N°d’ordre NNT : 2016LYSEI119

THESE de DOCTORAT DE L’UNIVERSITE DE LYON
opérée au sein de
l’INSA Lyon

Ecole Doctorale N° 162 :
MEGA

Spécialité de doctorat : Mécanique

Soutenue publiquement le 18/11/2016, par :
Nicolas Voeltzel

Molecular simulation of an ionic liquid as lubricant: from bulk rheology to nanoconfinement

---

Devant le jury composé de :

Espinosa-Marzal, RM	Associate Professor /University of Illinois	Rapportrice
Padua, A	Professeur / Université Blaise-Pascal	Raporteur
Neuville, A	Professor / University of Leeds	Examinatrice
Fillot, N	Maître de Conférences / INSA-Lyon	Directeur de thèse
Joly, L	Maître de Conférences / Université de Lyon	Co-Directeur de thèse
Vergne, P	Directeur de recherche / INSA-Lyon	Examinateur

Département FEDORA – INSA Lyon - Ecoles Doctorales – Quinquennal 2016-2020

SIGLE	ECOLE DOCTORALE	NOM ET COORDONNEES DU RESPONSABLE
CHIMIE	**CHIMIE DE LYON** **http://www.edchimie-lyon.fr** Sec : Renée EL MELHEM Bat Blaise Pascal 3e etage secretariat@edchimie-lyon.fr Insa : R. GOURDON	M. Stéphane DANIELE Institut de Recherches sur la Catalyse et l'Environnement de Lyon IRCELYON-UMR 5256 Équipe CDFA 2 avenue Albert Einstein 69626 Villeurbanne cedex directeur@edchimie-lyon.fr
E.E.A.	**ELECTRONIQUE, ELECTROTECHNIQUE, AUTOMATIQUE** **http://edeea.ec-lyon.fr** Sec : M.C. HAVGOUDOUKIAN Ecole-Doctorale.eea@ec-lyon.fr	M. Gérard SCORLETTI Ecole Centrale de Lyon 36 avenue Guy de Collongue 69134 ECULLY Tél : 04.72.18 60.97 Fax : 04 78 43 37 17 Gerard.scorletti@ec-lyon.fr
E2M2	**EVOLUTION, ECOSYSTEME, MICROBIOLOGIE, MODELISATION** **http://e2m2.universite-lyon.fr** Sec : Safia AIT CHALAL Bat Darwin - UCB Lyon 1 04.72.43.28.91 Insa : H. CHARLES Safia.ait-chalal@univ-lyon1.fr	Mme Gudrun BORNETTE CNRS UMR 5023 LEHNA Université Claude Bernard Lyon 1 Bât Forel 43 bd du 11 novembre 1918 69622 VILLEURBANNE Cédex Tél : 06.07.53.89.13 e2m2@ univ-lyon1.fr
EDISS	**INTERDISCIPLINAIRE SCIENCESSANTE** http://www.ediss-lyon.fr Sec : Safia AIT CHALAL Hôpital Louis Pradel – Bron 04 72 68 49 09 Insa : M. LAGARDE Safia.ait-chalal@univ-lyon1.fr	Mme Emmanuelle CANET-SOULAS INSERM U1060, CarMeN lab, Univ. Lyon 1 Bâtiment IMBL 11 avenue Jean Capelle INSA de Lyon 696621 Villeurbanne Tél : 04.72.68.49.09 Fax :04 72 68 49 16 Emmanuelle.canet@univ-lyon1.fr
INFOMATHS	**INFORMATIQUE ET MATHEMATIQUES** **http://infomaths.univ-lyon1.fr** Sec :Renée EL MELHEM Bat Blaise Pascal 3e etage infomaths@univ-lyon1.fr	Mme Sylvie CALABRETTO LIRIS – INSA de Lyon Bat Blaise Pascal 7 avenue Jean Capelle 69622 VILLEURBANNE Cedex Tél : 04.72. 43. 80. 46 Fax 04 72 43 16 87 Sylvie.calabretto@insa-lyon.fr
Matériaux	**MATERIAUX DE LYON** **http://ed34.universite-lyon.fr** Sec : M. LABOUNE PM : 71.70 –Fax : 87.12 Bat. Saint Exupéry Ed.materiaux@insa-lyon.fr	M. Jean-Yves BUFFIERE INSA de Lyon MATEIS Bâtiment Saint Exupéry 7 avenue Jean Capelle 69621 VILLEURBANNE Cedex Tél : 04.72.43 71.70 Fax 04 72 43 85 28 Ed.materiaux@insa-lyon.fr
MEGA	**MECANIQUE, ENERGETIQUE, GENIE CIVIL, ACOUSTIQUE** **http://mega.universite-lyon.fr** Sec : M. LABOUNE PM : 71.70 – Fax : 87.12 Bat. Saint Exupéry mega@insa-lyon.fr	M. Philippe BOISSE INSA de Lyon Laboratoire LAMCOS Bâtiment Jacquard 25 bis avenue Jean Capelle 69621 VILLEURBANNE Cedex Tél : 04.72 .43.71.70 Fax : 04 72 43 72 37 Philippe.boisse@insa-lyon.fr
ScSo	**ScSo*** **http://recherche.univ-lyon2.fr/scso/** Sec : Viviane POLSINELLI Brigitte DUBOIS Insa : J.Y. TOUSSAINT viviane.polsinelli@univ-lyon2.fr	Mme Isabelle VON BUELTZINGLOEWEN Université Lyon 2 86 rue Pasteur 69365 LYON Cedex 07 Tél : 04.78.77.23.86 Fax : 04.37.28.04.48

*ScSo : Histoire, Géographie, Aménagement, Urbanisme, Archéologie, Science politique, Sociologie, Anthropologie

Preface

The research work of this PhD thesis was conducted at the *Laboratoire de Mécanique des Contacts et des Structures* (LaMCoS) of the *Institut National des Sciences Appliquées* (INSA) of Lyon. It was funded by the industrial chair between INSA and SKF, a worldwide leading bearing and seal manufacturing company.

As a PhD is a long and animated experience, this work couldn't have success without substantial external support. For that, I wish to thank all the people who contributed to its accomplishment and in particular:

PhD supervisors: Nicolas FILLOT, Laurent JOLY and Philippe VERGNE

SKF supervisor: Guillermo E. MORALES ESPEJEL

Reviewers of the thesis: Rosa M. ESPINOSA MARZAL

President of the jury: Anne NEVILLE

Main other collaborators of the project

Nathalie BOUSCHARAIN
Andrew GIULIANI
Daniele SAVIO

My colleagues for their cheerful mood

Sayed ALBAHRANI
Romain BUGNICOURT
Jérôme CAVORET
Matthieu CHAPRON
Pauline CUSSEAU
Sophie DE OLIVEIRA
Martin DENNI
Jérôme DURAND
Grégoire ISAAC
Lionel LAFARGE
Charly LAGRESLE
Marion LE
Charlotte MARY
Bilel MEZIANE
Serigne NDIAGA NDIAYE

Dimitri NIEL
Alejandro PORRAS VAZQUEZ
Stéphane PORTRON
Pierre RABASO
Jérôme RIVIERE
Arnaud RUELLAN
Nina SAINTE-MARIE
Vincent STRUBEL
Thomas TOURET
Stéphane TROMP
Fabrice VILLE
Guillaume VOUAILLAT
Jean-David WHEELER

Finally, I would like to express all my love to my close friends and family for their indefectible affection and support during those past three years.

Table of contents

Résumé étendu

i.1 Introduction

Parmi les sciences contemporaines, la tribologie est celle qui étudie les phénomènes survenant entre 2 corps en contact, immobiles ou animés d'un mouvement relatif. Il en existe des applications dans de nombreux domaines industriels et dans des situations de la vie quotidienne. Le frottement, l'usure, les vibrations et la chaleur résultant du glissement de deux surfaces l'une par rapport à l'autre cherchent continuellement à être contrôlés ou réduits pour atteindre les performances maximales d'un système. Le développement de la tribologie intègre diverses autres disciplines telles que la science des matériaux, la physique, la mécanique ou la chimie. Par conséquent, les différentes approches pour progresser dans le domaine sont souvent pluridisciplinaires.

Dans les cas où le frottement cherche à être limité, des lubrifiants sont couramment employés afin de limiter les pertes d'énergie lors du cisaillement de deux surfaces solides. De nos jours, les systèmes mécaniques cherchent à répondre à des exigences économiques et environnementales de plus en plus importantes. Pour relever ce défi, différents fluides sont notamment étudiés et parmi eux, les liquides ioniques présentes des propriétés très intéressantes comme lubrifiant alternatif, en particulier pour fonctionner dans des environnements très hostiles (haute ou très basse pression, haute température,…).

Par ailleurs, la volonté de réduire la consommation d'énergie entraine une forte réduction des épaisseurs de film dans le contact, jusqu'à n'avoir plus que quelques couches de molécules (cf. Figure i-1). Ce sont alors des mécanismes survenant à l'échelle atomiques qui régulent la dynamique du contact (structuration du fluide, glissement à la paroi, résistance thermique d'interface,…). Il est donc nécessaire de les caractériser, puisqu'ils peuvent grandement impacter le comportement globale du système lubrifié.

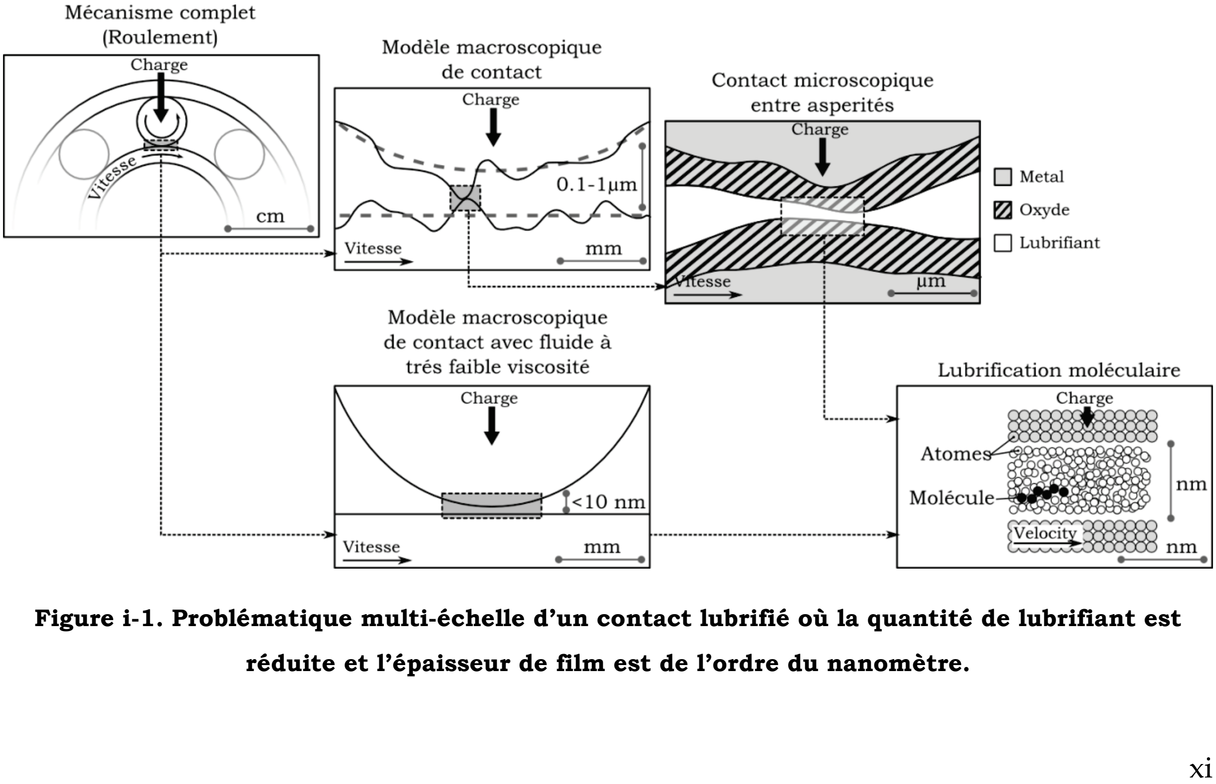

Figure i-1. Problématique multi-échelle d'un contact lubrifié où la quantité de lubrifiant est réduite et l'épaisseur de film est de l'ordre du nanomètre.

i.2 Etat de l'art et objectif

i.2.1 Film mince

Dans les régimes avec un film mince de lubrifiant, le frottement et l'usure des systèmes sont fortement impactés par les variations de l'épaisseur de film. Sa valeur ne peut pas être directement contrôlée dans un contact lubrifié en fonctionnement, mais elle dépend de deux propriétés du fluide : sa viscosité et son coefficient de piezoviscosité (CPV). Le CPV quantifiant l'influence de la pression sur la viscosité. Ainsi, l'estimation de ces quantités est la première étape pour prédire le potentiel de lubrification d'un fluide.

La viscosité et le PVC varient avec la température et la densité, qui sont loin d'être homogène dans un contact. Par conséquent, une caractérisation des deux valeurs en fonction de la température et de la densité est nécessaire de prévoir avec précision l'épaisseur de film d'un lubrifiant. Au cours des dix dernières années , cette caractérisation a été fait pour des fluides de natures différentes (hydrocarbures et les liquides ioniques entre autres) [1–4].

Les grands taux de cisaillement caractéristiques des films minces provoquent également des effets de rhéofluidification se traduisant par une chute de la viscosité souvent modélisée par la loi de Carreau :

$$\eta = \eta_0[1 + (t_{rel}.\dot{\gamma})^2]^{\frac{N-1}{2}} \tag{i.1}$$

avec la viscosité newtonienne η_0, le temps de relaxation t_{rel} un exposant N, trois valeurs intrinsèques au fluide, et $\dot{\gamma}$ le taux de cisaillement subit par le fluide. La viscosité newtonienne et le temps de relaxation dépendent des conditions de pression et de température, mais l'exposant N est traditionnellement considérée comme constant pour un fluide donné. Une analyse plus poussée doit être considéré pour évaluer cette approche.

Enfin, dans le cas des films très minces (0,1-10 nm), les dimensions associées du contact sont proches de la taille d'une molécule de lubrifiant, et une multitude de phénomènes locaux entrent alors également en jeu.

i.2.2 Lubrification moléculaire

Pour comprendre les mécanismes de lubrification moléculaire des films très minces, des approches à la fois expérimentales et numériques sont employées. Les différents travaux qui ont amené à l'état de connaissance actuelle des régimes de lubrification nano-confinés sont répertoriés dans cette partie.

Nano-rhéologie

Une première spécificité de la lubrification moléculaire est la modification du comportement rhéologique du film très mince. En particulier, le fluide ne peut pas être considéré comme un milieu homogène puisque sa viscosité change localement avec la variation de certaines conditions de fonctionnement. La viscosité apparente du contact dépend notamment de l'épaisseur de film de lubrifiant.

Ainsi, en dessous de 50 nm, la viscosité du fluide augmente progressivement [5]. Ensuite, lorsque moins de dix couches moléculaires restent entre les deux surfaces du confinement, la viscosité augmente drastiquement avec la réduction de l'épaisseur [6–10]. Enfin, lorsque le film de lubrifiant est constitué uniquement d'une à deux couches de molécules il se comporte comme un solide et sa viscosité peut être de plusieurs ordres de grandeur plus élevée que celle du fluide non confiné [10,11].

Structuration du fluide

Lorsqu'un liquide est en contact avec un corps non déformable, un agencement ordonné des molécules de fluide à lieu à l'interface liquide/solide. Ainsi, les molécules de lubrifiant ont tendance à se structurer en couches denses qui modifient localement la mobilité du fluide (voir la Figure i-2). La structuration peut être apparente à une distance de la paroi allant jusqu'à dix fois le diamètre des molécules [12]. Par ailleurs, de nombreux facteurs influent sur les conditions de formation de la structuration : les propriétés chimiques et l'état de surface de la paroi, la taille et la forme des molécules du lubrifiant ou sa teneur en eau [13].

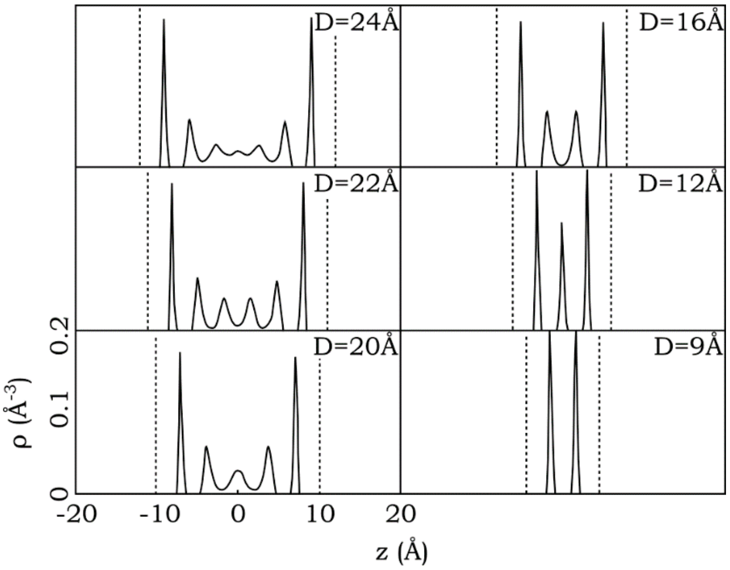

Figure i-2. Profile de densité dans l'épaisseur de lubrifiant (direction *z*) pour un fluide Lennard-Jones confiné. La distance *h* entre les parois (lignes en pointillé) varie de 24 à 9 Å, soit 7 à 2 couches moléculaires. Résultats de Gao et al. [14].

Ecoulement à l'interface liquide / solide

En plus de la structuration du lubrifiant, le cisaillement d'un système nanoconfiné inclut des phénomènes d'interface dans la dynamique de l'écoulement. Deux mode d'écoulement sont ainsi identifiés à l'interface liquide/solide: le glissement et le blocage [15].

Lorsque les forces issues de la liaison liquide/solide sont plus faibles que les forces de cohésion du liquide, le lubrifiant glisse sur la surface (voir Figure i-3). L'origine du glissement à la paroi dépend donc à la fois des interactions d'interface et de la viscosité du fluide. La corrugation définit l'énergie nécessaire pour initier le mouvement tangentiel d'une molécule fluide par rapport à l'interface. Une faible corrugation encourage ainsi le glissement à l'interface. Une interprétation des forces de corrugation peut être faite au travers du frottement fluide λ défini comme le rapport entre la contrainte de cisaillement τ et le glissement de vitesse à l'interface liquide/solide v_{slip}. En outre, comme une partie du cisaillement est captée par l'interface, une différenciation doit être faite entre le taux de cisaillement apparent du contact et le taux de cisaillement effectif dans le fluide. La longueur de glissement L_s, définie comme le rapport entre le saut de vitesse à l'interface et le taux de cisaillement effectif, est ensuite introduite pour quantifier le glissement à la paroi à l'interface liquide/solide. Trois régimes critiques sont ensuite identifiés : glissement parfait lorsque $L_s \rightarrow \infty$, glissement partiel, et pas de glissement lorsque $L_s \rightarrow 0$. Finalement, lorsqu'un glissement important est atteint, il a été observé expérimentalement que cela peut avoir un impact significatif sur le frottement à l'échelle macroscopique [16].

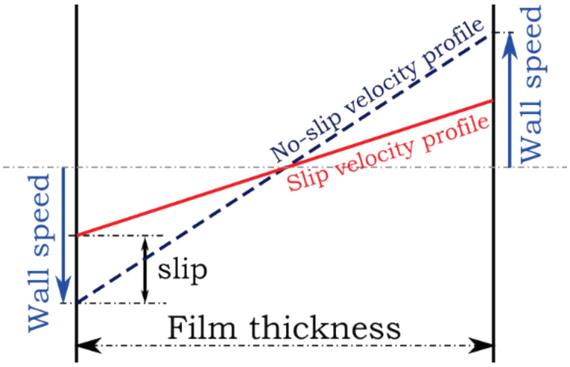

Figure i-3. Représentation schématique du glissement à la paroi d'un fluide nano-confiné cisaillé.

Enfin, un " blocage " des molécules fluides à l'interface se produit lorsque les conditions ne sont pas réunies pour qu'il y ait du glissement à la paroi, mais que les forces de cohésion dans les premières couches de fluide proche de l'interface sont encore plus fortes que celles dans le fluide en volume. Dans ce cas, une épaisseur de 1 à 2 molécules de fluide est verrouillée à la surface (pas de mouvement relatif tangentiel) et le cisaillement s'opère dans le lubrifiant, plus loin des surfaces.

Résistance thermique d'interface

Un dernier aspect important lié au régime de lubrification moléculaire est la régulation thermique. La température des matériaux présents impacte directement les performances du système lubrifié en modifiant la dynamique des fluides (viscosité, glissement à la paroi) et en encourageant les réactions d'oxydation du lubrifiant de corrosion à l'interface liquide/solide. Les conditions extrêmes du régime en film très mince génèrent une chaleur importante qui peut être évacuée à différentes vitesses. En effet, dans le cas des films très minces, l'élévation de la température est principalement pilotée par la résistance thermique de l'interface liquide/solide R_{th}, elle-même dépendante des interactions entre le fluide et les surfaces [17].

Après cet état de l'art des mécanismes de lubrification en film très mince, certaines questions demeurent. Entre autres, pour mieux caractériser le fonctionnement des lubrifiants classiques, des études plus poussées sont nécessaires avec des fluides plus réalistes. Certaines surfaces ont aussi révélé leur nature très glissante mais doivent encore être testées dans des conditions de lubrification réalistes. De plus, la température ayant un impact direct sur la nano-rhéologie et les réactions chimiques possibles, son comportement doit être mieux caractérisé par rapport à la résistance thermique d'interface.

i.2.3 Potentiel des fluides ioniques comme lubrifiants

Les liquides ioniques (LIs) constituent une famille de fluides qui présentent de nombreux atouts comme lubrifiants alternatifs aux huiles couramment utilisées. Par la suite, les LIs sont présentés, puis le savoir et les lacunes dans la connaissance des mécanismes de lubrification qui leurs sont propres sont détaillés. Les limites connues des LIs comme lubrifiants sont également exposées.

Premier aperçu des liquides ioniques comme lubrifiants

Les LIs, sont des sels liquides à température et pression ambiantes, généralement constitués d'un anion et d'un cation [18]. Leur point de fusion bas, leur volatilité négligeable et leur propriété ignifuge sont autant d'attributs essentiels pour des lubrifiants opérants dans des conditions de fonctionnement extrêmes. Par ailleurs, la forte polarité des LIs induit la formation d'un film absorbé sur les surfaces à lubrifier chargées et les protège ainsi d'un contact direct solide/solide destructeur. Enfin, compte tenu de la grande diversité des types de cations et d'anions, il existe un très grand nombre de combinaisons possibles de LIs, certaines estimations atteignant jusqu'à 10^{18} possibilités [19]. Dans la pratique, le choix du couple {cation, anion} pourra se révéler performant dans certaines applications spécifiques mais inapproprié dans d'autres.

Les LIs ont principalement été comparés à des huiles classiques de lubrification [20]. Ainsi, à différentes conditions de température et de pression, les LIs induisent moins de frottement et d'usure que les huiles de référence. Les LIs ont également été testés comme des lubrifiants mais avec des approches différentes : soit avec des additifs, soit en tant qu'additif, soit dans des environnements très spécifiques tels que dans le vide (pour des applications au spatiale) ou en film mince continu (pour des applications à l'électronique). Dans tous les cas, l'utilisation des LIs a tendance à améliorer les performances des systèmes (moins de frottement et d'usure) et certaines études pointent l'importance de maîtriser la natures des ions d'un LI (taille, forme, composition) pour optimiser les performances.

Mécanismes de lubrification propres aux liquides ioniques

Tout d'abord, concernant les propriétés rhéologiques des LIs, leur viscosité et leur coefficient de piezoviscosité sont en général suffisamment élevés pour maintenir le film hydrodynamique qui permet d'assurer la lubrification d'un système. Mais ces propriétés sont extrêmement dépendantes de la nature des ions. A titre d'exemple, la viscosité étant liée à la longueur des chaînes alkyles, le volume d'usure produit par un contact lubrifié avec un LI [C_{12}MIm][PF_6] est dix fois plus faible que pour le même contact lubrifié avec un LI [C_1MIm][PF_6] (même LI avec une chaine alkyl douze fois plus petite au cation) [20].

Par ailleurs, la structuration des LIs à l'interface liquide/solide est similaire à celle observée dans le cas des fluides apolaires présentés précédemment, à ceci près qu'elle dépend de la nature polaire des surfaces. En effet, une surface chargée entraîne une structuration particulière du LI en monocouches successives de cations et d'anions [21] et la structuration est d'autant plus marquée que l'intensité de la charge augmente [22]. En plus de la structuration du fluide, les fortes interactions liquide/solide issues des charges électrostatiques augmentent l'adhérence d'un film de fluide protégeant ainsi contre un éventuel contact sec entre les deux surfaces.

Enfin les charges ont également un effet sur la dynamique du fluide près de l'interface. D'une part il a été observé qu'avec des surfaces chargées, la viscosité du fluide augmentait au point de faire croitre le frottement dans les régimes avec une très faible épaisseur de film (< 20 nm) [23]. D'autre part, le LI se déplace à l'interface en enchainant successivement adhésions et glissements à la paroi.

Limitation de l'utilisation des LIs comme lubrifiants

Malgré les performances remarquables des LIs comme lubrifiants, leur usage présente également quelques restrictions.

D'une part, en raison de leur polarité élevée, la capacité d'absorption de l'eau des LIs est plus élevé que pour les lubrifiants classiques et la tribo-corrosion à l'interface liquide/solide avec des surfaces métalliques est plus importante [20]. Dans les contacts, cette réaction peut créer un film anti-usure bénéfique, mais si les composants sont hautement réactifs, les surfaces se dégradent significativement et provoque la défaillance globale du système. Néanmoins, cette dégradation chimique peut être limitée. En particulier, le choix d'un LI approprié peut considérablement réduire la corrosion.

D'autre part, bien que les LIs soient considérés comme des lubrifiants « écologiques » en raison de leur origine non fossile, leur réactivité élevée peut également être toxiques pour certains milieux naturels. En particulier, les LIs avec de longues chaînes alkyles lipophiles ont tendance à augmenter leur nocivité [24]. Certains ions ont en revanche été remarqués comme étant respectueux de l'environnement. Des études de toxicité plus approfondies des différents LIs sont nécessaires pour sélectionner les meilleurs candidats comme lubrifiant écologique.

Après l'examen des propriétés macroscopiques des LIs et leur comportement en nanoconfinement, certaines questions demeurent. Notamment, une étude détaillée de leur réponse à des cisaillements importants est manquante. Dans l'étude qui suit, le comportement d'un LI est étudié dans diverses configurations représentatives des régimes en films minces ou très minces. Entre autres, l'étude de la dynamique du contact doit alimenter les discussions sur la réponse du frottement au cisaillement avec des surfaces polaires ou d'autres très glissantes.

i.3 L’outil de dynamique moléculaire

Pour répondre aux problématiques posées, le choix a été fait d'utiliser un outil numérique capable de simuler la dynamique des particules à l'échelle nanométrique : la dynamique moléculaire (DM). Par rapport aux études expérimentales, une telle approche permet de tester facilement un grand nombre de cas et de configurer avec précision les entrées thermodynamiques de pression, de température et de cisaillement. Une fois rigoureusement validée, la méthode est également capable d'estimer quantitativement des quantités physiques d'intérêt résultant du système simulé. En outre, comme l'objectif principal est de comprendre les mécanismes impliqués dans le processus de lubrification, l’outil numérique offre la possibilité d'avoir un regard direct sur les phénomènes locaux et de les caractériser pour une large gamme de conditions thermodynamiques.

i.3.1 Théorie de la dynamique moléculaire

La principale difficulté pour modéliser correctement le comportement du matériau dans les simulations de DM est la définition des interactions interatomiques (comme les liaisons chimiques, les interactions faibles, les liaisons hydrogène ou les interactions de Coulomb). Un champ de force fait référence aux modèles et aux ensembles de paramètres utilisés pour calculer l'énergie potentielle résultant de ces interactions.

Les champs de force peuvent être de plusieurs natures selon la précision souhaitée des simulations par rapport aux temps de calculs envisageables. Les champs de forces les plus précis seront coûteux en temps de calcul mais fourniront des résultats plus réalistes que ceux obtenus avec des champs de forces plus grossiers.

Définir les jeux de paramètres des champs de forces est l'aspect le plus sensible de la DM. Ils influencent directement les propriétés de la matière modélisée et ses interactions avec d'autres matériaux. Ils sont déterminés à partir des données expérimentales pour vérifier certaines propriétés physiques (champs de force empiriques) ou à partir de calculs ab-initio. Quelle que soit la méthode, ils sont toujours déterminés sur une gamme limitée de conditions environnementales (pression, température, état physique...) et leur validité doit donc être vérifiée avant l'utilisation dans des situations différentes des conditions d'établissement du champs de force.

Pour modéliser la physique du système simulé, la MD résout explicitement l'équation newtonienne du mouvement au fil du temps. Les positions et les vitesses de chaque atome sont alors calculées itérativement à chaque pas de temps donné, en fonction des forces d'interaction entre les atomes et des contraintes thermodynamiques simulant les conditions de fonctionnement.

Parmi les liquides ioniques étudiés dans la littérature, ceux avec des anions du type bis(trifluoromethylsulfonyl)amide [NTf2-] et des cations de la famille des imidazolium sont très performants comme lubrifiants. Ainsi, dans cette étude, le choix a été fait de travailler avec du 1-3 dimethylimidazolium bis(trifluoromethylsulfonyl)amide [$mmIm^+$][NTf_2^-] (voir

Figure i-4) qui de plus présente une viscosité proche des huiles classiques à température et pression ambiante (≈ 30 mPa.s).

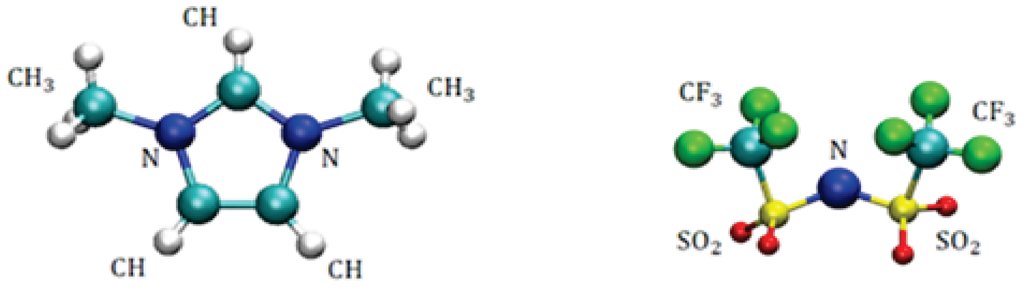

1,3-dimethylimidazolium [$mmIm^+$]

bis(trifluoromethylsulfonyl)imide [NTf_2^-]

Figure i-4. Le liquide ionique modélisé: Molécules du cation (à gauche) et de l'anion (à droite).

Un champ de force initialement développé par Canongia Lopes et Pádua [25,26] pour une large gamme de liquide ionique a été ajusté pour modéliser le [$mmIm^+$][NTf_2^-]. Pour valider les adaptations réalisés sur le champ de force, les variations de certaines propriétés de transport (viscosité et coefficient de diffusion) et de la densité en fonction de la température, ont été confrontées à des mesures expérimentales.

i.3.2 Simulation du fluide ionique en volume

Pour caractériser la réponse du fluide aux différentes sollicitations d'un contact lubrifié (hautes températures, hautes pressions et taux de cisaillement importants), la nature du [$NTf2^-$][$mmIm^+$] est tout d'abord étudiée au travers de simulations d'un volume de LI homogène. Dans cette configuration, les conditions périodiques sont définies dans les trois directions du domaine de simulation pour simuler un milieu fluide infini. En supposant que le fluide en volume est un système ergodique, ses propriétés thermodynamiques macroscopiques peuvent alors être déterminées grâce aux simulations de DM.

Des simulations à l'équilibre sont réalisées pour déterminer les variations de densité, de diffusion et de viscosité newtonienne en fonction de la pression et de la température. En revanche, pour étudier l'influence du cisaillement du fluide sur la viscosité (rhéofluidification), les simulations sortent de l'équilibre et sont stabilisées à un régime stationnaire avant que les grandeurs mesurées ne soient relevées.

i.3.3 Simulation d'un nano-contact lubrifié

Le liquide ionique est également nano-confiné entre deux surfaces ayant un mouvement relatifs. Différents matériaux ont été étudiés dans ce travail pour comprendre l'influence de leurs propriétés sur la phénoménologie de l'interface. Pour décrire le cas d'un contact acier-acier lubrifié réaliste, de l'oxyde de fer (FeO) a d'abord été intégré dans les simulations de confinement. Par ailleurs, les revêtements Diamond-Like-Carbon (DLC) sont utilisés pour améliorer sensiblement les performances tribologiques des systèmes frottant. Plusieurs matériaux à base de carbone ont ainsi été intégrés aux simulations pour étudier les spécificités du DLC dans un contact lubrifié.

Dans ces simulations, le nombre de molécules de LI est constant et des conditions aux limites périodiques sont définies le long des deux directions perpendiculaires au confinement, simulant ainsi des surfaces infinies (voir Figure i-5). Une pression normale aux surfaces permet d'assurer le confinement. La température est régulée dans l'interface mais laissée libre dans le fluide pour que l'influence de la température puisse être caractérisée. Enfin un mouvement relatif, parallèle au confinement, est imposé aux deux surfaces pour créer un cisaillement.

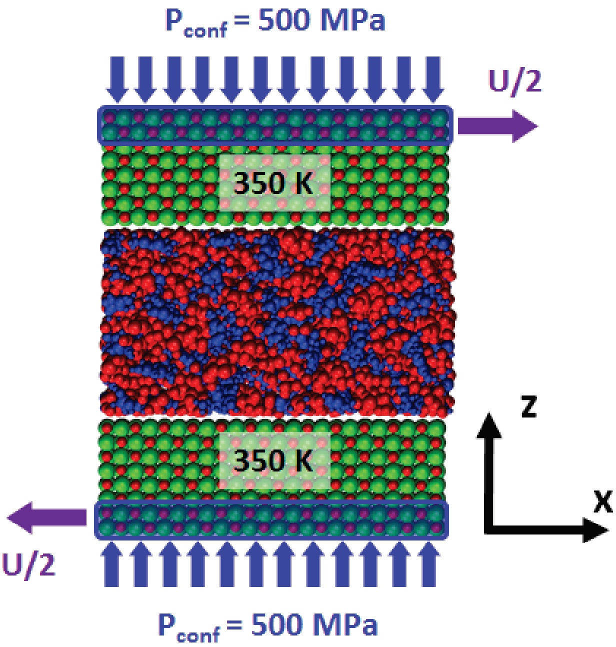

Figure i-5. Principe de confinement et de cisaillement du fluide. En bleu, les régions où la pression et le mouvement sont imposés.

Un certain nombre de valeurs peuvent être calculées grâce à ces simulations pour comprendre le comportement dynamique d'un nano-contact. Les profils de température et de vitesse donnent notamment des indications sur les effets du cisaillement sur le fluide en fonction de la vitesse de cisaillement et de la nature des surfaces.

i.4 Rhéologie en films minces

Ce chapitre offre une image complète de la rhéologie du [mmIm$^+$][NTf$_2^-$], basée sur environ 200 simulations de DM et avec une contribution expérimentale, dans des conditions de pression, température et cisaillement représentatives des régimes élasto-hydrodynamique (EHD) ou film mince. Pour répondre au besoin de savoir estimer l'épaisseur de film, la viscosité et le CPV (coefficient de piezoviscosité) du LI sont tout d'abord évalués en régime linéaire. Puis l'étude va plus loin en caractérisant les variations de la viscosité avec des taux de cisaillement très importants, propres aux régimes en film mince.

i.4.1 Régime linéaire

Lors de l'analyse de la réponse rhéologique du LI en régime linéaire, les résultats de DM sont confrontés à des mesures expérimentales pour renforcer la fiabilité de l'étude. Les résultats sont présentés en Figure i-6.

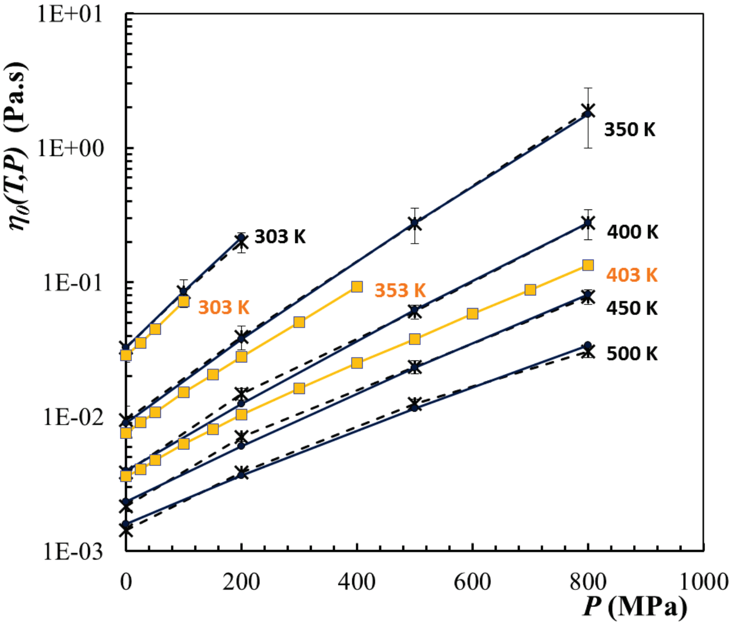

Figure i-6. Viscosité du [mmIm$^+$][NTf2$^-$] en fonction de la pression pour différentes températures. Les résultats expérimentaux sont représentés par des carrés jaunes et le modèle WLF correspondant par des lignes jaunes. Les résultats de DM sont représentés par des étoiles noires et des traits en pointillé noirs et le modèle WLF correspondant par des lignes noires.

La comparaison entre les expériences et les simulations montre un accord quantitatif acceptable à 303 et 350 K. Cependant, une nette surestimation de l'influence de la pression sur la viscosité par des calculs de DM est observée à des températures élevées. À 400 K l'écart n'est clairement plus négligeable pour les hautes pressions. En complément, le modèle WLF-Yasutomi, permettant de prédire la viscosité newtonienne en fonction de la pression et de la température, est appliqué sur les deux sets de valeurs (expérimental et numérique). Dans les deux cas le modèle est capable de prédire avec précision la variation de la viscosité newtonienne puisque l'écart relatif est de 2,1 % pour prédire les données expérimentales et de 8,8 % pour prédire les données numériques.

Les résultats précédents ont également permis de calculer la variation du CPV en fonction de la température. Il en résulte un CPV deux fois plus faible que celui d'une huile lubrifiante classique mais qui suit une évolution similaire avec la variation de température.

i.4.2 Régime non-linéaire

Pour anticiper les effets de rhéofluidification, les variations de viscosité du LI ont également été caractérisées dans le domaine non-linéaire (i.e. lorsque le cisaillement est suffisamment important pour faire perdre au fluide sa propriété newtonienne). La Figure i-7 illustre le phénomène pour différents cas de pression et température.

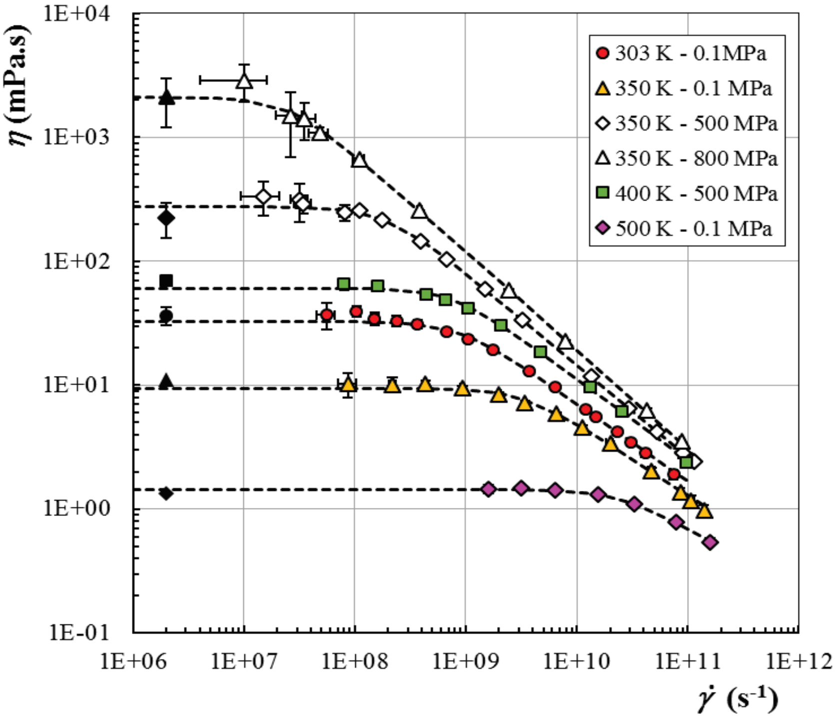

Figure i-7. Variation de la viscosité du [mmIm$^+$][NTf$_2^-$] obtenue à partir de calcul de DM en fonction du taux de cisaillement à différentes conditions (T, P), sélectionnées arbitrairement. Les lignes en pointillé représentent la régression de chaque configuration au modèle de Carreau.

Grâce à la normalisation des différents cas (T, P) à une même courbe maitresse, l'étude de la pertinence du modèle de Carreau (Equation i.1) est rendu possible.

D'une part, la variation du temps de relaxation, inverse du taux de cisaillement critique $\dot{\gamma}_c$ entre le régime linéaire et le régime non-newtonien, a pu être exprimée en fonction de la température et de propriétés intrinsèques au fluide :

$$t_{rel} = \frac{1}{\dot{\gamma}_c} = K \cdot \frac{\eta_0(T,P)}{\rho(T,P) \cdot T} \tag{i.2}$$

avec ρ la densité du fluide et K une constante. Cela indique notamment que les temps de relaxation dérivés du modèle de Carreau ne sont pas des paramètres purement numériques sans signification, mais des résultats pertinents du point de vue rhéologique et physique.

D'autre part, les variations de l'exposant N, jusqu'ici considéré dans la littérature comme indépendant des conditions de température et de pression, ont également pu être caractérisées à la fois au travers d'un modèle analytique purement numérique et par une relation avec le temps de relaxation :

$$N = a.\,ln(t_{rel}) + b \tag{i.3}$$

avec a et b respectivement égaux à -0.0474 et 0.362. Ainsi, la variation de l'exposant révèle une plus grande sensibilité de la viscosité et donc de l'épaisseur de film du contact lubrifié, à haute pression et à basse température.

i.5 Confinement et cisaillement

Dans cette partie, le liquide ionique [mmIm$^+$][NTf$_2^-$] est confiné entre deux surfaces caractéristiques d'un contact acier-acier : des surfaces d'oxyde de fer (voir Figure i-5). La réponse du système au confinement et au cisaillement est étudiée qualitativement et quantitativement pour mieux comprendre les mécanismes de lubrification moléculaire caractéristique des films très minces.

i.5.1 Structuration et orientation du liquide ionique confiné

188 pairs de [mmIm$^+$][NTf$_2^-$] sont confinées entre 2 surfaces d'oxyde de fer (FeO). Il en résulte une épaisseur de film de 2,8 nm. Comme attendu, le liquide ionique réagit avec les surfaces en se structurant en couches parallèles à celles-ci (voir courbe noir sur la Figure i-8).

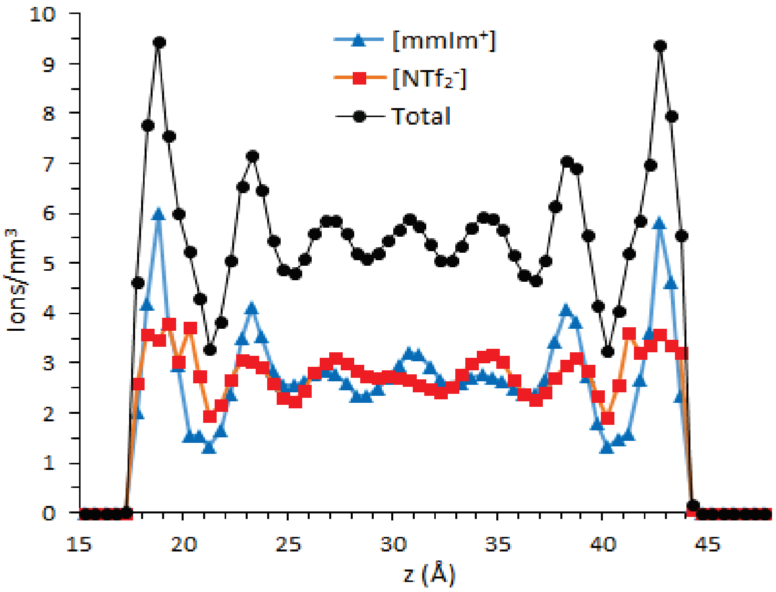

Figure i-8. Profile de densité volumique du [mmIm$^+$][NTf$_2^-$] confiné entre deux surfaces d'oxide de fer (FeO) à une pression *P* = 500 MPa et une température *T* = 350 K.

La densité des ions dans les premières couches correspond à 220 % et à 135 % celle du fluide non-confiné pour le cation et l'anion respectivement. Par ailleurs, en accord avec de précédentes études numériques et expérimentales, les cations et les anions sont présents dans toutes les couches lorsque le LI est confiné entre des matériaux non-chargés (polarisés ou non) [22,27,28]. Ce constat contraste avec la structuration des LI entre des surfaces chargées où les couches formées à l'interface sont des monocouches successives d'anions ou de cations.

En plus de la structuration, l'orientation des ions à l'interface liquide/solide a été étudiée. Alors que les cations se positionnent dans les couches en plans parallèles aux surfaces, les anions, eux, sont orientés avec leur fonction CF_3 pointant en direction du centre du confinement et avec leurs atomes d'oxygènes positionnés au plus proche des surfaces. Il en résulte que les oxygènes des anions et les hydrogènes des cations peuvent réagir chimiquement avec le substrat. Les matériaux de confinement doivent alors être choisis en conséquence pour éviter des phénomènes indésirables de corrosion ou pour favoriser la formation d'un film protecteur.

Enfin, pour analyser l'effet réel de la structuration du fluide sur la rhéologie du fluide et sur le glissement à la paroi, un mouvement de cisaillement est ajouté au système.

i.5.2 Réponse du nano-contact cisaillé

Le liquide ionique est cisaillé sur une large plage de vitesse (de 2 à 160 m/s). Il en résulte un coefficient de frottement relativement élevé (0.1 - 0.2), mais qui sature aux grandes vitesses de cisaillement (voir Figure i-9).

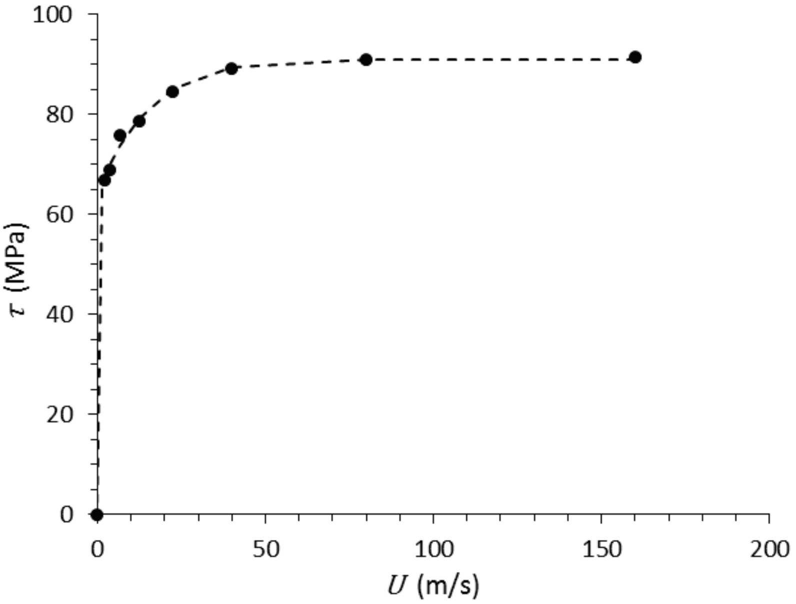

Figure i-9. Evolution de la contrainte de cisaillement τ dans le nano-contact lubrifié en fonction de la vitesse de cisaillement, pour une pression de confinement de 500 MPa et une température des parois fixée à 350 K.

Comme le contrôle du frottement est une préoccupation majeure de la communauté tribologique, l'analyse qui suit vise à décorréler les mécanismes à l'œuvre afin d'estimer leurs influences individuelles sur le frottement.

Le cisaillement imposé au système est absorbé à la fois par la déformation du LI et par le glissement des ions à l'interface liquide/solide. Ces deux mécanismes dépendent l'un de l'autre puisqu'ils sont tous les deux à l'origine de la contrainte de cisaillement :

$$\tau = \eta . \dot{\gamma}_{eff} = \lambda . v_{slip} \qquad (i.4)$$

avec $\dot{\gamma}_{eff}$ le taux de cisaillement effectif du fluide, η sa viscosité, λ le frottement fluide à l'interface et v_{slip} le saut de vitesse à l'interface. Ainsi, l'étude de la viscosité η et du coefficient de frottement fluide λ en fonction du cisaillement suffisent à expliquer la dynamique en place dans le nano-contact. La Figure i-10 illustre la variation des deux grandeurs en fonction du cisaillement effectif du fluide.

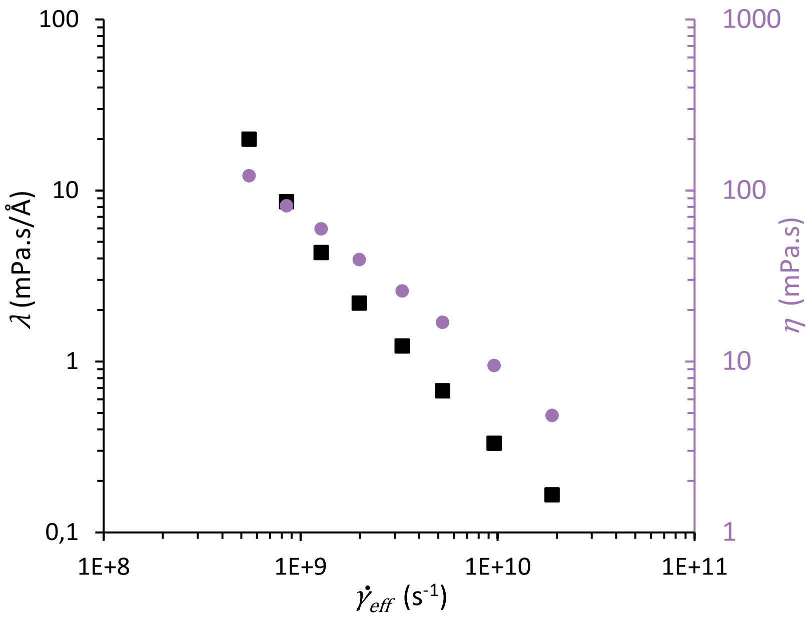

Figure i-10. Variation du coefficient de frottement fluide λ à l'interface IL/FeO et de la viscosité du LI η en fonction du taux de cisaillement effectif.

Le glissement dépend directement de ces deux paramètres puisqu'il est d'autant plus important que la surface est glissante (λ faible) et que la viscosité du fluide est importante (η important). La longueur de glissement L_s lie ces deux paramètres par la relation :

$$L_s = \frac{\eta}{\lambda} \qquad (i.5)$$

La variation de L_s avec le cisaillement effectif est tracée en Figure i-11.

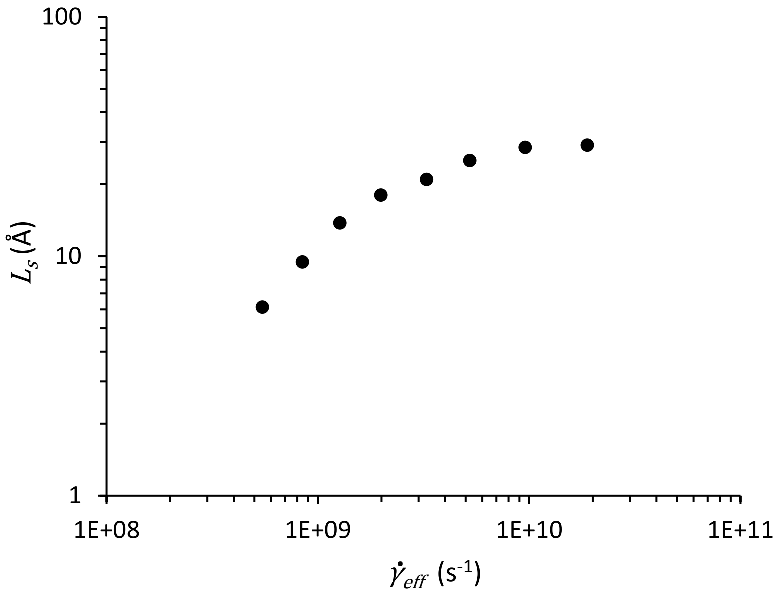

Figure i-11. Longueur L_s de glissement en fonction du cisaillement effectif du fluide

La mouillabilité du couple LI/FeO est également estimée à partir de la mesure de l'angle de contact d'une goutte de LI déposée sur du FeO. L'angle mesuré est de 43° ce qui traduit une forte adsorption du fluide sur le substrat.

Plusieurs observations découlent de ces résultats. Premièrement, malgré une mouillabilité importante, le glissement a un rôle non négligeable dans la dynamique du contact puisque la longueur de glissement atteint plus d'un nanomètre pour un contact de trois nanomètre d'épaisseur soit environ un tiers du cisaillement qui est absorbé par le glissement à l'interface. Deux origines à ce constat : la forte viscosité due au confinement sévère (225 mPa.s à 500 MPa), ainsi que la réduction de la viscosité qui est plus lente que celle du coefficient de frottement fluide (Figure i-10), ce qui a pour effet d'augmenter le glissement (cf. Equation i.5). Deuxièmement, à des taux de cisaillement importants, le frottement fluide décroit moins rapidement et rejoint la tendance de variation de la viscosité (Figure i-10). Cela a pour conséquence une saturation de la longueur de glissement aux hauts taux de cisaillement (Figure i-11). Enfin, la variation de la viscosité peut être prédite par la loi de Carreau comme dans des configurations de fluide non confiné (cf. partie i.4). Cependant, l'exposant N décrivant la vitesse de réductions de la viscosité est différent pour des conditions de pression similaire. Seule la variation de température du LI dans les systèmes confinés cisaillés peut expliquer le changement de l'exposant N.

i.5.3 Le rôle complexe de la température

Dans les systèmes nano-confinés, le cisaillement important du fluide visqueux est à l'origine d'une forte génération de chaleur Q :

$$Q = \eta . \dot{\gamma}_{eff}^{\ 2} \tag{i.6}$$

Etant donné que la chaleur générée dans le fluide se dissipe dans les solides, la résistance thermique de l'interface liquide/solide R_{th} joue un rôle crucial dans le comportement thermique du système. La Figure i-12 en témoigne fortement puisqu'un saut important de température est observable aux interfaces liquide/solide.

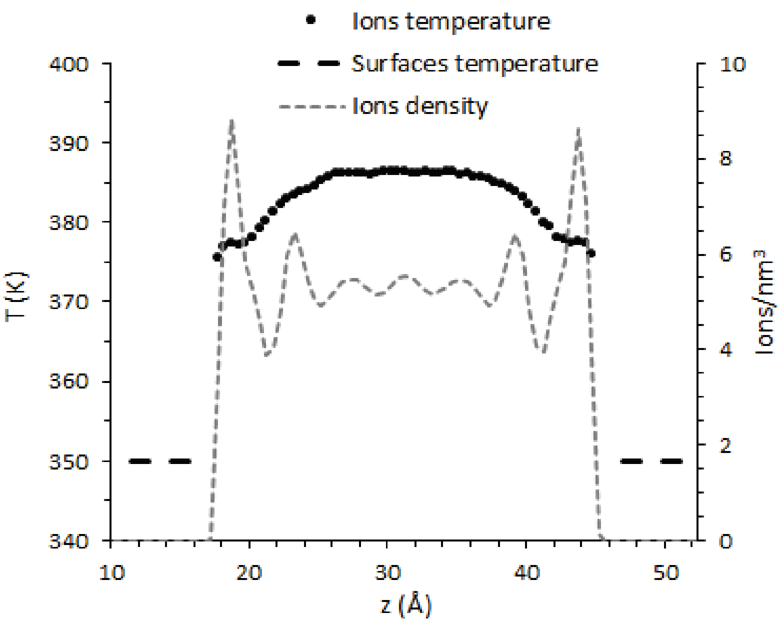

Figure i-12. Profile de température typique dans un contact nano-confiné. Ici, pour une vitesse de cisaillement U = 40 m/s.

Les fortes températures vont, d'une part, modifier la dynamique du contact en provoquant une chute de la viscosité, d'autre part, amplifier les potentielles réactions chimiques d'oxydation du lubrifiant ou de corrosion du substrat. Il est donc essentiel de maîtriser son évolution pour assurer le bon fonctionnement du contact lubrifié. Dans cette optique, une expression de la température dans le contact confinée a été développée :

$$T(z) = \frac{\eta \dot{\gamma}_{eff}{}^{2}}{4k}\left(h\left(R_{th}k + \frac{h}{4}\right) - z^2\right) + T_{wall} \qquad (\text{i}.14)$$

avec k la conductance thermique du fluide et T_{wall} la température de la surface à l'interface.

(

Au-delà de l'influence de la température, le rôle de la nature des surfaces dans la dynamique du contact est toujours source d'interrogation. La section suivante apporte des éléments de réponse essentiels en comparant le comportement dynamique du contact cisaillé par les surfaces de FeO à des contacts cisaillés par des surfaces de différentes natures.

i.6 Influence de la nature des surfaces

Il a été montré dans la section précédente qu'à l'échelle moléculaire, le frottement à l'interface entre le lubrifiant fluide et la surface solide est un élément clé de la dynamique des contacts. Par ailleurs, Savio et al. [29] a montré que si le glissement n'était pas le même sur les deux surfaces d'un contact lubrifié en régime élasto-hydrodynamique (EHD), l'épaisseur du film est grandement affectée et peut soit augmenter, soit diminuer. Dans le dernier cas, des ruptures locales du film de lubrifiant peuvent apparaitre, entrainant alors des dommages physiques au système.

Parmi les matériaux prometteurs pour des applications tribologiques, les revêtements DLC (Diamond-Like Carbon) présentent un frottement très faible et une résistance élevée à l'usure [30,31]. Différents matériaux à base de carbone proches des DLC sont ainsi étudiés dans l'optique de comprendre l'impact de leur nature sur la dynamique du contact.

i.6.1 Dynamique et frottement issus de différentes surfaces

Les quatre matériaux à base de carbone étudiés sont le diamant, le graphite et deux carbones amorphes (a-C) avec des rugosités nanométriques légèrement différentes. Le cisaillement du [mmIm$^+$][NTf$_2^-$] par les différentes surfaces entraine des comportements dynamiques du contact très différents comme en atteste la forte disparité de la longueur de glissement en Figure i-13.

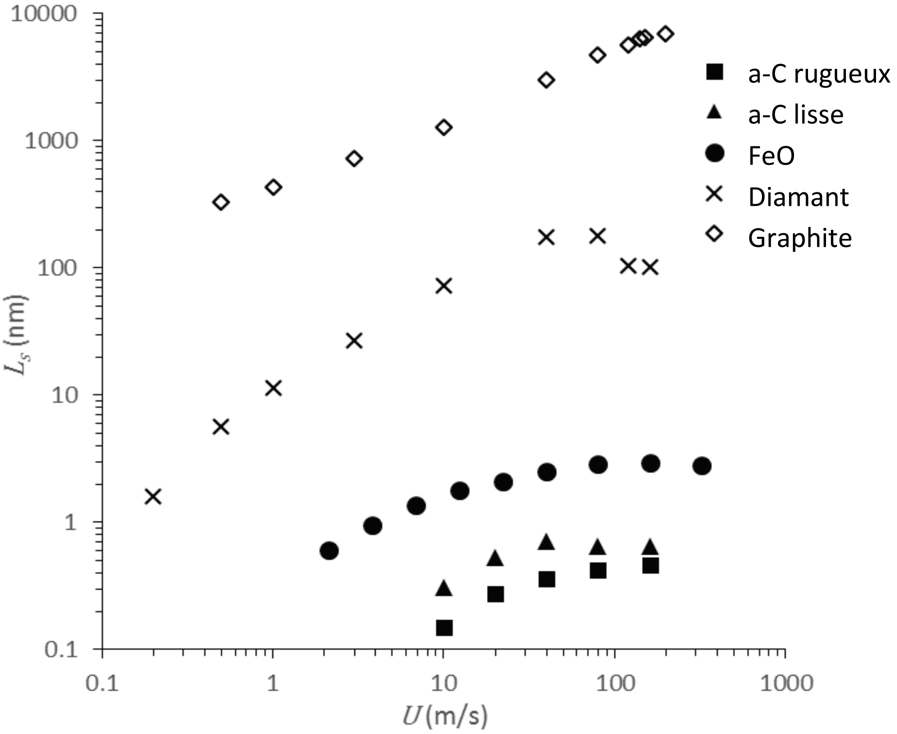

Figure i-13. Variation de la longueur de glissement avec la vitesse de cisaillement à partir du cisaillement par cinq surfaces différentes.

La longueur de glissement varie de plus de cinq ordres de grandeur entre les différentes surfaces. Alors que les surfaces de carbone amorphe entrainent des longueurs de glissement inférieures à celle associée à l'oxyde de fer, le diamant et surtout le graphite sont à l'origine de glissements considérables, ce qui modifie profondément la dynamique du système. Ainsi même pour des épaisseurs de film standards dans les systèmes lubrifiés (i.e. de l'ordre du dixième de micromètre), le glissement peut être prédominent et gouverner le comportement dynamique du contact.

Par ailleurs, la longueur de glissement issue des surfaces d'oxyde de fer et de carbone amorphe saturent à une vitesse de cisaillement donnée. Ce comportement a été observé et expliqué dans la section précédente pour l'oxyde de fer et le même mécanisme survient ici avec les surfaces non-glissantes de carbone amorphe.

Comme l'épaisseur de film est d'environ 3 nm dans les présentes simulations, lorsque la longueur de glissement est bien supérieure à l'épaisseur de film (cas du graphite et du diamant), le cisaillement est quasiment intégralement absorbé par le glissement aux interfaces liquide/solide. A l'inverse, dans les configurations où la longueur de glissement est inférieure à l'épaisseur de film, le cisaillement est absorbé par la déformation du fluide. Cette dynamique est également liée au frottement comme en témoigne la Figure i-14.

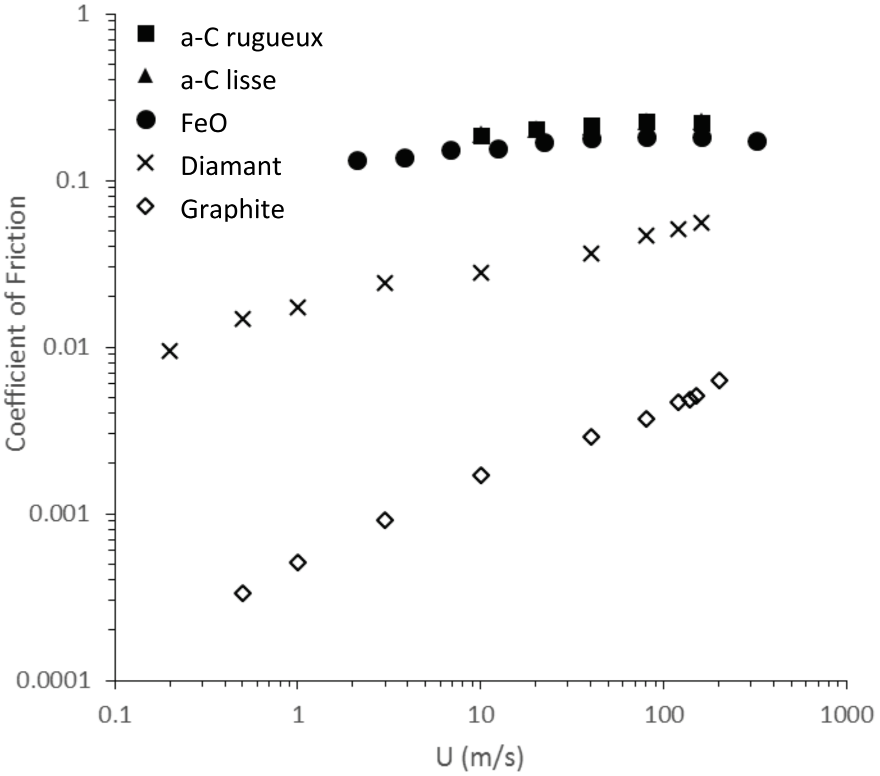

Figure i-14. Coefficient de frottement du système cisaillé avec une charge normal de 500 MPa pour cinq surfaces différentes.

Dans les configurations où le cisaillement s'opère principalement dans le fluide (FeO et a-C), le glissement n'a logiquement pas d'influence sur le frottement. En revanche, dans les configurations où le glissement est prédominant, le frottement peut-être réduit de plusieurs ordres de grandeur.

i.6.2 Aux origines du glissement

Pour comprendre et maîtriser le phénomène de glissement, les différents mécanismes à l'œuvre sont étudiés. Notamment, il a été remarqué que la température avait un rôle assez limité dès lors que le glissement est important. A l'inverse, l'épaisseur de film a un effet important sur la quantité de glissement mais qui est complexe à appréhender car la variation de l'épaisseur de film modifie également le taux de cisaillement subit par le système.

En parallèle, la nature (géométrie et composition) des surfaces conditionne la présence de glissement. Une principale caractéristique de la géométrie des surfaces est leur rugosité (Tableau i-1).

	Graphite	Diamond	Smoothest a-C	Roughest a-C	FeO
$h_{rugosité}$ (Å)	0.0115	0.0534	0.5709	0.8202	0.0705

Tableau i-1. Rugosité géométrique pour les cinq différentes surfaces.

Un lien peut directement être fait entre la rugosité et la longueur de glissement puisqu'aux plus faibles rugosités correspondent des glissements importants, et inversement. La seule exception à la règle ici est pour l'oxyde de fer pour lequel un glissement relativement faible est observé alors que sa rugosité l'est également (à peine 32 % d'écart entre les rugosités du FeO et du graphite contre 3100 % d'écart entre leur longueur de glissement à 5 m/s). L'explication de cette singularité réside dans la nature polaire des atomes de l'oxyde de fer qui vont interagir plus fortement avec les atomes du LI et ainsi augmenter le frottement à l'interface.

i.7 Conclusion et perspectives

L'étude du comportement d'un liquide ionique en film très mince s'inscrit directement dans le cadre du développement de systèmes lubrifiés plus économes et plus performants. Dans cette étude, un liquide ionique (LI) avec des propriétés rhéologique comparable aux lubrifiants traditionnels a été considéré. Grâce à des simulations de dynamique moléculaire (DM) ses propriétés de transport et sa réponse au confinement nanométrique couplé à du cisaillement ont été étudiées.

Premièrement, plus de 200 simulations ont permis d'explorer les régimes linéaires et non-linéaires du LI en volume à différentes conditions de pression, température et cisaillement. Cela a notamment permis de proposer une amélioration des modèles de rhéologie actuels pour mieux prédire la viscosité à fort taux de cisaillement.

Deuxièmement, les simulations du LI nano-confiné et cisaillé ont révélé que le cisaillement était accommodé par deux mécanismes bien distincts : la déformation du fluide et le glissement à l'interface liquide/solide. Chacun ayant un rôle clé dans la saturation de la contrainte de cisaillement aux hauts taux de cisaillement. Concernant le premier, les influences de la température et de la rhéofluidification ont été étudiées en détails et un modèle de prédiction de la température dans le nanoconfinement a été proposé.

Enfin, l'influence de la nature des surfaces a été caractérisée. Certaines surfaces très peu rugueuses sont à l'origine de glissements de vitesse très importants à l'interface liquide/solide, à tel point que le glissement peut-être prédominant dans des systèmes où l'épaisseur de film atteint le micromètre. En revanche les surfaces plus rugueuses ou polaires interagissent plus fortement avec le fluide et le glissement n'est alors significatif qu'à des épaisseurs de l'ordre de l'Angstrom ou du nanomètre.

Des travaux complémentaires pourraient mener à une connaissance encore plus approfondie des mécanismes de lubrification.

D'une part, étudier au moyen de simulation de DM d'autres liquides ioniques et avec d'autres composants (eau, additifs, …) permettrait de vérifier la généralité des résultats obtenus dans cette étude et d'avoir un aperçu de l'influence des différents composants.

D'autre part, les mécanismes menant à la saturation de la contrainte de cisaillement mériteraient d'être explorés avec des fluides et surfaces de différente nature.

Enfin, les glissements très importants observés avec quelques surfaces doivent être retrouvés au moyen d'essais expérimentaux réalistes pour qu'une application industrielle concrète soit envisageable.

Nomenclature

Roman symbols

A_{rms}	[Å], [nm]	Root mean square roughness amplitude of the surface
COF	Dimensionless	Coefficient of Friction
D	[Å²/s]	Self-diffusion coefficient
E	[kcal/mol]	Total potential
E_{angle}	[kcal/mol]	Angle bending potential
E_{bond}	[kcal/mol]	Harmonic bond potential
E_{bonded}	[kcal/mol]	Bonded interaction potential
$E_{dihedral}$	[kcal/mol]	Dihedral potential
$E_{non-bonded}$	[kcal/mol]	Lennard-Jones and Coulombic interaction potential
$E_{Tersoff}$	[kcal/mol]	Potential steming from the Tersoff force field
F_c	[kcal/mol.Å]	Conservative force derived from the total potential
F_{corr}	[kcal/mol.Å]	Corrugation force from the scanning technique
F_l	[kcal/mol.Å]	Long-range forces
F_s	[kcal/mol.Å]	Short-range forces
$F_{p,i}$	[kcal/mol.Å]	Confining force applied on the atom i of the surface
$g(r)$	Dimensionless	Radial distribution function
h	[Å], [nm]	Film thickness
H	Dimensionless	Dimensionless film thickness
k	[W/m.K]	Thermal conductivity of the fluid
k_B	[J/K]	Boltzmann constant
K_a	[kcal/mol.deg^2]	Half spring stiffness of the angle bending potential
K_b	[kcal/mol.Å^2]	Half spring stiffness of the harmonic bond potential
$K_{d,i}$	[kcal/mol]	Spring stiffeness of the mode i of the dihedral potential
l_k	[Å]	Kapitza length
L_s	[Å]	Slip length
m	[a.m.u.]	Atom mass
$m_{mol,i}$	[a.m.u.]	Mass of the molecule i
N	Dimensionless	Exponent for the shear thinning behavior in fluids
n_c	Dimensionless	Number of atoms in the control domain of the walls
n_{mol}	Dimensionless	Number of fluid molecules in the system

p	[kcal/mol.Å.fs]	Momentum transfer in the Müller-Plathe method
P	[Pa]	External pressure
PVC	[1/Pa]	Pressure viscosity coefficient
P_{conf}	[Pa]	Confining pressure
$P_{\alpha\beta}$	[Pa]	Indenpendent components of the fluid stress tensor
Q	[e]	Generated energy per unit volume
q_i	[e]	Atomic partial charge
r_{ij}	[Å]	Distance between two atoms i and j
r_0	[Å]	Equilibrium interactomic distance
S	[Å^2]	Area of the contact nano-patch in the Molecular Dynamics simulation
t	[s]	Time
t_{rel}	[s]	Relaxation time of the fluid
T	[K]	Fluid temperature
T_{wall}	[K]	Imposed wall temperature
U	[m/s]	Relative shearing velocity of the surfaces
V	[m^3]	Volume of the simulation domain
v_{slip}	[m/s]	Velocity jump at the liquid/solid interface
w_c	[m/s]	Weighting factor of the ionic liquid partial charges
$\boldsymbol{x}$	[Å]	Atom coordinates
$\dot{\boldsymbol{x}}$	[Å/fs]	Atom velocity
$\boldsymbol{x}_i$	[Å]	Coordinates of the atom i
$\boldsymbol{x}_s$	[Å]	Temporary atom coordinates computation
$\dot{\boldsymbol{x}}_s$	[Å/fs]	Temporary atom velocity computation
z_0	[Å]	Position of the film thickness center

Greek symbols

α_{CR}	[deg]	Cation's specific orientation angle
α_{AC}	[deg]	Anion's second specific orientation angle
α_{AS}	[deg]	Anion's first specific orientation angle
β	Dimensionless	Temperature-viscosity coefficient
$\dot{\gamma}$	[1/s]	Shear rate of the bulk fluid
$\dot{\gamma}_{app}$	[1/s]	Apparent shear rate of the confined system
$\dot{\gamma}_{eff}$	[1/s]	Effective shear rate of the confined fluid
δt	[fs]	Time step of the short range interactions
Δt	[s]	Leading time step of the Molecular Dynamics simulations
ΔT	[K]	Temperature jump at the liquid/solid interface
ε_{ij}	[kcal/mol]	Lennard-Jones energy interaction parameter between atoms i and j
ε_0	F/m	Electric permitivity constant
η , η_{bulk}	[mPa.s]	Fluid viscosity in bulk conditions
η_0	[mPa.s]	Fluid viscosity of the Newtonian plateau
η_c	[mPa.s]	Fluid viscosity predicted by he Carreau model
η_{eff}	[mPa.s]	Effective fluid viscosity under confinement
θ_{ijk}	[deg]	Angle between three consecutively bonded atoms i, j and k
θ_0	[deg]	Equilibrium angle of the angle bending potential
λ	[mPa.s/Å]	Interfacial liquid friction
R_{th}	[m^2.K/GW]	Thermal resistance
ρ	[kg/m^3]	Average lubricant density in the film
ρ_N	[molecule/nm^3]	Average number density of a molecule
σ_{ij}	[Å]	Lennard-Jones distance parameter between atoms i and j
σ_{scan}	[Å]	Lennard-Jones distance parameter for the scanning atom
τ	[Pa]	Shear stress
φ_{ijkl}	[deg]	Dihedral between four consecutively bonded atoms i, j, k and l
ϕ_q	[m^2/GW]	Heat flux at the liquid/solid interface

Introduction

Among contemporary sciences, the one of interacting bodies in relative motion, referred to as Tribology, gathers many investigations of the scientific and industrial communities. Firstly, it has applications in countless manufacturing domains and in everyday life situations. The friction, wear, vibration and heat resulting from the rubbing of two surfaces are continually looked to be controlled or reduced to reach maximum performance of a system. Secondly, tribology science embraces the development of various other disciplines such as material science, mechanics or chemistry. Hence, the different approaches to progress in the field are often multidisciplinary.

For the cases where friction and wear are looked to be reduced, the most commonly used solution is the introduction of a fluid third body between the two sliding solids. Owing to their wide presence in industrial applications, such lubricated systems represent an essential share of investigations in Tribology. Regarding the recurrent environmental and economic issues, researches mainly focuses on the sustainability of lubricated systems. Hence, both life expectancy and energy consumption aim to be optimized and "green" materials intend to replace the classical harmful ones.

To meet these challenges, several fluids are currently studied as an alternative to conventional lubricants. Among them, ionic liquids exhibit very promising properties to deal with common lubricating issues and, in particular, in extreme working environments. In addition, their high electrical conductivity opens the way to new fields of application.

The desired reduction of energy consumption often implies a significant downsizing of the systems. Hence, current lubricated contacts present film thicknesses close to the micrometer and the ongoing developments go towards nanometers for the future. At this scale, phenomena introduced by the physical-chemistry of the involved materials are intensified and superpose to the classic lubrication mechanisms. Dedicated approaches are then essential to accurately predict the behavior of the tribological contact at the tiniest scales.

In the present work, a model ionic liquid is studied in very thin film. The approach is mostly computational and focuses on transport properties. By means of molecular simulations, the response of the ionic liquid to extreme stresses and nanoconfinements is analyzed in detail to evaluate its lubrication potential.

The present manuscript consists of five chapters.

First, **Chapter I** presents a brief history of tribological systems until their adoption by the contemporary industries. A state of the art of the usual issues of lubricated systems in operating conditions is drawn up. From there, weaknesses in the knowledge of current and future lubrication mechanisms are identified. In particular, the prediction of the lubricant film thickness is a key asset for the conception of enhanced lubricated systems. Next, the lubrication mechanisms occurring at the nanoscale are reviewed. Above all, the structuration of the fluid molecules, their interactions with the confining solid and the dynamics of the system are looked over, as many factors which impact the global performances of a lubricated contact. In this chapter, the response of ionic liquids to nanoscale confinement is also summarized as a comparison with the previously introduced mechanisms at this scale using more conventional fluids.

Molecular Dynamics, a numerical method able to model the physical behavior at the nanoscale, is introduced in **Chapter II**. The strengths and limits of the tool are also enumerated to justify its choice for this study. To lead the investigations, two main simulation systems are modeled: the bulk fluid alone and the fluid confined between two solid surfaces. The configuration of the different simulated domains is detailed and a validation of the model is done. Finally, the last section depicts how the quantities of interest are computed.

In the following three chapters, the results of the study are presented and discussed from the simplest system to the most complete ones.

First, from over 200 bulk fluid simulations, the rheological properties of the considered ionic liquid are analyzed in **Chapter III**. As the film thickness prediction is a growing issue with the reduction of film thickness and the subsequent increase of shear rate, a better knowledge of the lubricant rheological properties is essential. The rheological characteristics of the ionic liquid in the linear regime are calculated for several conditions of pressure and temperature. At this stage, a comparison is undertaken with experimental measurements to bridge experimental and computational studies of viscosity under highly-stressed states. Finally, from simulations at high shear rates, an enhancement of a classical analytical model is proposed to predict the viscosity.

The lubrication mechanisms occurring within very thin films are then investigated. A system composed of the ionic liquid confined between surfaces representative of a classic steel-steel contact is modeled in **Chapter IV**. To broaden the knowledge on the physical behavior of ionic liquids under confinement, the static behavior of the configuration is first analyzed. Thus, from the structuration and orientation of the lubricant molecules near the liquid/solid interfaces, predictions can be made on the lubrication performances of the simulated system. One main objective of this study is to reveal the behavior of a highly confined lubricated contact and the mechanisms involved. With a relative motion imposed between the surfaces, the effective rheology of the system is measured for different velocities and the crucial role of temperature and of some interfacial phenomena is depicted. The discussion contributes to explain a current challenging mechanism at the heart of the research in lubrication, when friction is no longer dependent on the velocity of the surfaces.

To complete the picture of the nanoscale contacts lubricated by an ionic liquid, the influence of the confining surface nature is valued in **Chapter V.** In particular, presumed very efficient anti-wear coatings are implemented in the simulations to be tested under highly stressed lubrication conditions. In this manner, the dynamical responses of five different materials with different compositions and structures are compared. From these responses, the consequences on macroscale lubrication are estimated. Once again, the underlying mechanisms are detailed to provide the opportunity to better design the lubricated systems of the future.

Chapter I: Context and state of the art

This first chapter firstly aims to explain the scientific and industrial interest in the issues concerning lubrication in very thin film with ionic liquids and secondly to draw up a state of the art of the related knowledge. After a brief history of the lubrication science, the current related challenges are introduced in a first section. As severe working environments and the current trend to downsize systems lead to significant reduction of the lubricated contact thickness, a next section is dedicated to the lubrication mechanisms at the smallest scales. In a last section, an overview of the lubrication capabilities at this scale is presented for potential alternative lubricants: ionic liquids. The goals of this study are then detailed.

I.1 Lubrication Theory

In this first section, the history of lubricated systems is presented, from their apparition in wide domains, to the specific challenges in today development of new technologies. Especially, a focus is made on the prediction of the lubricant rheology in highly stressed systems, when the behavior is the most difficult to apprehend.

I.1.1 Tribology: From the first uses to its technological development

Tribology has been an everyday life science long before it even got its name. Since the first time a human tried to make fire by rubbing stones or pieces of wood together, the number of applications involving friction has increased continuously over the centuries along with the development of civilizations and their technologies. To control friction, complex methods were early developed, as demonstrated by the use of primitive lubricants like water, sand or animal fat before 4000 B.C. [32]. With the development of transport, energy and manufacturing industries, the science of tribology became a central question to optimize a system’s performance as first evidenced by the 1966 Jost report, which estimated that improvements in tribological principles of industry (lubrication, maintenance, etc.) could, at the time, save the British economy £500 million per year.

Despite the key role of friction in society, its first theorization dates back to the Renaissance and is attributed to Da Vinci [32]. He introduced the friction coefficient defined as the ratio between the force resisting the relative motion of two bodies sliding against each other and the normal load holding those bodies in contact. He initially established the independence of the coefficient from the surface contact area. His work was rediscovered two centuries later by Amontons who generalized it. Coulomb, better known for his work on electrostatic forces, also played his part in the development of the friction theory by testing the influence of the surface roughness and showing that, in most cases, friction doesn’t vary with the sliding velocity. It was Hirn who, after an extensive experimental work in 1847, first introduced the fluid lubrication to the study of friction [32]. Even though he supported Coulomb’s observations on how friction does not change in relation to sliding speed for dry contacts, he highlighted a significant variation of the coefficient of friction in relation to speed for lubricated contacts. From then on, the sciences of dry contacts and fluid-lubricated contacts took different directions as the physics involved in both situations digress.

New approaches were advanced to quantify friction of a lubricated contact. In 1886 Reynolds included the influences of temperature and theorized the specific rheology of the thin lubricant films [33]. In 1902 Stribeck proposed a continuous profile of friction variation with three distinct lubrication regimes that depend on the velocity, the lubricant viscosity and the load applied to the system (Figure I-1) [34].

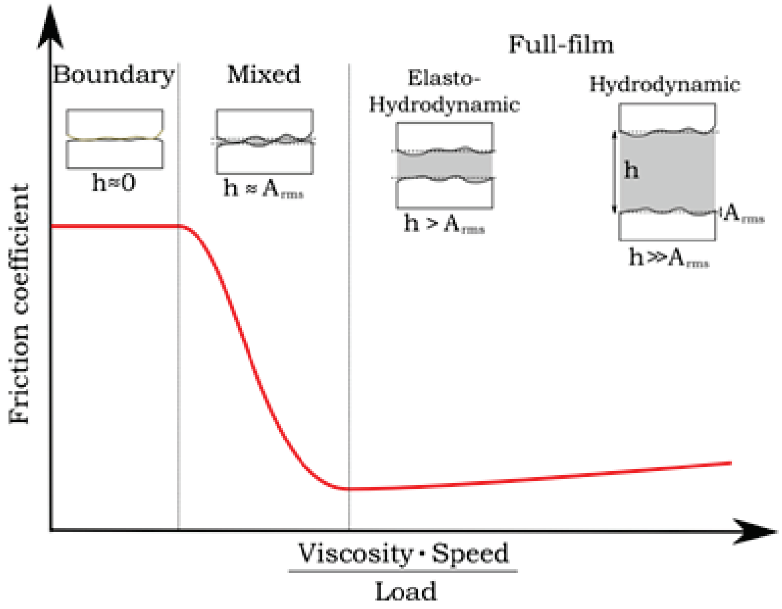

Figure I-1: Stribeck curve, representing the qualitative dependence of the friction coefficient with operating conditions. A comparison between the contact thickness *h* and the root mean square roughness amplitude A_{rms} of the surfaces is also shown. From Savio [15].

Finally, the complexity and the diversity of today lubricated contacts requires more than the understanding of their mechanical behavior. Depending on the involved solids and potential lubricants, it is essential to consider many variables like potential chemical reactions, the material properties and the dynamics of the system to design a complete tribological system (Figure I-2).

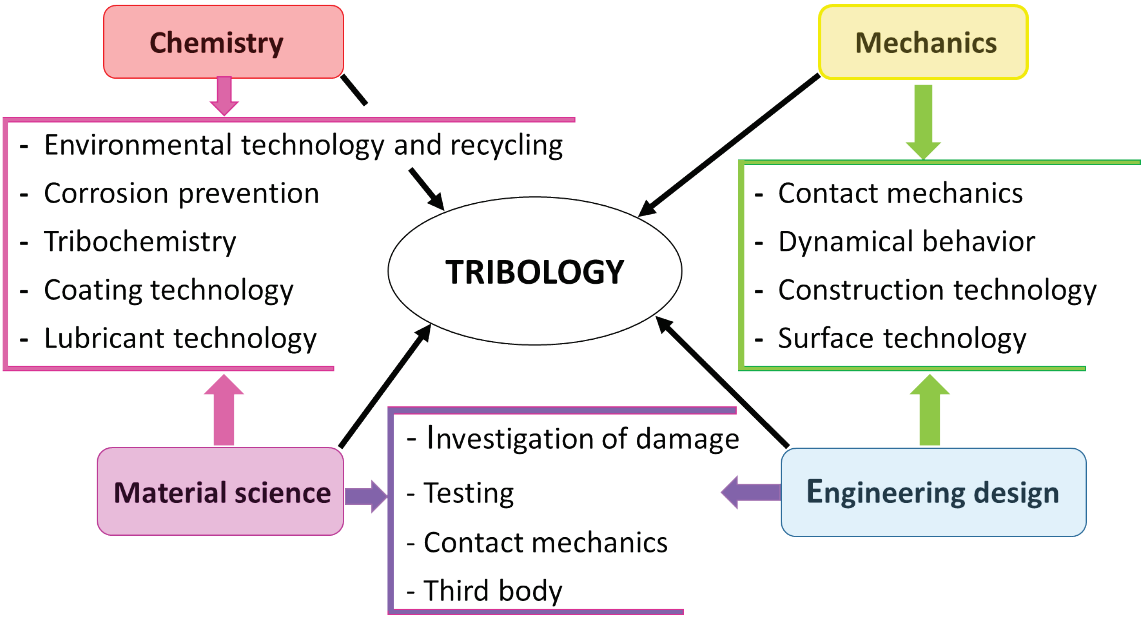

Figure I-2: Tribology: A multidisciplinary science

I.1.2 Lubrication regimes

The Stribeck curve displays three distinct lubrication regimes (Figure I-1). At low sliding speeds, high loads or low viscosities, a "boundary regime" takes place as the two sliding surfaces are in direct contact. In this regime, the friction is independent of the velocity as suggested by Coulomb. At higher speeds, higher viscosities or reduced loads, some lubricant is dragged in between the shearing surfaces creating a partial fluid film between them. In this "mixed regime", the film thickness is about the size of the surfaces' asperities. During this transition regime, the more the surfaces are separated by the lubricant, the more the friction is reduced. Finally, when the film thickness is higher than the asperities, the load is entirely supported by the hydrodynamic lift as a "full film regime" is in place and the friction only slightly increases with the shearing speed. Moreover, as there is no direct contact between the sliding surfaces, the wear of the surfaces is negligible. Therefore, this regime is the one sought to achieve the maximum performances in lubricated systems.

In full-film regime, two sub-regimes are distinguished depending on the nature of the contact geometry. For surfaces of conforming bodies (eg. journal bearings, see Figure I-3a), the resulting nominal pressure is weak enough not to deform the solids. In this case, the lubrication is hydrodynamic (HD) and the friction increases (linearly for Newtonian fluids) with the sliding speed. On the other hand, non-conforming surfaces (see Figure I-3b) induce a high local pressure in the contact, generating significant deformations of the bodies [35], and a modification of the properties of the piezoviscous, compressible and temperature-dependent lubricant [36–39]. This will considerably modify the fluid flow in the contact [39–41] and the resulting friction [42–44]. To study this so called elasto-hydrodynamic (EHD) regime, the multiple contributions to the global tribological response require the development of multi-physical computational methods [43–47]. As industrial lubricated systems are mostly subject to the EHD regime, it is essential to understand the underlying mechanisms to better predict and control the dynamics and the resulting performances.

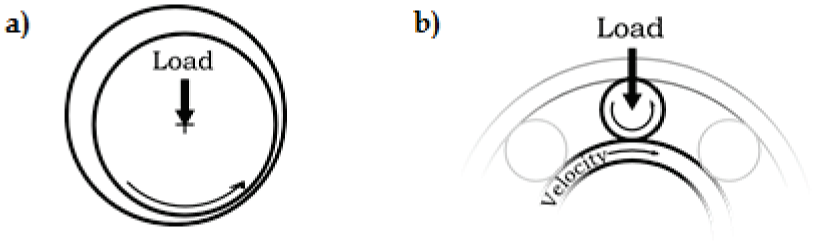

Figure I-3. Schematic representation of contacting geometries. a) Conforming: shaft rotating in a journal bearing. b) Non-conforming: Roller-raceway contact in a bearing

Finally, the industrial surfaces of mechanical transmissions usually present roughness lower than a tenth of a micrometer. Hence, the lubricant films in the EHD-lubricated systems can reach thicknesses of the same scale. Such thin films exhibit very specific rheology that must be study into details.

I.1.3 Thin film rheology

In thin films, one key element of the lubricated system performance is the lubricant film thickness. In fact, as depicted in the following section, friction and wear are greatly impacted by its variations. Nevertheless, its value cannot be directly controlled in the contact of a working lubricated system but mostly depends on two of the fluid properties: the viscosity and the pressure-viscosity coefficient (PVC). Hence, the estimation of those quantities is the first step to predict the lubrication performances of a system.

The PVC quantifies the influence of the pressure on viscosity. In the past decades, it was evaluated through experimental and numerical works for different kinds of fluids [48–50]. Viscosity and PVC vary with temperature and density, which are far from being homogeneous in a working contact. Therefore, a characterization of both values over several temperatures and densities is needed to accurately predict the film thickness for a specific lubricant. Over the past ten years, this characterization has been done for fluids of different natures (hydrocarbons and ionic liquids) [1–4].

As thin films generally come with high shear rates, shear thinning might occur leading to a non-Newtonian behavior of the fluid. Further investigations were then necessary to enhance the film thickness prediction at high shearing conditions. The Carreau analytical law is able to describe the viscosity drop caused by the shear thinning for classic lubricating oils [51]:

$$\eta = \eta_0 [1 + (t_{rel} . \dot{\gamma})^2]^{\frac{N-1}{2}} \qquad (\text{I. }1)$$

with the Newtonian viscosity η_0, the relaxation time t_{rel} and the exponent N, three values inherent to the fluid, and $\dot{\gamma}$ the shear rate. Several numerical analysis also validated the Carreau model for different kinds of alkanes and isomers [52–54]. Both the Newtonian viscosity and the relaxation time depend on pressure and temperature, but the exponent N is traditionally considered as constant for a given fluid. This statement will be further examined in Chapter III.

Finally, thin films exhibit a complex rheology that could be quantified numerically. However, when it comes to very thin film (0.1-10 nm), the dimensions of the studied contact are close to the lubricant molecular size, so a multitude of local phenomena can come as well into play.

I.2 Molecular lubrication

The present section explores the lubrication mechanisms at stake when the film thickness tends toward 10 - 0.1 nm. The context of the apparition of such very thin films is first described. An overview of the different numerical and experimental tools used to investigate those films is then given. Finally, the known molecular lubrication mechanisms occurring in very thin films are depicted one by one and some lacks in their understanding are identified.

I.2.1 From local to global film thickness reductions

Lubricated systems are generally designed to work in full-film regimes where friction and wear are low. However, upon severe conditions, only a few tenth of a nanometer would separate the junctions between surface asperities peaks which represent a sub-region of the whole contact area (see Figure I-4 a → b → c → d) [55]. Moreover, due to economic and environmental constraints, the size of the elements and the quantity of lubricant tend to be reduced, leading to a global film thickness reduction [56]. Simultaneously, recent progress in manufacturing technics gives the opportunity to design very smooth surfaces [55], which ones, coupled with low viscosity lubricants as cooling fluids or ionic liquids, favor molecular lubrication (see Figure I-4 a → e → d) [57,58].

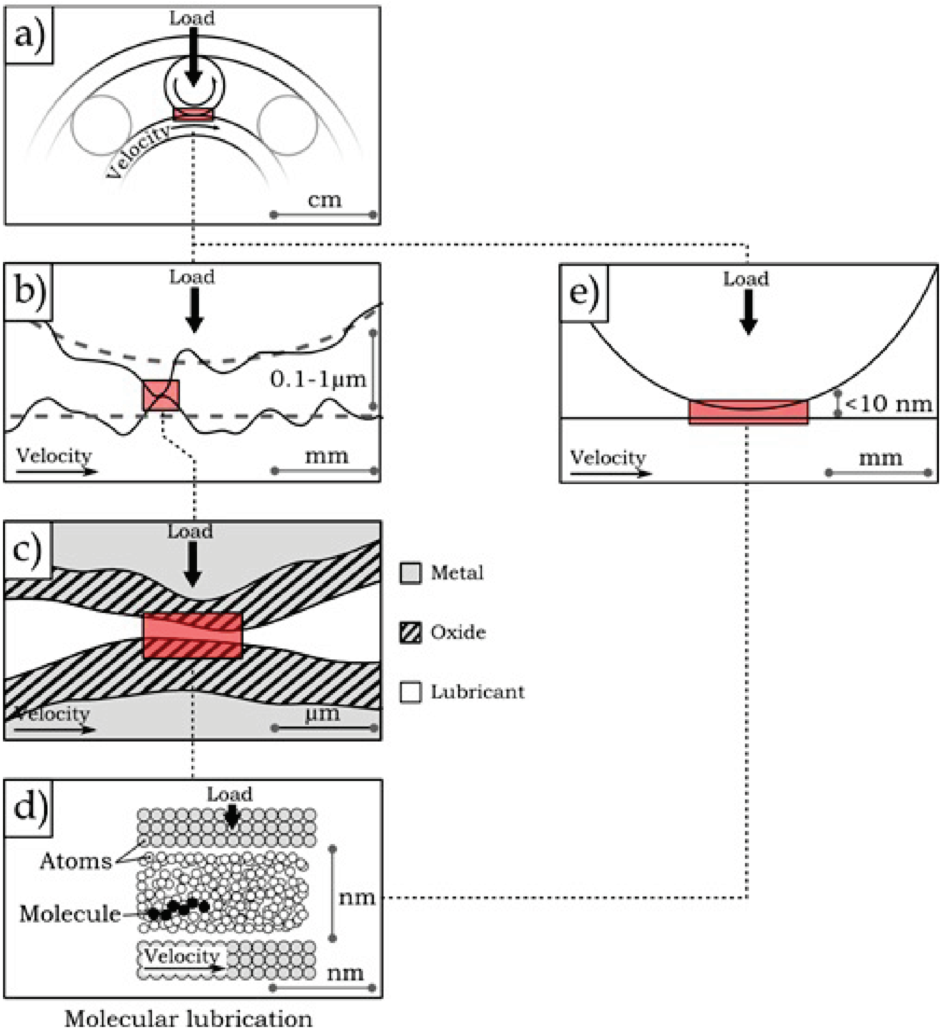

Figure I-4: Multi-scale nature of a lubricated contact problem with film thickness reduction: from a macroscopic application to molecular lubrication between surface asperities (a → b → c → d) or between very smooth surfaces (a → e → d). From Savio [15].

Although molecular lubrication has becomes a central concern in lubrication, it is far from being fully mastered as researches on the subject are relatively recent and the nanoscale regime is complex to investigate. Dealing with molecular confinements, the film can no longer be considered as a continuum medium. The fluid molecules must be studied as individual elements to apprehend the global behavior of the contact. This discrete nature of the fluid comes with a rich phenomenology resulting from local discontinuities. The latter are introduced by the liquid/solid interface featuring specific structuration, segregation of lubricant additives, hydrodynamic slip and physi- or chemisorption, and by the non-trivial rheology of the fluid which depends on different factors (thermal dissipation, molecular layering and arrangement and shear thinning). Today's studies on nanoscale thin films focus on the understanding of those phenomena to improve the prediction of the whole lubricated contact response and enhance its performances.

I.2.2 Investigation methods

It is impossible with the current technology to directly look at an operating nanoscale lubricated contact and instantly figure out the mechanisms of molecular lubrication. Nevertheless, by coupling experimental measurements and numerical simulations, it is possible to get a global insight of the lubrication process for various lubricants, confining surfaces and operating conditions.

Experimental approaches

Bhushan and coworkers reviewed the various apparatuses and methods developed to investigate confined fluids at the nanoscale [59].

In the late 1960s, the first measurements of interactions between two surfaces separated by a molecularly-thin fluid film became possible with the development of the Surface Force Apparatus (SFA) [13]. Two perpendicular cylinders are brought in contact and the contact area is estimated by means of optical interferometry [60] or capacitive methods [61]. Through the piezoelectric crystals which drive the two solids, the distances and the forces are measured with a precision of respectively 0.1 nm and 10 nN or even better with the most recent devices. Therefore, accurate evaluations of the static and dynamical properties of nanothick fluid films confined between smooth surfaces were achieved.

In 1981 a second instrument named Scanning Tunneling Microscope (STM) was designed. It allows to picture clean surfaces as well as lubricant molecules using the electrical conductivity of some surfaces [62].

Finally in 1985, the Atomic-Force Microscope (AFM) [63] and its by-product, the Friction-Force Microscope (FFM) have been the most remarkable discoveries of the last decades among the experimental tools used at the nanoscale. With a probe tip scanning the studied surface, it can measure extremely low forces with a precision better than 0.1 nN. To achieve this performance, the probe tip is attached to a cantilever whose deflections are evaluated by a laser beam. With the classic AFM, topographical measurements, adhesion or electrostatic force estimations can be carried out on a surface, with or without fluid, providing valuable information on the wear, the indentation, the transfer of material, etc. it endured. Subsequent modification of the original apparatus led to the development of the FFM, able to measure forces tangential to the surface.

Numerical approaches

Simultaneously, the exponential progress in the computing field enabled a fast development of numerical tools that would supplement the experimental studies on molecular lubrication. As previously noticed, at the nanoscale, solids and liquids are better described by their elementary components: the atoms. Classic simulations include up to millions of discrete elements, so the dimensions of the modeled domain extend from the Angstrom to a ten of nanometers. Similarly, simulation times last from picoseconds to a fraction of a microsecond in time-explicit simulations. Hence, molecular simulations provide a glimpse of the system at the nanoscale, in a steady state or in an ultra-fast transient state.

To model materials at the atomic scale, two methods are most recurrently used. The first, Monte-Carlo (MC) [64,65], is a statistic approach designed to determine the equilibrium properties and configuration of molecular systems in specific thermodynamic ensembles. Atomic configurations are generated randomly but are kept only if they fulfill a condition depending on their energy state. Hence, in MC simulations, the potential energy is computed but the time is not. This means that there is theoretically no limit to model features with quasi-infinite characteristic times. As a consequence, few computation steps are usually required to get to the equilibrium state, opening the way to simulate systems with a large amount of particles. However, without time reference, it is not possible to solve the dynamical behavior of non-equilibrium systems. Nevertheless it remains a preferred tool to work out the structuration and the molecular arrangement in complex systems.

Molecular Dynamics (MD) simulation is a deterministic approach in which the Newton's equations of motion governing each atom are explicitly solved. Therefore, it becomes possible to study non-equilibrium systems [66]. On the other hand, since time is computed explicitly, simulations usually do not exceed a few tens of nanoseconds. Very complete systems can be modeled with the MD tool to reveal qualitative phenomena (structuration, velocity profiles, molecule segregation, etc.). A large set of physical quantities can also be derived (viscosity, thermal or electrical conductivity, friction, energy, etc.). More details on the potential and the computational aspects of MD simulations will be given in Chapter II.

The following section reviews the investigations on molecular lubrication mechanisms, both experimental and numerical approaches are used to apprehend the various involved phenomena.

I.2.3 Molecular lubrication mechanisms

In the following are described some effects occurring at the nanoscale that have influence on the global lubrication performances. First is depicted the influence of the contact thickness on the system global response. The structuration of the confined fluid molecules is then described. A picture of the consequent dynamics near the fluid/solid interfaces is presented. Finally, the influence of the temperature variations on the fluid rheology is introduced.

Nano-rheology

A first specificity of the molecular lubrication is the possible alteration of the rheological behavior of the very thin lubricant film. In fact, the fluid cannot be treated as a homogeneous medium because its viscosity can change with the variation of some of the operating conditions. Especially, local variations of the effective shear viscosity are caused by the re-arrangement of the molecules in structured assemblies up to their crystallization.

When typically less than ten molecule layers remain in the gap between the two confining surfaces, the viscosity dramatically increases as the thickness keeps being reduced. It has been first highlighted by SFA experimental assessments on hexadecane [10] and confirmed with different numerical simulations on n-dodecane [6,7] and on model fluids [8,9]. This sudden rise is attributed to the formation of long range structures across the narrow fluid film.

When the lubricant film is made of only 1-2 molecule layers it undergoes a solid-like behavior as the fluid tends to crystalize, and so its viscosity is several orders of magnitude higher than the bulk one [10,11]. Under those conditions, shearing is no longer a continuous movement but a succession of stick and slip phases of the lubricant molecules at the liquid/solid interface. The phenomenon was detected experimentally [11] as well as using numerical simulations [9,67] and always comes with very high pressures.

Finally, independently of the contact thickness, at high shear rates the motion is more steady and the viscosity evolves as a negative power law with the shear rate: $\eta \propto \dot{\gamma}^{-n}$, with $\dot{\gamma}$ is the shear rate and $n \in [0.5;1]$ [9,68–70]. When the viscosity reaches its bulk value, it stays constant [71] (see Figure I-5). This mechanism is different from the non-Newtonian shear thinning effect depicted in a following section. In fact, shear thinning occurs at high to very high shear rates (see Figure I-5) [51] whereas the previously described solid-like behavior only occurs at low shearing [72].

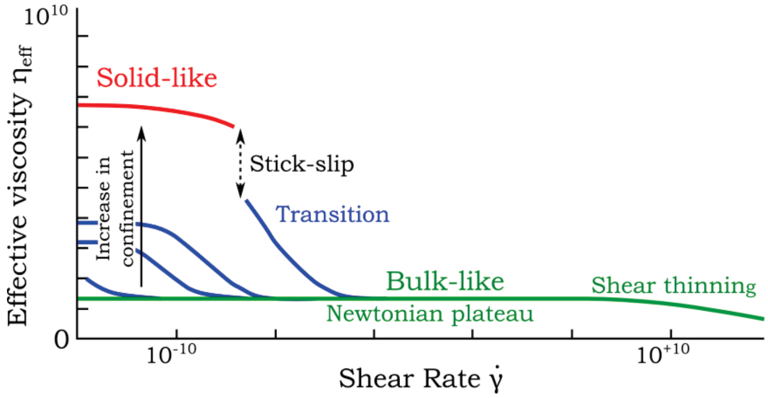

Figure I-5. Generalized map in arbitrary units for the effective viscosity of confined films as a function of the shear rate, load and film thickness. Inspired by Luengo et al. [71]**.**

This complex relationship between the contact film thickness and the effective rheology in nanoconfinements also depends on the nature of the involved lubricant and surfaces. The size and shape of molecules define the solidification threshold: smaller and regular molecules would tend to arrange and solidify more easily at lower pressures or higher thicknesses [6,13,14].

Effective for any nano-confined liquid, the structuration of the molecules near the liquid/solid interface also governs the rheology of the lubricant at the nanoscale.

Structuration at the interface

When a liquid is in contact with a non-deformable body, a tidy arrangement of the fluid molecules occurs at the liquid/solid interface. The lubricant molecules tend to structure in distinct dense layers that change the local mobility (see Figure I-6). Layering is a direct consequence of the liquid/solid interaction. As the solid surface keeps its plane structure, its atoms uniformly interact with the fluid ones in the two directions of the plan. In response, the closest fluid molecules to the wall will lay parallel to the surface in a dense layer that can reach several times the bulk density. This first structure is located at the equilibrium point defined by the liquid/solid interactions stemming from the Van der Waals and Coulomb forces [13,73]. The formation of a first dense layer modifies the classical isotropic interactions inside the fluid. As a consequence, a second layer will form next to the first one, and so on, other layers develop away from the solid. Nevertheless, the irregularities of the molecules shape and the thermal agitation cause the layers to be less and less organized away from the wall. The structuration can be apparent up to ten molecular diameters away from the surfaces when the conditions favor the ordering [12]. Beyond this limit, the fluid becomes isotropic again with bulk properties that can be predicted by classic fluid dynamics models.

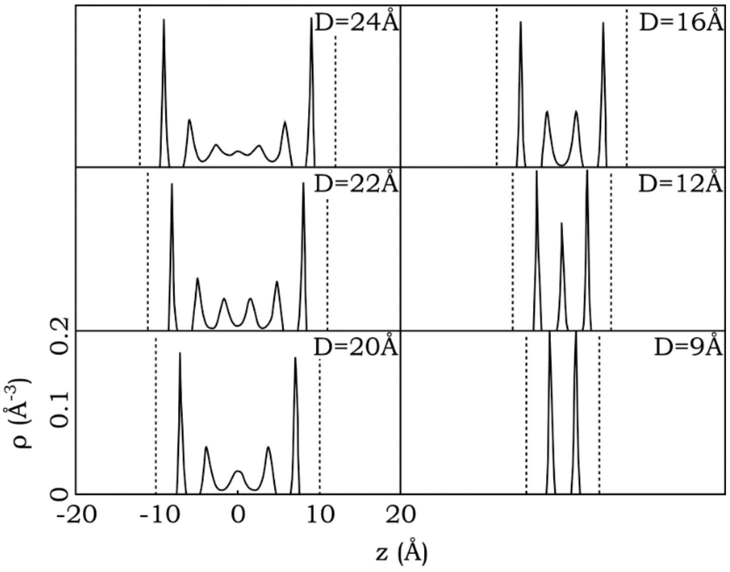

Figure I-6. Density profiles across the lubricant film (z-direction) for a confined Lennard-Jones fluid. The distance *h* between the walls (dotted lines) is varied from 24 to 9 Å, corresponding to 7 to 2 molecular layers. Results from Gao et al. [14].

Many factors influence the formation of the organized structuration. Horn early found out experimentally that the molecule size impacts the layers density and width and that the chemical surface properties and the water content can strongly modify the first layer amplitude [13]. Similarly, at the liquid/solid interface, Thompson analyzed through molecular dynamics simulations the relation between the surface topographies and molecule geometries [74]. At high pressure, it appeared that fluid film crystallization was favored when the surface structure and the fluid can interpenetrate (condition often reached when the solid density is close to the molecule one and the fluid/solid interactions are strong).

Furthermore, various numerical works have shown that the presence of nanoscale roughness on the surfaces will disturb the molecular ordering and the glass transition [69,75,76], as well as macroscale rough surfaces will [70,75,77]. The layering was however found to be insensitive to temperature [13] and to high shearing [8,78–80], although it dramatically reduces the crystallization capability of the fluid molecules [72].

Finally, branched molecules also reduce the structuration capability [9,14,81,82]. However the effect on the rheology response is more complex. Even if the reduction of the structuration comes in this case with less crystallization [4,82], and so less friction at low shear rates, at high shearing conditions, the structured area induces high viscosity as the branched molecules lock the layers together.

Interfacial flow

In addition to the structuration of the lubricant, shearing with high confinement induces local interfacial phenomena in the dynamics of the flow. In regard to the size of the considered systems in the molecular lubrication regime, they have a non-negligible influence on the apparent properties of the lubricated system. Two interfacial flow patterns are identified at the liquid/solid interface: slip and locking [15]. Since the local dynamics of nanoscale films under severe operating conditions is difficult to access through experimental tests, most of the following observations stem from Molecular Dynamics investigations.

When the forces induced by the liquid/solid interactions are smaller than the cohesion forces of the fluid, molecules will slip on the surface (see Figure I-7). The occurring hydrodynamic “wall-slip” thus depends on both the interfacial interactions and on the viscosity of the fluid. The interfacial interactions controlling the tangential friction force are embodied by the fluid friction, λ, defined as the ration between the shear stress τ and v_{slip}, the velocity slip at the liquid/solid interface. Also, as a part of the shearing is absorbed by the interface a differentiation has to be made between the apparent shear rate of the confinement and the effective one experienced by the fluid. The slip length, L_s, defined as the ratio between the interfacial velocity jump and the effective shear rate is then introduced to quantify wall-slip at one liquid/solid interface. Three critical regimes are then identified : perfect slip when $L_s \rightarrow \infty$, partial slip, and no slip when $L_s \rightarrow 0$ [16]. When large slip is reached, it was experimentally observed that it can have a significant impact on the friction at the macroscale [16].

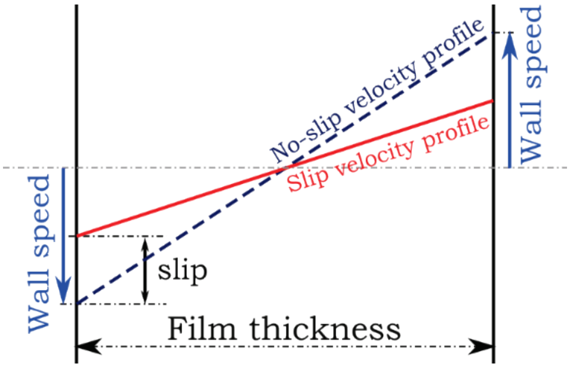

Figure I-7. Schematic representation of wall slip in a nano-confined fluid under shearing.

Wall slip is frequently found in molecular simulations of fluids sheared between smooth surfaces [8,78,83]. Standard values of the slip length are a few nanometers for alkanes confined between materials with crystalline structures [83], but can reach the micrometer with very slippery materials as for water into carbon nanotubes [84].

As for structuration, wall slip is a multifactorial feature of molecular lubrication. The couple {surface, lubricant} is the prevailing factor as wall-slip is an interfacial phenomenon. In particular, two properties of the interface drive the fluid behavior: the wettability [85] which quantifies the adsorption capability of a fluid on a substrate, and the corrugation [17], often linked to the wettability, which defines the required energy to initiate a relative tangential motion at the interface. In particular, a weak corrugation encourages an increase of the hydrodynamic slip at the interface. As well, the liquid/solid geometry compatibility and the sliding direction may have also substantial influence [83]. Petrie and Denn early found that the molecule length and shape also impact the slip: longer and more complex chains reinforce the fluid cohesion and therefore favor slip [86]. Besides, a very limiting factor of the wall slip is the surface topography. Numerous experimental [16,87,88] and numerical [29,75,77,79] studies highlighted that nano- to micro-scale roughness significantly reduce interfacial slip. Similarly, Jabbarzadeh and coworkers found that flexible surfaces also tend to reduce it [89].

Variation of slip with the environmental parameters was also widely investigated. It results from molecular dynamics simulations that slip increases with shear rate [79,89,90] while it decreases with temperature as a consequence of the reduction of the liquid viscosity [79]. The slip dependence on pressure seems however more complex since observations differ according to the nature of the fluid and surfaces under investigation. With water and hydrophobic surfaces, the increase of absolute pressure tends to reduce the slip [91] while the opposite trend is observed with alkanes sheared in between copper oxide surfaces [92] for instance.

At last, the dynamics singularity referred to as “locking” occurs when the conditions for wall-slip to occur are not met, but when cohesion forces in the first layer(s) of fluid next to the interface are still stronger than the ones of the bulk. In that case, a 1-2 molecule thickness of fluid will be locked to the surface (no relative tangential movement). In this configuration the shearing entirely occurs within the fluid thickness excluding the extreme layers near the interfaces. Here, effective shear rate will be higher than the apparent one. Furthermore, lubricant additives are often use to enhance the lubrication performances of a contact. Those additives are designed to be strongly adsorbed on the surfaces, so it creates a "tribofilm" at the liquid/solid interfaces. This way, it prevents direct contact between the sliding surfaces that would cause dramatic wear and undesired high friction. With regard to the interfacial rheology, Berro evidenced that the presence at the interface of ZDDP - a common lubricant additive - will favor locking [17] (see Figure I-8).

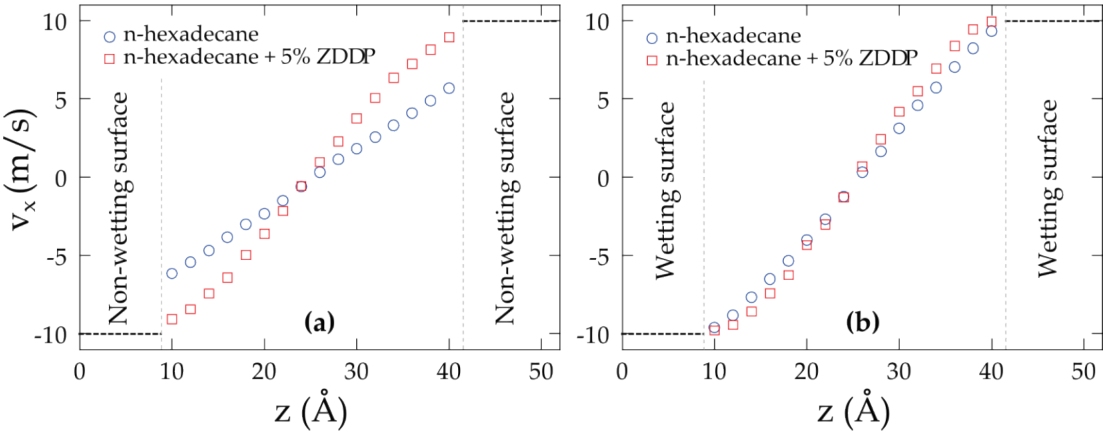

Figure I-8. Velocity profiles for pure hexadecane and a hexadecane-ZDDP mixture under confinement. Non-wettable (a) and wettable (b) surfaces are obtained by changing the wall-fluid interaction potential. Interfacial flow is modified by the physisorption of the antiwear additives (ZDDP) and surface wettability. Results from Berro et al. [17].

Interfacial thermal resistance

One last important aspect concerning molecular lubrication is thermic behavior within the contact. A temperature change of the materials directly impacts the performance of the lubricated system by modifying the fluid dynamics (viscosity, wall-slip) and stimulating corrosion and oxidation reactions. The severe conditions encountered in the molecular lubrication regime generate important heat which can be evacuated at various rates depending on the solid and fluid materials. In fact, the temperature elevation is controlled by the thermal resistance of the liquid/solid interface R_{th} and by the thermal diffusion of the confining solid that drains the heat out of the contact. A wise choice of lubricating and confining material is thus essential to prevent unexpected effects that would cause premature failure of the lubricated system.

In nanoscale systems, the temperature discontinuity caused by the interfacial thermal resistance R_{th} is even more important given that the diffusion in continuous materials operates over very small distances. The liquid/solid interfacial interactions impact the interfacial resistance R_{th} [17]. Indeed, an important wall-slip or well-structured layers reduce friction and heat generation by favoring the atoms mobility [29]. Though it must be noticed that important wall slip often comes with an important interfacial thermal resistance which drastically limits heat dissipation by the surfaces [93]. Lastly, the presence of classic additives at the interface increases the interfacial thermal resistance [17]. Depending on the value of R_{th}, the evolution of the fluid temperature significantly impacts the rheology at the nanoscale. If well controlled, this effect can be an asset to optimize the global lubricating performance of a system.

I.2.4 Questions still pending

The above review shows that the knowledge on the molecular lubrication mechanisms is already well mastered. The dependence of each phenomena on the considered materials and to the environmental conditions was widely studied. Nevertheless, different questions still remain. First, all the mechanisms were mostly characterized for very basic fluids, as Lennard-Jones fluids or linear alkanes with rather low number of carbon atoms. To define more precisely the lubrication regimes with classic oils, further investigations with more realistic fluids are essential. Then, the study of the interfacial flow can be more deeply explored. For instance, it was shown that the pressure can lead to opposite effects depending on the nature of the fluid involved. Moreover, some surfaces revealed their very slippery nature but still need to be tested under realistic lubrication conditions. The understanding of the relation between the wetting strength and the interfacial friction would also benefit from further work. Slip was also found to increase with shear rate, but a more precise description of its evolution would contribute to control the contact response. At last, as temperature has a direct influence on nano-rheology and potential chemical reactions, its impact shall be better characterized regarding to its influence on the interfacial thermal resistance.

In order to explore the lubrication process with a more realistic fluid lubricant, a fluid family is considered has it has recently proven its great potential to lubricate different kind of systems.

I.3 Ionic liquids as lubricants

Ionic liquids are introduced in this section. This kind of fluids presents numerous assets to consider it as alternative lubricant to commonly used oils. The potential of ionic liquid properties is thus first described. As they also exhibit interesting features for other applications (gas or energy storage, pharmaceuticals and solar thermal energy, among others), they have been largely studied in the last decades, including at the molecular scale. Based on the ensuing results, a brief review was undertaken on the lubrication mechanisms specific to ionic liquids, from the rheological properties of the bulk fluids to their dynamics and interactions with the surfaces at the nanoscale. The known limits of ionic liquids as lubricants were also evaluated and, finally, the remaining issues on the ionic liquids lubricating mechanisms were summarized.

I.3.1 Ionic liquids promising properties

With the aim to find more performing lubricants, several fluids with promising properties (thermal stability, high PVC, high or low conductivity…) have been considered. Some were already tested to reveal their behavior as nanoconfined films or at a surface interface, either with an experimental approach: water and aqueous solutions [94–96], glycerol mono-oleate (GMO) [97], fatty acid [98,99], oligomers [100], or using molecular numerical simulations: glycerol [101], alcohol [102], fatty acid [103]. The studies revealed interesting properties for lubrication applications, but all of those fluids also present some limitations to be widely adopted as lubricants. Furthermore, another family of fluids, very well studied in the physical chemistry literature, seems to have extremely promising properties to be used as lubricants: ionic liquids [20].

Room temperature ionic liquids (RTILs), often referred to as ionic liquids (ILs), are liquid salts at ambient temperature and pressure, made of atomic or molecular ions [18]. Given the considerable diversity of cations and anions, there is a tremendous number of possible combinations of ions with some estimations reaching 10^{18} possibilities [19] (see in Figure I-9 the most common ions). Most ILs are based on one cation/anion pair and occasionally on a triplet with two cations and one anion type when the anion carries a double charge (dicationic ILs).

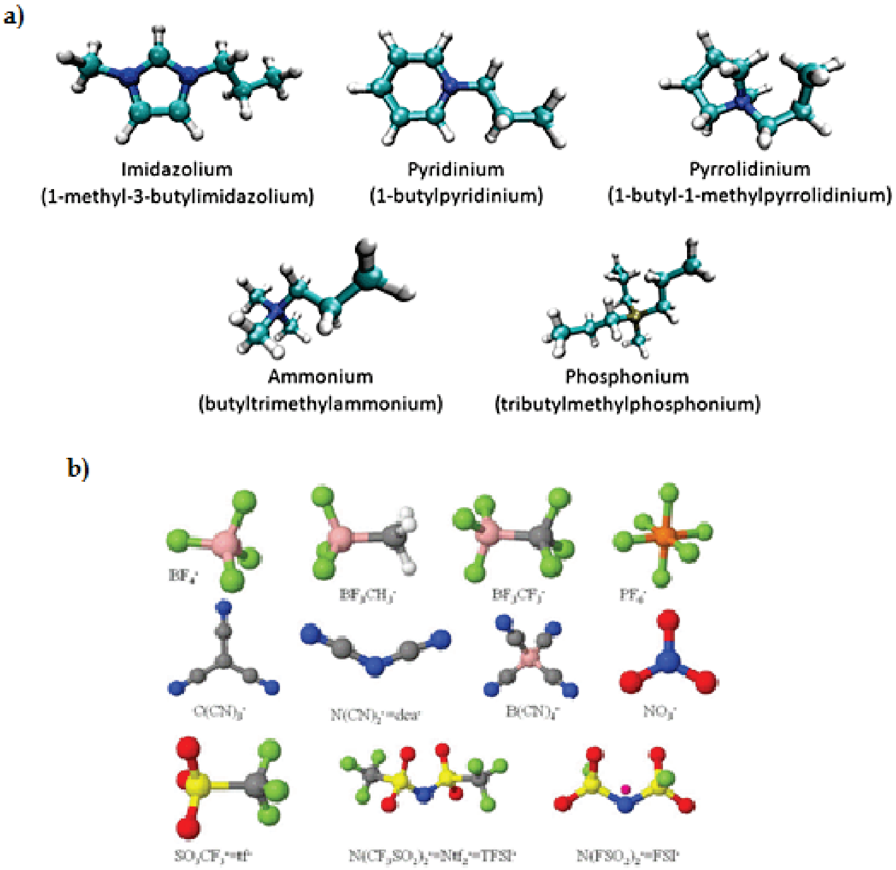

Figure I-9. The most common a) cation classes and b) anions

Ionic liquids were first suggested as lubricants in 1961 because of the high stability of their thermal properties that could prevent corrosion issues of lubricated systems [104]. But this is only one among the long list of the remarkable properties they exhibit as potential lubricants, which explains the increasing enthusiasm to study them [20,104–108]. Their low melting point, negligible volatility and non-flammability are all essential attributes to the use of these lubricants under severe operating conditions. Also related to ions properties, the high polarity of ILs can induce the formation of a strong absorbed film on charged surfaces that protects them from destructive solid/solid contacts. Finally, ILs are customizable lubricants as the cation/anion couple deeply influences the tribological properties of the ILs. Among the possible combinations, the chosen {cation, anion} couple will perform well in specific applications but fail in others. For that reason, numerous studies on ILs as lubricants have focused on the dependence of IL properties on their composition either in bulk rheology or at liquid/solid interfaces.

I.3.2 ILs in lubricated systems

Given their properties in the lubrication field, ILs are mostly studied for oil replacement. Some were compared to X-1P and PFPE, two lubricant oils commonly used in specific industrial lubricated systems [20]. At different conditions of temperature and pressure, ILs exhibit lower friction and wear than the two reference oils. But ILs were also considered as lubricants with alternative uses: either with additives or as additives, or in very specific environments as in high vacuum (for space applications) or in very thin film confinements (for applications in electronics).

Some ILs were tested with additives to enhance their lubricating performances [104]. When the surface and the additive were compatible (i.e. when they interact enough to create a protective tribofilm), friction and wear of IL-lubricated contacts were both found to be reduced. Best performances were reached with an amino-acid-derived salts specially designed to work with ILs.

Studies on the use of ILs as additives for classic oils [20] identified a friction reduced up to 30 %, explained by the formation of a protective tribolayer adsorbed on the shearing walls. The latter can prevent solid-solid contact and limit corrosion reactions at the interface, as it protects the substrate from the lubricant and the water it might contain. Nevertheless, the application is limited by the low solubility of common ILs in oils (< 1 %). Better performance might be obtained using specific ILs or base-lubricants. For example, ILs are more miscible in polyethylene glycol: very low wear rates were obtained for solutions of polyethylene glycol with 3 % of IL. It was also found that ILs are rather more efficient as additives at 100°C than at 25°C.

Under high vacuum, ILs also exhibit lower friction that the PFPE [20,107]. It is noteworthy that the alkyl chain length of IL's cation were found to have no influence on the friction in this configuration [109]. However cations with short alkyl chains exhibit better thermal stability than ILs with longer ones. This results in an increase of the lubricant lifetime [107]. Aside, their low vapor pressure and high radiation resistance features made ILs very good candidate for high vacuum space applications.

In MEMS/NEMS ILs could replace PFPE oils, which experience metal catalytic degradation, and their high electrical conductivity could contribute to improve the technologies in the field. Compared with classical lubricated systems, lubricant films in MEMS/NEMS are less than 40 nm thick but not submitted to high confining pressures [20]. In this configuration, it was found that substrates with hydroxyl terminations or silicon surfaces lead to more interactions and induce the formation of strong anti-wear films that ensure good tribological properties. Moreover, a mixture of several ILs can lead to better performances than a single IL. As ILs are electrically conductive, they can also find applications in electrical cars where electric potential differences are the cause of mechanical damages when insulated by non-conducting lubricant [110].

I.3.3 Ionic liquid lubrication mechanisms

This section presents a short review of the investigations, carried out over the past ten years, on ILs as lubricants. It covers the bulk rheology properties which depend on the nature of their ions, on the presence of a surface or a confinement. This section aims to apprehend the formation of boundary films and their dynamical behavior in the molecular lubrication regime, as much essential elements in the choice of an IL as a lubricant.

Inherent properties of ionic liquids in bulk rheology

Ionic liquids exhibit different rheological behavior depending on their composition, size and shape. First, the length of alkyl chains of ions (most often the one of cations), influences the nature of the fluid and its related properties. ILs with longer chains exhibit enhanced viscosity [19,20], higher piezo-viscosity coefficient and lower surface tension [48]. Their rheological properties are also less dependent on the shear rate [19]. In most applications they perform better than ILs with little chains, because their higher viscosity and piezo-viscosity index stimulate the formation of a thicker hydrodynamic film. Therefore, the wear volumes are drastically reduced [20,111]. As an example, the wear volume produced by a contact lubricated with $[C_{12}MIM][PF_6]$ IL (long alkyl chain) is ten times lower over the same sliding time than a similar contact lubricated with $[C_1MIM][PF_6]$ IL (short alkyl chain) [20]. Lastly, the melting point of ILs also varies with the alkyl chain length [20], and so deeply modifies the rheological response at low shear rates.

Likewise, the shape of ILs has an impact on their tribological response in severe environments. An asymmetric structure of the ions of an IL make it more resistant to solidification [112,113]. Perkin and coworkers [114] experimentally observed reduced wear and friction for systems lubricated with ILs made up of ions with important disparities in size and shape compared to more regular non polar fluids. On the other hand, a sub class of ILs named “ionic liquid crystals” solidify at close-to-ambient conditions of pressure and temperature, and exhibit specific rheological behaviors. Besides their important viscosity (around 1 Pa.s), the specific orientation of their molecules (as they tend to crystalize) make them very non-Newtonian fluids.

With regard to the ion natures, the disparity of anions is more important than the one of cations but both have a significant influence on the ILs physical and chemical properties. Three families of cations with equivalent alkyl chain length and the same anion were compared: from the less to the more viscous, the ILs based on imidazolium, pyridinium, pyrrolidinium are among the most studied ones in the last decade [20]. As a confirmation, Lopéz Sánchez and coworkers [115] observed higher friction with the $[BMpyrr][NTf_2]$ than with the $[BMMIm][NTf_2]$. As for the anions, eight families were compared based on ILs with the same cation: from the less to the more viscous: NTf_2^- (≈ 10 mPa.s) < FAP^- < $BETI^-$ < $CF_3SO_3^-$ < $BF4^-$ < $PF6^-$ (≈ 10-100 mPa.s) < Cl^- < Br^- [48,114]. In particular, it has been noticed that the geometry of anions influences the viscosity: the more spherical and symmetric anions, the more viscous ILs [48].

To ensure the presence of a lubricating film in EHD regime and so to guarantee the best lubrication performances in severe environments, the viscosity of the candidate IL must combine a large response to the confining pressure (i.e. an adequate PVC) and good thermal stability [48]. The PVC were compared for some of the previous anions: $BF4^- < NTf2^- < PF6^- < FAP^-$ [48,116]. As for the temperature , a low temperature-viscosity coefficient β as defined by Spikes [117] implies little dependence of the viscosity on temperature. NTf_2-based ILs have shown the lowest temperature-viscosity coefficient ensuing a good thermal stability. Finally, NTf_2-based ILs present the highest PVC/β index ratio and so they can be considered as the best candidates for severe environments. Considering mild lubrication conditions, PF_6^--based ILs present the lowest coefficients of friction and wear generation, although the ones from NTF_2^--based and BF_4^--based ILs are low too [19].

Interfacial behavior

Once in contact with a surface, the IL adopts a layered structure close to the interface that can differ from the structuration of a non-polar fluid. In fact, as detailed below, the conformation changes with the IL nature, the surface topography and charges and it can directly impact the rheology of the nano-contact.

First, on a single surface, the deposed IL experiences different structurations according to the size of the ions and the surface charges. On uncharged surfaces considered in the literature (gold, graphite or mica with a carbon precoverage), the global density profile of the IL (anions and cations taken together) is similar to the one with non-polar surfaces (layering of the size of the ions) [118]. This denotes alike solvation forces in both cases. Wetting is high at the liquid/solid interface, which favors the formation of protective layers [27,119]. Also, when anions and cations are of comparable size, they structure in a checkerboard-like arrangement in order to optimize charge neutrality. Moreover, the cation lies flat on the surface while, on the contrary, the anions stand normal to the wall [27] with their oxygen elements adsorbed onto the surface [28]. On negatively charged surfaces (mica), the cations remain alone in the first layer next to the wall to screen the charge, and anions come above them as a second layer. In this configuration, the wetting might be weaker or stronger depending on the ions nature [119–121]. It is finally observed that whatever the surface charge, ions with longer alkyl chains disturb the first layer ordering [27,120]. This can modify the interface rheology once the fluid is sheared.

The IL structuration near the interface is of the same nature when confined between two surfaces than previously with a single surface. Between uncharged surfaces (graphite or iron), successive mixed-layers of cations and anions are formed parallel to each surface [28]. The cations are oriented parallel to the wall, which favors the layering in presence of small anions [22]. Between charged surfaces, successive monolayers of cations and anions come one after another [21] and the layering increases with the charge intensity [22]. The dependence of the structuration on the alkyl chain length is still effective for an IL confined between uncharged surface [22], but it is remarkably amplified when confined between charged walls

[21,22,122]: for a [CnC1Im][NTf2] IL, Perkin's team [21] observed that between an imidazolium cation with a butyl alkyl chain (n=4) and an imidazolium with an hexyl alkyl chain (n=6), the layer thickness increases up to four times. This is explained by the more amphiphilic nature of the [C_6C_1Im] cation which causes self-assembly into tail-to-tail cation bilayers at the mica surface (Figure I-10-b,c), driven by the need to sequester the non-polar hydrocarbon chains away from the saturated ionic regions. The interactions between the cation tails being a lot weaker than the interaction at the interface, this dual layered structure (one adsorbed IL layer locked on the surface and a mobile one) leads to very good tribological properties [113]. A similar bilayer structuration is observed with pyrrolidinium-based ILs, but the mono layers to bilayers transition occurs at different alkyl chain length than with imidazolium-based ILs and the alkyl chains are also more interdigitated [123].

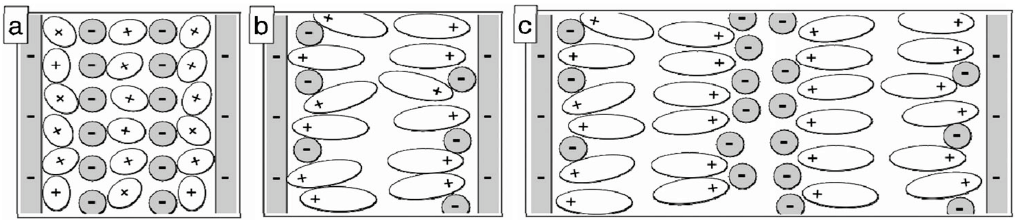

Figure I-10. Suggested ion orientations in (a) [C4C1im][NTf$_2$] at a film thickness of 2.3 nm showing alternating cation and anion monolayers for C(AC)$_2$; (b) [C6C1im][NTf$_2$] at 3.4 nm showing a single bilayer, (ACCA)$_1$, and (c) [C6C1im][NTf$_2$] at a film thickness of 8.3 nm showing two bilayers, (ACCA)$_2$ [21].

In addition to the described fluid structuration, the liquid/solid interaction directly influences the strength of the adhesion of the fluid onto a surface. In particular, the chemical elements involved are predominant in the formation of a protective tribofilm. For example, phosphate-containing anions *mimic* the behavior at the interface of anti-wear additives like ZDDP and act as a protective tribofilm [113]. Lubrication performances are also enhanced with fluorine-containing anions [113] or phosphonium cations [124,125], which favor tribofilm formation. Likewise, dicationic ILs show better anti-wear properties than mono-cations as the adsorption film were found to be thicker [126,127]. Concerning surfaces, it was also observed that SiO_2 and $Mg(OH)_2$ materials shows better tribological properties than Al_2O_3, MgO, ZnO and ZrO_2 because of the active interaction with the IL hydroxyl groups, which initiates protective layer formation [20]. At last, the presence of water significantly impacts the lubricating behavior. With hydrophilic ILs, water is absorbed in the lubricant and reduces its viscosity: it will be thus more easily squeezed out of the contact and boundary lubrication might occur. With hydrophobic anions, the water is adsorbed on the surfaces and modify the ions orientation. This can either increase or decrease friction, depending upon the ions type and the operating conditions [128,129].

Dynamics at the nanoscale

The global dynamic response of a nanoscale contact and the rheology at the interface both depend on the previously depicted structuration and tribofilm formation, and on some conditions like pressure or shear rate.

The influence of the structuration is complex. A difference is to be made between the layering structuration and the cohesive reinforcement of the fluid. Indeed, the first one tends to ease the diffusion as a motion is possible between well-defined layers whereas the second reduces the mobility as an isotropic densification occurs. Confining two different ILs between low-charged silica surfaces, Federici Canova and coworkers [130] observed two opposite types of structuration resulting in two rheological responses: alternating monolayers (of cations and anions) formed with the [BMIM][BF4] induce faster dynamics than the mixed layers formed with the [BMIM][NTF2]. Similarly, as previously noticed, molecules with long alkyl chains progressively order in parallel layers as the shearing rises. In this way, they present a non-Newtonian behavior at low shear rate in nanoconfinements [128,131] as parallel layering reduces the resistance to shearing with increasing sliding. On the contrary, the cohesive nature of the fluid dictates its viscosity and different external factors can alter it and so modify its dynamical response. For instance, Bou-Malham and coworkers [23] found that the surface charge increases the ILs cohesion. Indeed, the bulk viscosity exponentially increases from film thickness thinner than 20 nm when confined between mica surfaces. The IL even exhibits a solid-like behavior under 3.5 nm. Concurrently, if the same fluid is confined between methyl-terminated surfaces, no viscosity variation of the IL occurs for thicknesses down to 2 nm. In a different context, Mendonça and coworkers highlighted that nano-roughness at the solid surface could disturb the fluid cohesion and favor the shearing movement [131].

When high pressure conditions force the lubricant to nanoconfinements, a stick-slip response can occur [112]. In this regime, friction is usually independent of the shear rate. Although the stick-slip also takes place with non-polar fluids, its origin and apparition conditions differ with ILs as they are generally less subject to solidification. Several explanations were suggested [112,129]. The shearing might happen at the interfaces between the anion and cation monolayers when the IL is confined between charged surfaces. Besides, it was observed that the motion can oscillate between local microslips and collective slip resulting from consecutives jumps of the molecules at a fixed shear plane. Finally, a succession of local freezing and melting could occur to accommodate the shearing. Depending on the rheology, it has been observed in some configurations that friction can even drop with an increasing shear rate [128]. This anomalous response is attributed to bonds breaking with the shearing as the sliding times between the molecules become faster than the re-bonding times at important shear rates.

I.3.4 Problems inherent to ILs and solutions

Since ILs are considered for a use as lubricants, research groups also investigated the potential issues.

In particular, due to their high polarity, the water absorbing capacity of ILs is higher than for classical lubricants and the tribo-reactions at the fluid/solid interface with metallic surfaces can be more important [20]. Under confinement, this reaction provides a benefic anti-wear film but for highly reactive components, degradation of the surfaces can arise. Thus damaged surfaces rapidly lead to the global system failure. As an example, fluorine-containing anions were found to be very sensitive to tribo-corrosion [20,115]. Nevertheless this degradation can be restricted in several manners. First, the choice of an appropriate ILs can significantly reduce corrosion in major situations. As the charge of the ions is not located in their alkyl-group, the ones with long alkyl chains present a reduced polarity and are consequently less prone to corrosion [19,20]. Moreover, specific anions were also found to be quite resistant to chemical degradations as for instance $[NTf_2]^-$ which is one of the most hydrophobic anions [20]. Best performances in resistance to corrosion were achieved with the synthetic anion $[FAP]^-$ which offers much better tribological properties (low friction and wear) than $[NTf_2]^-$-containing ILs in long-lasting tests [20]. Other solutions consist to add anticorrosion additives to the lubricating IL or to mix it with an anticorrosion functional group [20]. Tests with a benzotriazole additive showed good performances, but the latter consumed quickly and did not resist to high temperature. On the other hand, mixing a triazole at 50/50 with an IL efficiently absorbs the acid locally generated by hydrolysis and chemisorbs on metallic surfaces to form a protective tribofilm. Lubricating performances are therefore greatly enhanced.

Further to corrosion, oxidation reactions are also to be considered using ILs as lubricants. In fact, even if they are less prone to oxidation than classical oils, they can still deteriorate over long periods [20] in severe environments. As for corrosion, the presence of water must be restrained and the use of hydrophilic anions (as PF6 and BF4) should be avoided to increase the thermo-oxidative stability and keep good tribological performances [104]. Not much investigations were conducted on the subject except on the cation influence: the –H terminations are suspected to favor the oxidation so cations with short alkyl chain lengths present better thermo-oxidative stability [20,104].

Finally, though ILs are considered as green lubricants owing to their non-fossil origin, their high reactivity might also be toxic for the environment, which could become a major issue if they are used more widely. In particular, ILs with long lipophilic alkyl chains tend to increase their hazardous properties [24]. According to a recent review of Amde *et al.* [132], the IL toxicity varies considerably across their type, test conditions and morphology of the organisms. On the whole, it is recommended for further studies to create a database of environmentally benign ILs, based on their toxicological and biodegradation data to fully inform on noxiousness for the environment.

I.3.5 Conclusion

As a conclusion, ILs can feature best lubrication performances than classical oils and their particular properties such as electrical conductance or high thermal conductivity can also be of interest for some specific applications. Today, they remain expensive lubricants with rather high sensibility to corrosion and oxidation and possible harmfulness for the environment. However, further investigations would give the keys to choose one IL for a specific application, optimizing the lubrication performance and limiting the adverse reactions.

Ahead of those investigations, the approach in this work will mostly consider the rheological response under representative conditions of an EHD contact, the behavior at high confinements and the dynamic interactions in presence of various rough and smooth particular substrates. An IL with rheological properties alike to the ones of classic lubricant oils should be selected, so the revealed lubrication mechanisms could be compared. It should also be composed of ions which are already recognized to be compatible with solid materials of current lubricated systems.

After the review on the macroscale and nanoscale properties of ILs, some questions remain. Even if the rheological properties of various ILs were already explored, a detailed study of their response to high shearing is still missing. In the following, the behavior of an IL will be studied in diverse configurations representative of thin film or very thin film regimes. Among other considerations, the revealed mechanisms must feed the discussions on the friction response to shearing with polar surfaces. Finally, from the orientation and structuration of the ions at the interface, hypothesis can be drawn up on the influence on the reactivity at the interface and on the rheological response.

To carry out the aforementioned investigations, the choice was made to use a numerical tool able to simulate the dynamics at the nanoscale. Compared to experimental studies, this approach enables to easily test a large number of cases and to precisely configure the thermodynamic inputs of pressure, temperature and shear. Once validated, it is also capable to quantitatively estimate some physical quantities of interest. Moreover, as the main objective was to understand the mechanisms involved in the lubrication process, the numerical tool offers the opportunity to have a direct look into the local phenomena and to characterize them over various input conditions. The next chapter details the tool and its parameterization.

Chapter II: The Molecular Dynamics tool

This study aims to predict the behavior of ionic liquid lubricated systems under various operating conditions and to investigate nanoconfinements to understand the lubrication mechanisms occurring in severe environment. The molecular dynamics numerical tool enables to easily explore multiple configurations with a great control of the environment parameters and offer the possibility to focus independently on each involved mechanisms.

In this chapter, the molecular dynamics tool is first presented and the different solving methods are reviewed and evaluated for their suitability with this study. Then a first simulated system is introduced: bulk simulation of an ionic liquid. With this system, the rheological response of this fluid to various conditions (pressure, temperature, shear rate) can be analyzed. At last, a second system is presented: the same fluid nano-confined between surfaces of different nature. Through this configuration, a deep analysis of systems response to high shearing is possible.

II.1 Model theory

This first section presents the molecular dynamics tool through its operational principle and the existing methods to configure a simulation.

II.1.1 Context

Molecular Dynamics (MD) is an N-body numerical simulation method able to describe the physics of interacting particles as atoms and molecules thanks to long-range interaction laws [66]. It was first developed in the late 1950s for applications in the theoretical physics. Today, it can model various configurations in any phase state from simple crystalline solid structures to complex proteins. Hence, it finds applications in material, biomolecular and chemical physics sciences.

In the tribological field, numerous studies highlighted the ability of MD simulations to describe the lubricant dynamics in lubricated systems [15,17,133,134]. Fluids of different natures can either be tested as bulk fluid to evaluate their inherent properties in various environmental conditions, or in nanoconfinements. In the last case, each fluid presents specific structuration and orientation at the liquid/solid interface that have direct effects on the global rheology and the potential chemical reactions. The dynamics of the sheared contact can also be modeled to evaluate the characteristic values of lubrication at the molecular scale.

As any approach, MD comprises limitations. First, as time is explicitly solved in the method, the simulation time step must be low enough to introduce minimum cumulative errors in the resolution. This confines the simulation times to generally a few nanoseconds. Similarly, with today computational technologies, the number of particles can go up to a few thousands and so the size of the 3D simulation domain reaches generally of a few nanometers cube. It is sufficient to evaluate inherent properties of bulk fluid, as long as lubricant molecules are not too big. Though it is more constraining for nanoconfined systems as only a nano-patch of the contact area can be considered. Besides, classical MD cannot describe potential chemical reactions as more complex modeling at the subatomic scale are necessary to determine the establishment conditions of chemical bonds. Nevertheless, some hybrid algorithms described thereafter enable to model some simple unbonding and rebonding between particles. Finally, MD remains a relevant tool to provide essential information on the transport properties at the molecular scale, cornerstone of the global tribological response of a lubricated contact.

The time scale restriction is besides a challenging obstacle to simulate the shearing of complex fluids. As only a few nanoseconds of a nanoscale system can be simulated, the shear rate is generally of the order of 10^7 to 10^{10} s^{-1} to acquire sufficient data statistics. Consequently, with confinements of a few nanometers, it is hard to run shearing simulations with surface velocities under 1 m/s. Moreover, the simulation of complex fluids come with complex modeling of the interactions between elements, bringing an increase of the computation times. As the trend is to study molecular lubrication with new fluids (IL, glycerol, refrigerants, fatty acids…) [101–103] compromises must be found between the model complexity, the simulating times and the shearing velocity.

II.1.2 Force Field Theory

The main feature to model properly the material behavior in MD simulations is the definition of the atomic interactions (as chemical bonds, weak interactions, hydrogen bonds or Coulombic interactions). A force field (FF) refers to the functional form and parameter sets used to calculate the potential energy resulting from those interactions.

In classic FF, the functional form is split up between non-bonded $E_{non-bonded}$ and bonded E_{bonded} terms of the total potential energy E of a particle. The first often characterizes all the long-range contributions (Van der Waals, electron cloud repulsion and electrostatic forces) while the second describes the chemical bonds. The non-bonded terms are softer than the bonded ones but are usually the most computationally intensive. Hence, it is relevant to set up different time steps to compute both kinds of potential. Alternatively to classic ones, reactive FFs aim to represent both bonded and long-range interactions in a same expression by progressively changing the potential nature according to the distance between the atoms. Those FFs reasonably increase the computational times and allow a simplified representation of chemical reactions. Though, to accurately predict complex chemical reactions, ab initio computations or methods combining MD and quantum chemistry (as ab initio MD) are necessary [135]. However, associated simulation times are several orders of magnitude larger than in classic MD.

According to the size of the simulated molecules and to the targeted simulation times, the representation of the molecule structures may differ with the FF. In "All-atom" FFs every type of atom is individually implemented in the simulation, while "united-atom" FFs treat the hydrogen and carbon atoms in each terminal methyl and each methylene bridge as a single interaction center. "Coarse-grained" potentials define even more crude representations for increased computational efficiency. They are frequently used in long-time simulations of macromolecules such as proteins, nucleic acids, and multi-component complexes.

The configuration of the FF parameter sets is the most sensitive aspect of the MD method. They directly influence the properties of the modeled matter and its reaction with other materials. Only accurate sets would be able to provide quantitative results. They are ascertained either from experimental data to verify some physical properties (empirical force fields) or from ab-initio calculations. Independently of the method, they are always determined on a limited range of environmental conditions (of pressure, temperature, physical state…) and so the validity must be verified before use in situations differing from the establishment conditions of the FF.

II.1.3 Calculation principle and Equations

To model the physics of the simulated system, MD simulations explicitly solve the Newton's equation of motion over time. The positions and the velocities of each atom are recalculated every given time step according to the interaction forces between atoms and the thermodynamic constraints simulating the operating conditions. To do so, the potential energy E of each atom is deduced from their interatomic interactions which are defined by the setup of a force field detailed in following sections (ionic liquid: II.2.2 and surfaces: II.3.1). The conservative force F_c acting on one atom is then the opposite of the gradient of its potential energy E:

$$F_c = -\nabla E \tag{II. 1}$$

The Verlet algorithm is usually employed to compute the atom position as it guarantees a good precision of the energy conservation [66]. However, considering the disparity between the characteristic times of the different interatomic interactions ruling the dynamics of complex fluids, the use of a multi-timescale integrator can substantially reduce the computation times [136]. The reversing Reference System Propagator Algorithm (r RESPA) allows to consider separately the short and long range interactions to integrate the Newton's second law of motion over time. Therefore, the displacements of particles resulting from sensitive intra-molecular interactions are computed more often than the ones resulting from loose inter-molecular interactions. Besides, before the integration of the interaction forces, additional forces are added to the long range forces to represent the external conditions of pressure, temperature and potential other imposed forces. The different thermostats and barostats used in this study are detailed in the following for each simulated configuration. The r RESPA integration algorithm is detailed in Appendix A.

The process is repeated many times to reproduce the dynamical behavior of the simulated system until an equilibrium or steady state is reached and/or sufficient statistics is acquired to estimate the wanted physical quantities. Through iterative computations of positions and velocities, cumulative errors are also introduced, depending on the chosen time steps. The swifter displacement of atoms correspond to their thermal agitation and start to be appreciated at roughly 10^{-12} s. To ensure energy conservation in the thermodynamic ensemble, time steps closed to the femtosecond (10^{-15} s) are generally taken. With such time basis, millions of time steps are necessary to achieve the few nanoseconds needed to analyze the physics of the simulated system. Tens of CPU units are commonly exploited to complete the simulations in reasonable times.

II.2 Bulk simulations

II.2.1 Choice of the studied IL

It was observed that hydrophobic anions like the bis(trifluoromethylsulfonyl)imide [NTf_2^-] (sometimes also referred to as [tf_2N^-] or TFSA) perform well in steel-steel contacts [20]. As previously depicted, ILs with this anion also exhibit pressure-viscosity coefficients and temperature-viscosity coefficient that confer them an optimum stability under high pressure and wide-temperature range conditions [48,116]. With respect to the cation, imidazolium-based RTILs proved to be thermally stable and adaptable. Indeed, through different chemical reactions, alkyl chains of varying lengths can be positioned on the imidazole ring, modulating its physical and chemical characteristics [104].

Finally, coupling a bis(trifluoromethylsulfonyl)imide [NTf_2^-] anion with a short alkyl chain length imidazolium as the 1-3 dimethylimidazolium [$mmIm^+$] (also referred to as [$C_1C_1Im^+$]) results in an ionic liquid (illustrated in Figure II-1) with one of the lowest possible viscosity, and comparable to the one of common lubricants [20,48]. This feature can induce low friction in tribological systems working in the full film lubrication regime, but also cause more lubricant squeezing out of the contact, which would highly favors the presence of the nano-confined areas that are central in this work. At last, the size of [$mmIm^+$] cations is very close to the one of [NTf_2^-] anions, meaning the results of this study are exempt from possible asymmetrical effects.

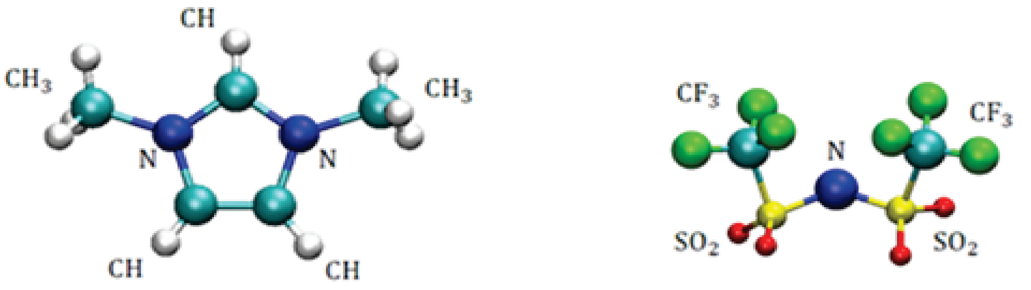

1,3-dimethylimidazolium [$mmIm^+$] bis(trifluoromethylsulfonyl)imide [NTf_2^-]

Figure II-1: Simulated Ionic Liquid: cation (left) and anion (right) molecules

II.2.2 IL force-field development

To model the behavior of ILs with MD simulations, Canongia Lopes and Pádua [25,26] built an all-atom force field from ab initio calculations. The molecular geometry, the partial charge distribution and the torsional energy profiles were considered to evaluate the parameter set. It was then validated on several ILs in both liquid and crystalline phases. Some partial charges of the anions were also adjusted to be transferable to various sets of molecules and compatible with the OPLS force field [137].

To represent the Van Der Waals and Coulombic interactions between atoms of different molecules or separated by more than 4 atoms along the same molecular chain, the functional form of the non-bonded potential energy bring together a classic 12-6 Lennard-Jones potential [138] and the Coulomb's law:

$$\boldsymbol{E_{non-bonded}} = \sum 4\varepsilon_{ij}\left(\left(\frac{\sigma_{ij}}{r_{ij}}\right)^{12} - \left(\frac{\sigma_{ij}}{r_{ij}}\right)^{6}\right) + \frac{1}{4\pi\varepsilon_0}\frac{q_i q_j}{r_{ij}} \tag{II.7}$$

with, for the Lennard-Jones term, r_{ij} the distance between the atoms' nuclei, σ_{ij} the finite distance at which the inter-particle potential is zero and ε_{ij} the depth of the potential well, and for the Coulombic term, q_i the atomic partial charge of the atom i and ε_0 the electric permittivity constant equal to 8.854 × 10^{-12} F/m. When the atoms are of different natures, the Lorentz-Berthelot mixing rules are applied to determine the Lennard-Jones parameters:

$$\varepsilon_{ij} = \sqrt{\varepsilon_i \cdot \varepsilon_j} \quad \text{and} \quad \sigma_{ij} = \frac{\sigma_i + \sigma_j}{2} \tag{II.8}$$

The cutoff distance of the non-bonded interactions is fixed to 12 Å as they are almost null over this distance. However, as the coulombic forces have a very long interaction range, they remain effective for $r_{ij} > 12$ Å but are estimated using a particle-particle particle-mesh solver [139] (see Appendix B for more details).

To describe the complex structure of fluid molecules, their numerous degrees of freedom and the bond flexibility, the bonded term of the interaction potential energy is the combination of three components:

$$\boldsymbol{E_{bonded}} = \boldsymbol{E_{bond}} + \boldsymbol{E_{angle}} + \boldsymbol{E_{dihedral}} \tag{II.9}$$

Atoms pairs linked with covalent bonds are model as tension/extension springs:

$$\boldsymbol{E_{bond}} = \sum_{bonds} K_b\left(r_{ij} - r_0\right) \tag{II.10}$$

with K_b the bond stiffness, r_{ij} the distance between atoms i and j and r_0 the equilibrium distance. Force between triplets of atoms are represented by an angle bending potential:

$$\boldsymbol{E_{angle}} = \sum_{angles} K_a\left(\theta_{ijk} - \theta_0\right) \tag{II.11}$$

with K_a the angle stiffness, θ_{ijk} the bending angle and θ_0 the equilibrium angle. Finally, torsion of covalent bonds between quadruplets of atoms are modeled with a dihedral potential:

$$\boldsymbol{E_{dihedral}} = \sum_{dihedrals} \frac{1}{2}K_{d,1}\left[1 + \cos\left(\phi_{ijkl}\right)\right] + \frac{1}{2}K_{d,2}\left[1 - \cos\left(2\phi_{ijkl}\right)\right] + \frac{1}{2}K_{d,3}\left[1 + \cos\left(3\phi_{ijkl}\right)\right] \tag{II.12}$$

with $K_{d,i}$ the torsion stiffness of the different modes and ϕ_{ijkl} the torsion angle.

The force field is compatible with the classic OPLS-AA and is able to describe a large set of IL compounds, but it generally fails to reproduce quantitatively their transport properties. In particular, it typically overestimates their viscosity by one order of magnitude [140]. A rescaling of some of the force field coefficients is then necessary to obtain accurate predictions of the IL lubrication behavior by means of this force field. This is presented in the following section II.2.5

II.2.3 System definition

One goal of the following work is to estimate the bulk properties of the studied fluid. The first goal is to validate its model parametrization by comparing computed thermodynamic features with the corresponding experimental data. Secondly, the rheological behavior can be characterized in a variable environment (pressure, temperature and shear rate).

Each simulation run is associated to a statistical ensemble. In the microcanonical ensemble (NVE), the total energy of the system (sum of the potential and kinematic energy of all the atoms), the volume and the number of particles are each fixed to their starting values. In most of the studied cases, the fluid is submitted to no external forces so Equilibrium Molecular Dynamics (EMD) simulations were run with a microcanonical ensemble as no control of the pressure and temperature is necessary. Assuming that the bulk fluid is an ergodic system, its macroscopic thermodynamic properties can be determined through the evolution of a simple MD simulation as the time averages of an ergodic system correspond to microcanonical ensemble averages. Hence, the different macroscopic quantities of density, viscosity and diffusion are evaluated with this method. Some Non-Equilibrium Molecular Dynamics (NEMD) simulations were also carried out to study the influence of the shearing on the viscosity. Although the equilibrium state is broken, a steady state is required to average over time the studied quantities.

In bulk simulations, periodic conditions are applied along the three directions to simulate an infinite fluid medium. Hence, the dimensions of the simulations domain must have theoretically no influence on the occurring physics. Minimum dimension sizes are nevertheless required for the molecules not to interact with themselves through the periodic boundary conditions and to have enough molecules to ensure sufficient data statistic generation when computing the thermodynamic quantities. So most simulated bulk domains are cubes with edges 5 nanometers long, that being roughly ten times the size of [mmIm$^+$][NTf2$^-$] molecules (Figure II-2).

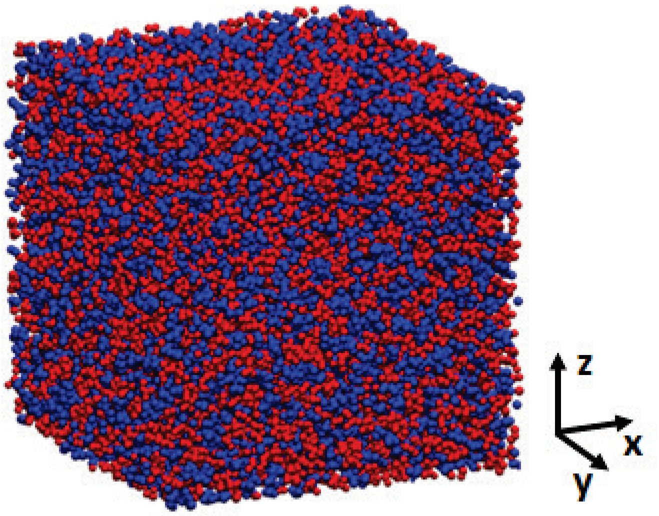

Figure II-2: Bulk fluid domain. Red molecules are anions and blue ones are cations

Before the computation of the desired data, an equilibration step is run to minimize the potential energies of the molecules placed manually into the simulation box and to reach an equilibrium or steady state according to the imposed temperature, pressure and shear rate. In particular, although MD simulations are deterministic, the equilibration step allows for a simulation of a disordered initial state peculiar to a fluid at the liquid state. Those initialization stages are run in an isothermal-isobaric (*NPT*) ensemble in which the atom number, the temperature and the pressure are controlled but where the total energy is free to evolve to adapt to the environmental conditions. To lead the simulation to the desired pressure and temperature, Nosé-Hoover thermostat and barostat [141,142] were set up and regulated the full system every 100 and 1000 time steps respectively. As the studied fluid presents a relatively low mobility, preliminary tests revealed that a few hundreds of picoseconds are often necessary to fully stabilize the system before calculation of the quantities of interest. Once at equilibrium, the statistical ensemble is switched to microcanonical.

II.2.4 Quantities of interest

Several thermodynamic properties of the fluid were computed to evaluate its rheological behavior at conditions of shearing, temperature and pressure which cannot be achieved easily through experimental tests.

Density

Density was the first bulk fluid property investigated as it is a representative quantity of the fluid thermodynamic nature depending both on the pressure and the temperature. It is also relatively fast to compute so a wide range of environmental conditions could be tested. The density ρ can be defined as follow:

$$\rho = \frac{\langle \sum_{i=1}^{n_{mol}} m_{mol,i} \rangle}{V} \tag{II.13}$$

with n_{mol} the number of molecules in the system, $m_{mol,i}$ the mass of one molecule, V the domain volume and $\langle\ \rangle$ the average over time. As it is dependent on the volume, the density computation must be perform in an isothermal-isobaric (*NPT*) ensemble in which the volume is free to vary. After the density reached its equilibrium value, it is time-averaged over 100 ps to get a satisfactory estimation of the value.

Diffusion

The diffusion coefficient D is computed from the mean square displacement of the molecules [66]:

$$D = \frac{1}{6n_{mol}t} \langle \sum_{i=0}^{i=n_{mol}} |\boldsymbol{x}_i(t) - \boldsymbol{x}_i(0)|^2 \rangle \tag{II.14}$$

with t the acquisition time and $\boldsymbol{x}_i$ the position of the molecule i. After the equilibrium stage in the NPT ensemble to relax the fluid at the desired temperature and pressure, 2 ns are necessary for the diffusion to stabilize at its limit value. The diffusion coefficients of different molecules of a same fluid can be computed either together or separately to provide information either on the fluid properties or on its component species.

Viscosity

The bulk viscosity was computed using two different methods. The Newtonian viscosity of the fluid is estimated through EMD simulations while NEMD ones were run to study the transition of the fluid from its Newtonian behavior (viscosity independent of the shear rate) to a non-Newtonian one. For the equilibrium simulations, the Newtonian viscosity is estimated within the linear response theory, using a Green-Kubo relation based on the integration of the autocorrelation of the five independent components of the traceless stress tensor [143]:

$$\eta_N = \frac{V}{5k_BT}\int_0^\infty \langle P_{\alpha\beta}(t)P_{\alpha\beta}(t=0)\rangle dt \qquad \text{(II.15)}$$

with η_N the Newtonian viscosity, k_B the Boltzmann's constant, T the fluid temperature and $P_{\alpha\beta}$ the independent components of the traceless stress tensor: P_{xy}, P_{yz}, P_{zx}, $\frac{1}{2}(P_{xx}-P_{yy})$, $\frac{1}{2}(P_{yy}-P_{zz})$. The computation time is directly dependent on the viscosity and averaging the contributions of those five components significantly reduce this time. Nevertheless, as it was studied on a wide range of environmental conditions, at the highest pressures and lowest temperatures (i.e. most important viscosities), more than 40 ns simulations were required to estimate the Newtonian viscosity with the chosen IL.

The evaluation of the sheared viscosity without shearing walls and without supplying external energy to the system is possible thanks to the Müller-Plathe algorithm [144]. The method consist of exchanging artificially momenta between particles of different regions to generate a shear velocity profile in the fluid (see Figure II-3). Hence, the shear rate $\dot{\gamma}$ is not directly an input of the simulation but is controlled by the number of particles swapping their momenta and on the periodicity of those swaps. To reach shear rates from 10^7 s^{-1} to 10^{11} s^{-1}, momenta exchanges goes from 1 exchange every 0.1 ps to 20 exchanges every 0.02 ps. The velocity range on which the data are exploitable is bounded at both sides: at the lowest shear rates, longer computations times are needed to yield the shear rate value through thermal noise and at the highest shear rates, a swap too frequent of the momenta prevent the establishment of a linear velocity profile. The viscosity η is then deduced from the shear stress τ measured from the energy of exchanged momenta p:

$$\eta = \frac{\tau}{\dot{\gamma}} \quad \text{with} \quad \tau = \frac{1}{2S}\frac{\delta p}{\delta t} \qquad \text{(II.16)}$$

with S the area of the section perpendicular to the direction of the exchanged momenta. As energy is added to the simulation, the control of the thermostat is also essential as it pulls out the excess of energy so the total energy of the bulk system is constant. In the present simulations using the Müller-Plathe method, the temperature was confirmed to be constant over time on account of the Nose-Hoover thermostat.

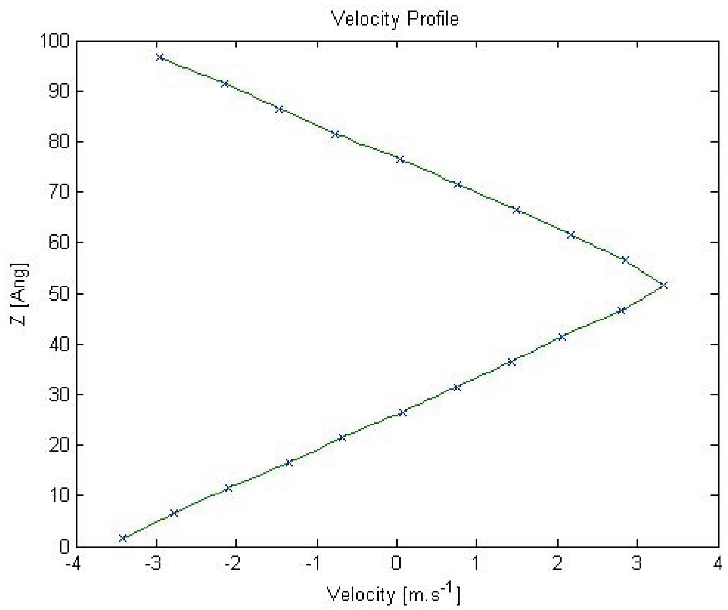

Figure II-3. Typical velocity profile resulting from the application of the Muller-Plathe method. The simulation is periodic in the *z* direction so the profile must be continuous between the lowest and the highest points.

II.2.5 Charge scaling and model validation

As quantitative results were expected from the present study, a standard charge scaling procedure [140,145] was implemented in order to properly reproduce the evolution of the density and of transport properties of the [mmIm+][NTf2-] ionic liquid with the temperature. This modification was conducted following the method described by Chaban [146].

For this purpose, the [mmIm$^+$][NTf2$^-$] IL properties were computed from MD simulations and compared to experimental data. Figure II-4 illustrates the variation of the IL density with temperature at ambient pressure P = 0.1 MPa, for both experimental data [146,147] and MD simulations carried out with 3 different charges weighting factors: w_c = 0.70, 0.75 and 0.80. The relative deviation between the computed density values and the measured ones is less than 1 % over the studied temperature range when w_c = 0.75. It was thus considered, for this specific w_c value, that density and by extension the structural properties of the [mmIm+][NTf2-] ionic liquid were satisfactorily predicted.

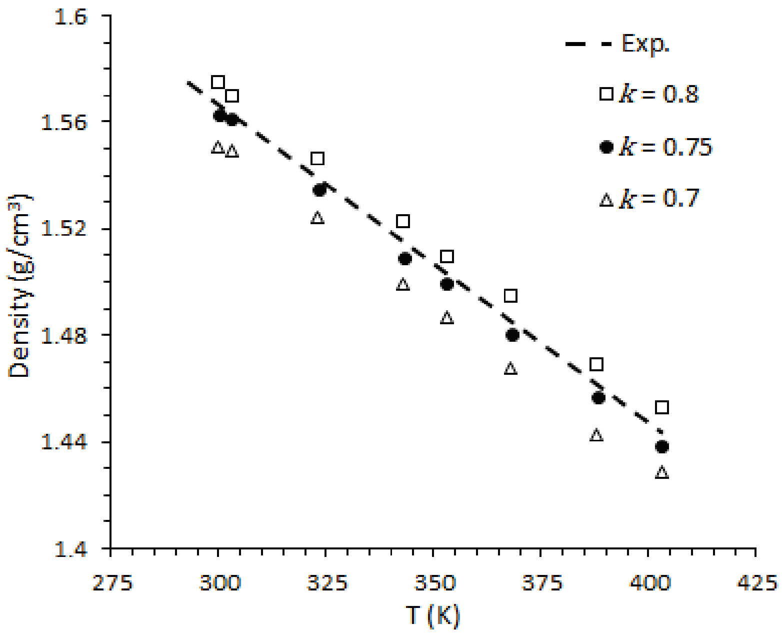

Figure II-4. Evolution of the bulk ionic liquid density with temperature, at ambient pressure p = 0.1 MPa. Symbols represent numerical values obtained for different weighting factors k applied to the Coulombic charges in the force field parameterization. The dashed line represents experimental results [146,147]**.**

As for dynamic properties, the diffusion coefficient was computed from the integration of the mean square displacement of the ions over time [66]. The weighting factor of 0.75 was used and the results were compared with analytical predictions of empirical laws derived from experimental data [148]. Figure II-5 shows the variation of the bulk self-diffusion coefficient *D* of [mmIm$^+$] cations and [NTf$_2$$^-$] anions versus temperature, at ambient pressure P = 0.1 MPa. The agreement between the two set of results is fairly satisfying: the maximum relative deviations are of ca. 20 % for the cation and ca. 10 % for the anion at 333 and 393 K, respectively.

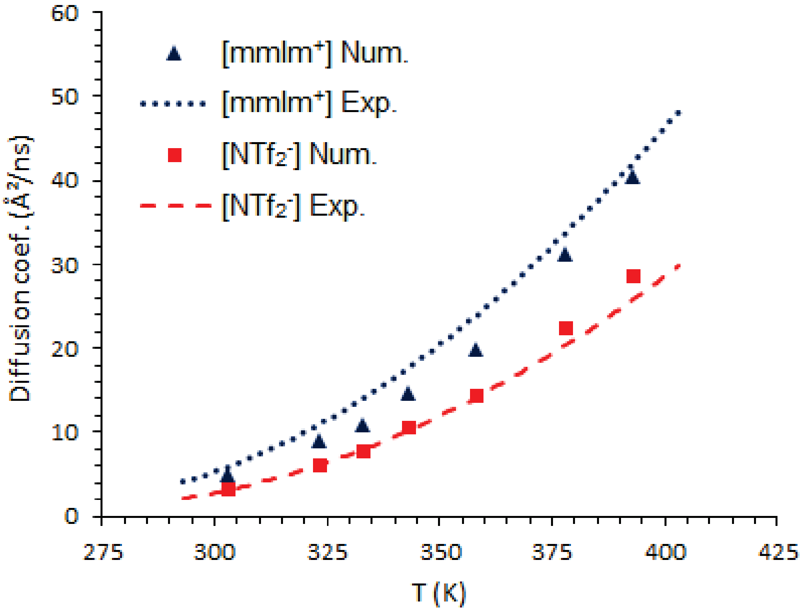

Figure II-5. Bulk diffusion coefficients of [mmIm$^+$] cations (blue triangles) and [NTf$_2^-$] anions (red squares) as a function of temperature, for a weighting factor w_c = 0.75 and at ambient pressure P = 0.1 MPa. Analytical laws determined empirically from experimental data [148] **are plotted for comparison.**

As a last step to confirm the k value of 0.75, the bulk shear viscosity at T = 303 K and P = 0.1 MPa was computed through equilibrium MD simulations using a Green-Kubo expression [66], still with the same weighting factor applied to the ions charges. The resulting viscosity value η was equal to 36 ± 5 mPa.s, to be compared with the experimental one of 32 mPa.s [146], the relative deviation of 13 % being within the range of statistical errors. Finally, the choice of w_c = 0.75 appeared to be relevant to predict both density and transport properties of the [mmIm$^+$][NTf$_2^-$]: this weighting factor has thus been adopted in this study. The whole parameter set of the IL force field is available in the Appendix B.

II.3 Lubricated nano-contact simulations

II.3.1 Surfaces generation and force field

As it was highlighted in the first chapter, the fluid/solid interface plays a major role on the studied rheology of a molecularly lubricated contact. Thus, the interaction of the fluid with the surfaces must be finely modeled. Different materials were considered in this work to study the influence of their properties on the interface phenomenology. To depict the case of a realistic steel-steel lubricated contact, iron oxide was first implemented in the confining simulations and most of the investigations of the system behavior were run with this solid. As Diamond-like-carbon (DLC) coatings proved to substantially improve the tribological performances of frictional systems, several carbon-based materials were then integrated and their influence on the confinement behavior were compared to the iron oxide one.

Iron oxide (FeO) force field

A huge part of mechanical systems, like rolling element bearings, are made of steel. The surface of carbon steel in contact with ambient air oxidizes and different compounds can result from the reaction (FeO, Fe_2O_3, FeO(OH)...) [149]. Among those compounds, iron oxide (FeO) is a relevant candidate to authentically describe the upper molecular layers of an engineering surface (see Figure II-6).

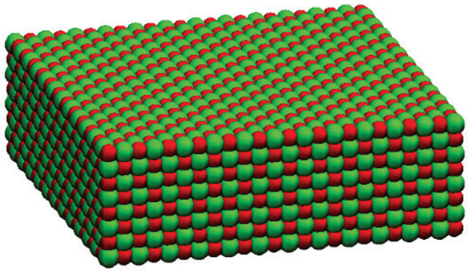

Figure II-6. Iron oxide surface. The numbers of oxygen ions (O^{2-} in red) and iron ions (Fe^{2+} in green) are the same. This way, the surface is polar but globally uncharged.

A force field developed by Cygan *et al.* [150] for crystalline structures and later validated for metal oxides [151] was implemented to describe the nature of the FeO interactions. In this force field, all the covalent bonds structuring the solid body are depicted through non-bonded Van der Waals and Coulombic interactions as described by Equation II.7. Here, to ensure the most realistic interaction with the fluid, the iron and oxygen atoms were set to their fully ionized configuration. The parameter set is given in the Appendix B. Finally, there is less than 4 % discrepancies between the lattice parameter of modeled FeO and its theoretical bulk value [152].

Carbon-based material force field

In the last chapter, the properties of different carbon-based materials as confining and shearing surfaces are explored. In those solids, the carbon presents different type of hybridizations. A sp^3 hybridized carbon features four bonds with other carbons (or other atoms) coordinated in a tetrahedral geometry. Similarly, sp^2 hybridized carbon presents three bonds in a same plane, and sp hybridized carbon, two lined up bonds. Here, the extreme cases of the two crystalline allotropes of carbon were first studied: graphite (sp^2 carbons only) and diamond (sp^3 carbons only) (see Figure II-7 a,b). In both cases, ideally flat surfaces were simulated. Tetrahedral amorphous carbon (ta-C) is a hydrogen-free DLC consisting of mainly sp^3-bonded amorphous carbon. It is used in numerous tribological applications [153]. Under working conditions, amorphous carbon (a-C) results from the ta-C coatings at the shearing interface. Hence, a-C is a good candidate to depict the interfacial behavior of a typical DLC coating. To model a-C, a 3-dimensional periodic volume of molten carbon was cooled and stabilized to nearly the solidification temperature (≈ 4000 K). From this state, two surfaces with different roughness where generated (see Figure II-7 c,d): the carbon volume was taken equal to 3000 K (roughest a-C) and 2000 K (smoothest a-C) at a cooling speed of 0.2 K/ps and blocs were cut out in the volume. Along one direction, each bloc has two free surfaces (with no periodic boundary condition) where carbon atoms are free to relax. Depending on the bloc temperature, it will differently modify the topography of the surfaces: at 2000 K, the carbon volume is fully solid so the surface structure will not rearrange more than necessary to be at an equilibrium state. At 3000 K more carbon atoms jump from one equilibrium location to another, causing an increase of the surface roughness. Once stabilized, both surfaces were cooled to ambient temperature before being integrated into shearing simulations.

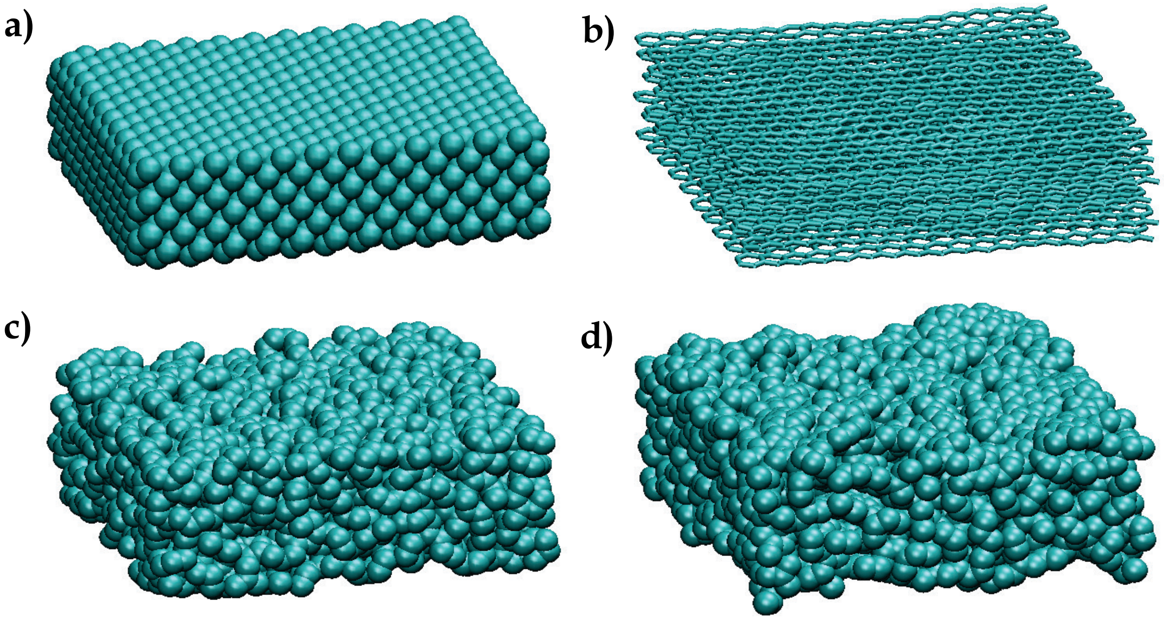

Figure II-7. Carbon-based surfaces representations. Representation with the atoms for the graphite a) and the smooth c) and rough d) a-C materials. Representation of the bonds for the graphite b), so the graphene layers are visible.

The reactive Tersoff potential [154] was invoked to represent the carbon-carbon interactions. First develop as a new force field for silicon (SiC), it was then adopted on repeated occasions to model carbon-based material interactions [155]. This potential describes, with a single expression, the force between the two atoms of breakable covalent bonds. For $r_{ij} < 1.8$ Å, exponential laws rules the interaction:

$$\boldsymbol{E_{Tersoff}} = \frac{1}{2}\sum_{i\neq j} f_C(r_{ij}).\left(Ae^{-\lambda_1 r_{ij}} - b_{ij}Be^{-\lambda_2 r_{ij}}\right) \tag{II.18}$$

with A and B two constants, λ_1 and λ_2 two atom-dependent parameters and b_{ij} a weighting coefficient including a three-body term to embody the bond ordering. For $r_{ij} \geq 2.1$ Å, the potential is null as the bond is broken and for $1.8 \geq r_{ij} \geq 2.1$ Å the potential smoothly tends towards 0 leaded by the $f_C(r_{ij})$ factor. The full analytical expressions and coefficient values of the force field are detailed in Appendix B. As graphite has a complex structure made of a piling of graphene layers, a hybrid force field is used with the Tersoff potential describing C-C bonds within graphene layers and a Lennard-Jones potential to model the non-bonded interactions between graphene layers. For this last material, the Tersoff force field coefficients were taken from Lindsay work [155] and the Lennard-Jones ones from the classic AMBER force field [156].

Wall-fluid interactions force field

Non-reactive force fields do not directly model the chemical reactions between the solid and the fluid bodies. They are inappropriate to study highly reactive species and long term oxidation/corrosion reactions. They are nevertheless a powerful instrument to describe the physisorption and the orientation of the molecules at the interface as well as the resulting tangential forces and velocities in a sheared system. Hence, only non-bonded Van der Waals and electrostatic interactions are modeled between the atoms of the surface and the ones of the IL. They are also described by Equation II.7 using the previously introduced Lennard-Jones and Coulombic coefficients mixed with the Lorentz-Berthelot rule.

II.3.2 System definition

To study the molecular lubrication, MD simulations are configured with the fluid confined and sheared between two sliding surfaces. Numerous data can be acquired through this method: arrangement and orientation of molecules, velocity and temperature profiles, energy transfers… Input parameters are also numerous: surface and fluid natures, lubricant thickness and sliding speed add to the thermodynamics variables of pressure, temperature.

Periodic boundary conditions are defined along both the x and y directions, thus simulating infinite surfaces. As for the bulk simulations, surfaces are about 5 nanometers long (x axis) and wide (y axis) for the fluid not to interact with itself. Given that in the center of a lubricated contact the film thickness is much smaller than the other dimensions the previous hypothesis is relevant to model molecular lubrication. As a consequence, the number of simulated lubricant molecules is constant between the surfaces. This is a major choice in the model configuration as with flat surfaces the full film lubrication condition is always fulfilled and no squeeze out of the fluid that would lead to local film breakdown can happen.

The solid surfaces are about 2 nanometers thick as the liquid/solid interactions are quasi non-existent beyond this distance. This way, the fluid experiences a contact with the surfaces as if they were semi-infinite solids. The operating conditions are set up on the two external atom layers of each surfaces according to the z direction (blue region in Figure II-8). The normal confining pressure is applied uniformly on the atoms of these control regions so each one support the following confining force F_{p_i}:

$$F_{p_i} = \frac{P_{conf} S}{n_c} \tag{II.17}$$

with P_{conf} the imposed confining pressure, S the surface section and N_c the number of atoms in a control region. In the shearing simulations, the sliding velocity is also applied to the same control regions by forcing the displacement along the x-direction to the desired speed. Half the value of the total shearing velocity is set up to each surfaces.

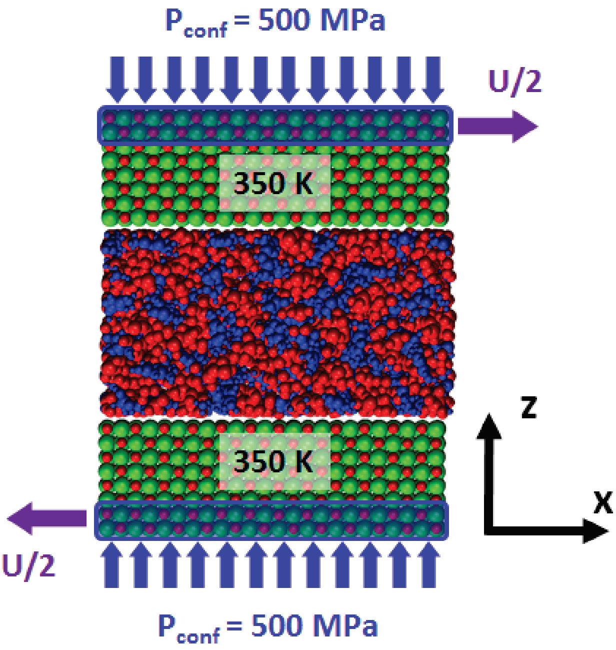

Figure II-8: Confined and sheared fluid principle. Highlighted in blue are the control regions where the pressure and the shearing velocity are imposed. The solid surfaces are entirely thermostated.

As one of the goals of this work is to study the thermal behavior of molecularly lubricated contacts and its influence on the rheology, no thermostat was directly imposed to the fluid so its temperature is free to evolve when it is sheared. However, as the solid thermal properties are not investigated here, the surfaces are fully thermostated with a Langevin thermostat [66] so the defined temperature T_{wall} is adjusted with a damping time of 100 time steps (being 0.2 ps). Hence, forcing to the same temperature all the surfaces is relevant for the comparison of the liquid/solid interface thermal behavior for the different studied cases.

Three steps were implemented to initialize the system. Firstly, an equilibration step was run without shearing and with no confining pressure applied on the surfaces so the fluid can relax between the walls. Secondly, the confining forces were added to the system so it progressively achieved an equilibrium state under confinement. Finally, a tangential relative motion was introduced between the two surfaces and sufficient simulation time (up to 2 ns) was run to ensure the sheared system achieved a steady state before data acquisition.

II.3.3 Quantities of interest

In simulations of the molecular lubrication regime, different outputs are generated and averaged over time. The shear stress and the film thickness are directly computed during the simulation and are regularly outputted. The shear stress $\tau = F_{\text{shear}}/S$ (with F_{shear} the total shear force measured on the control region of the confining walls) is deduced from the momentum supplied to the atoms of the control domain to keep their imposed velocity in the x direction while the contact thickness is defined as the arithmetic mean between the lubricant thickness and the distance between the two confining walls (see Figure II-9).

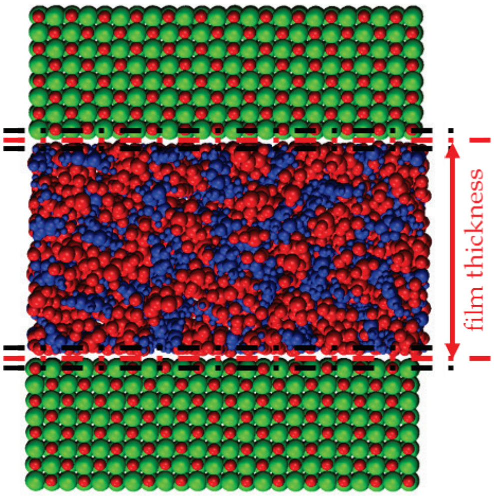

Figure II-9. Schematic representation of the film thickness calculation for smooth surfaces.

The velocity, temperature and local density of the fluid are all evaluated through their respective profile across the z direction. Each one is discretized in slabs that are about 1 angstrom thick and parallel to the xy plan. Atom number and velocities are measured in each distinct slab and averaged over multiple time steps to plot the different profiles. Snapshots of all the atoms positions are also regularly produced over short periods to generate visual renderings or to calculate the molecule orientations. All the other studied quantities (effective and apparent shear rates, friction, viscosity, slip length, fluid friction, average temperature and interfacial thermal resistance) can be deduced from the previous ones.

Finally, two classes of systems were configured and validated to investigate lubrication mechanisms by means of MD simulations: bulk fluid and nanoconfined fluid. With the first, the next chapter aims to characterize the rheology of ionic liquids, and more generally, of fluid lubricants, at high shear rates, for various conditions of pressure and temperature.

Chapter III: Rheology in thin films

This chapter offers a full picture of the $[\text{mmIm}^+][\text{NTf}_2^-]$ shear-rheological response to representative conditions of the elasto-hydrodynamic (EHD) and thin film regimes, based on MD simulations and with an experimental contribution. Most of this chapter is adapted from a paper accepted for publication in Tribology Letters. In a first section, experimental and numerical results in the linear regime are thoroughly evaluated, modeled and compared to prove the capability of molecular simulations to quantitatively predict the rheological properties. In a second section, the nonlinear domain is analyzed and the shear-thinning behavior of the ionic liquid is discussed and compared to the predictions of usual rheological models.

III.1 Linear regime

In this section, the opportunity to compare experimental findings with MD results is presented for the Newtonian (or linear) domain only. This includes the influence of temperature T and pressure P on low-shear viscosity η_0 and the deduction of the pressure-viscosity coefficients. To this end, a regression to the Carreau model (Equation I.1) was performed for each (T, P) couple of conditions to obtain the corresponding values of the Carreau equation parameters.

III.1.1 Methodology

A series of $(T, P, \dot{\gamma})$ cases was studied, in which T, P and $\dot{\gamma}$ were varied from 303 to 550 K, from ambient pressure up to 800 MPa, and from typically 10^7 to 10^{11} s^{-1}, respectively. The majority of the results were obtained from NEMD computations and the previously detailed Müller-Plathe method was employed to infer the viscosity at different shear rates. In a complementary manner, EMD simulations using the Green-Kubo formalism were also computed to derive the Newtonian viscosity in a different way, with the aim to offer a validation of the NEMD results. Thus, a total of nearly 200 cases were computed from 21 (T, P) conditions associated with different $\dot{\gamma}$ values. Figure III-1 shows a typical set of results obtained from arbitrarily selected conditions.

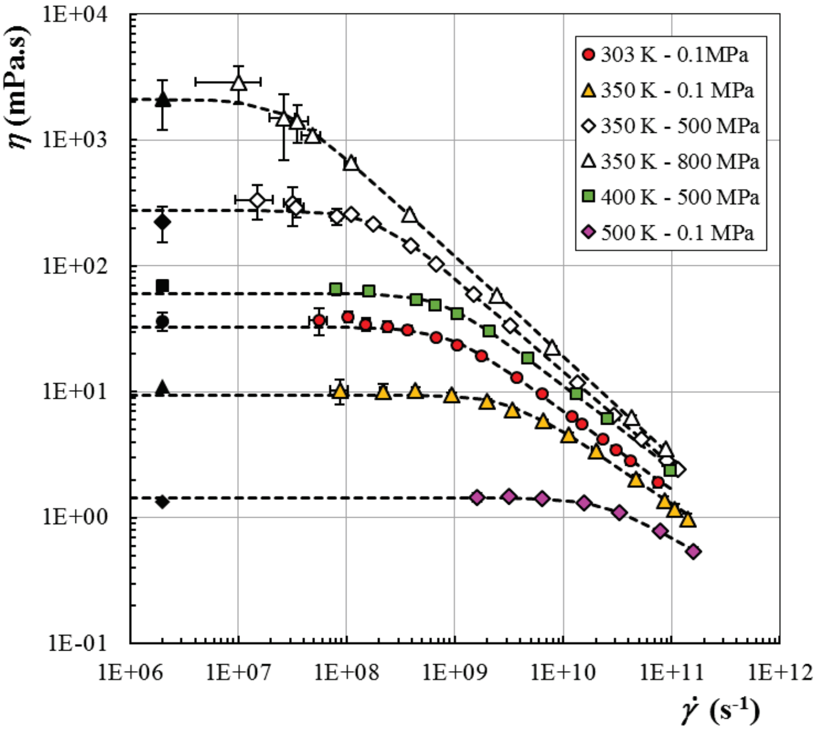

Figure III-1: Viscosity variations obtained from NEMD simulations of the [mmIm$^+$][NTf$_2$$^-$] ionic liquid versus shear rate at different (T, P) conditions, arbitrarily selected. Values obtained from the Green-Kubo approach are plotted with black symbols at an arbitrary shear rate of 2.10^6 s^{-1}. The dashed lines represent the regression of each configuration to the Carreau model (Equation I.1).

Whatever the case under consideration, the results follow a similar trend: first, a plateau is observed, followed by a continuous drop with a constant slope, suggesting a power-law trend. The plateau is characteristic of the Newtonian viscosity and the drop is induced by the shear thinning of the fluid. For the only 6 (T, P) couples (among the 21 effectively computed) reported in the Figure III-1, the viscosity values cover 4 orders of magnitude while the corresponding shear rates extend over more than 5 decades.

To strengthen the analysis, the Newtonian viscosities obtained from MD simulations were compared to the results of experimental measurements on the [mmIm$^+$][NTf$_2$$^-$] carried out at LaMCoS.

III.1.2 Analytical prediction model of the viscosity

Figure III-2 compares the two series of results obtained experimentally and numerically at ambient pressure over a range of temperature.

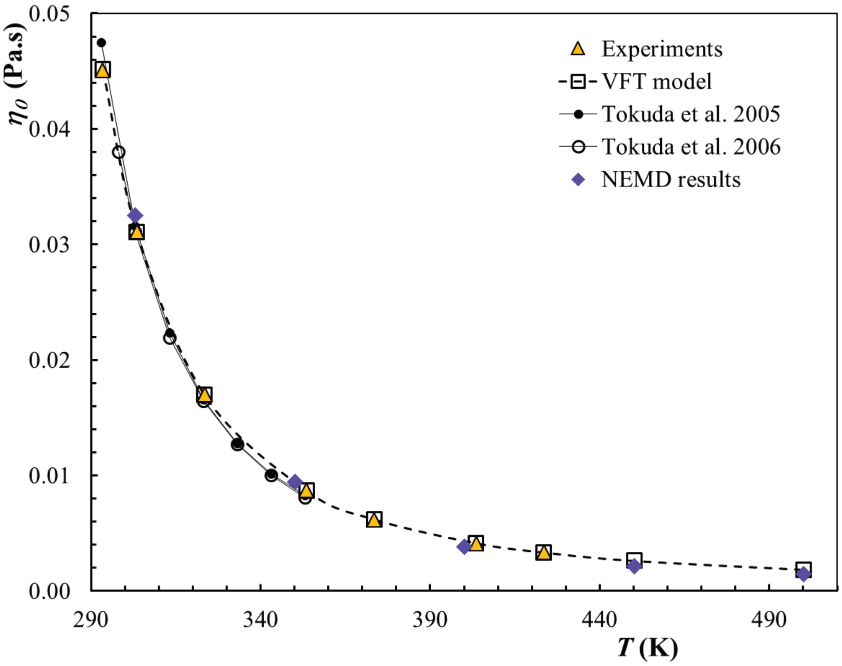

Figure III-2. Newtonian viscosity of the [mmIm$^+$] [NTf$_2^-$] ionic liquid at ambient pressure as a function of temperature. NEMD results are compared with measurements, including those of Tokuda et al. [148,157]**. The values resulting from a fit to the VFT expression are also reported with black open squares and dashed line.**

Overall, a good quantitative agreement was found even if some rather weak discrepancies are visible. By comparison with similar previous works, the self-consistence of the Newtonian viscosities variations versus temperature is triple checked in this work: the two computational approaches (NEMD and EMD-Green Kubo) highlighted before are completed by low shear-rate experiments. Finally, for confirmation purpose, but in the range 293-353 K, it is shown that the measured and simulated values agree well with those of Tokuda *et al.* [148,157] obtained experimentally for the same fluid, which are likewise plotted in Figure III-2.

The experimental results at ambient pressure were fitted to the Vogel-Fulcher-Tammann (VFT) empirical model [158] that has been often used in glass forming liquids which display a non-Arrhenius behavior, as it is the case with ionic liquids [159]. Its expression is given below, and the resulting viscosity values are also plotted in Figure III-2 (black open squares and dashed line).

$$\eta_0(T, P=0) = \eta_\infty \cdot exp\left\{\frac{D_F \cdot T_\infty}{T - T_\infty}\right\} \qquad (\mathrm{III.1})$$

where η_∞ is the viscosity extrapolated to infinite temperature, D_F the fragility parameter and T_∞ the Vogel temperature at which viscosity diverges. A regression of the VTF model to the experimental data gives η_∞ = 0.2546 mPa.s, D_F = 4.054 and T_∞ = 182.8 K.

The agreement between the viscosity values derived from NEMD simulations and those given by the VFT expression is very satisfying over the whole temperature domain investigated here, from 298 to 550 K. In fact, Equation III.1 also provides supplementary data which is required when it comes to consider the effect of pressure and temperature on viscosity. Assuming that a viscosity of η_g = 10^{12} Pa.s indicates the occurrence of a glass transition which is a typical value for lubricants at this specific state, it becomes possible to deduce the value of $T_g(0)$, the glass transition temperature at atmospheric pressure by making the assumption $T_g(0) \approx T_\infty$. With this approximation, we found $T_g(0) = 183$ K, thanks to the VFT model. This value was then directly introduced in a modified WLF-Yasutomi correlation [160] to allow the prediction of the Newtonian viscosity η_0, as a function of both temperature and pressure. This model is expressed as follows:

$$\eta_0(T,p) = \eta_g.exp\left[ln(10)\cdot\frac{-C_1\left(T-T_g(P)\right)\cdot F(P)}{C_2+\left(T-T_g(P)\right)\cdot F(P)}\right] \qquad \text{(III.2)}$$

with $T_g(P) = T_g(0) + A_1.ln(1+A_2.P)$ and $F(P) = (1+B_1.P)^{B_2}$, where $A_1, A_2, B_1, B_2, C_1, C_2$ are the model constants, and $F(P)$ the dimensionless relative thermal expansion function of the free volume.

The 6 parameters of the modified WLF-Yasutomi correlation were obtained by least mean square regressions of the experimental data using $T_g(0) =$ 183 K, as described before. The parameter values are reported in Table III-1.

Parameter (unit)	A_1 (°C)	A_2 (MPa^{-1})	B_1 (MPa^{-1})	B_2 (-)	C_1 (-)	C_2 (°C)	$T_g(0)$ (°C)	**Standard deviation**
From exp.	22.0997	$2,381\ 10^{-3}$	0,002346	-0,770	15,680	18.892	-90.159	2 %
From MD	1447.44	$2.063\ 10^{-5}$	0.002281	-0.8682	15.721	19.898	-90.159	9.4 %

Table III-1. Parameters and standard deviations of the modified WLF-Yasutomi correlation (Equation III.2) used to represent the viscosity variations with T and P of the $[\text{mmIm}^+]$ $[\text{NTf}_2^-]$ ionic liquid. Parameters are inferred from the Newtonian viscosity of experimental and MD measurements.

In Figure III-3, the experimental results are plotted with yellow squares and the modified WLF-Yasutomi predictions from those values are plotted with yellow lines. The uncertainty of the experimental data is lower than 3 %. With a standard deviation of 2.1 % calculated on the whole experimental dataset, Equation III.2 provides a very good fit to the measurements which makes almost impossible to distinguish the experimental points from the calculated values in a graph that spans over several orders of magnitude in viscosity. The Newtonian viscosities obtained through MD simulations are represented by black stars connected by black dashed lines whereas the values obtained from the modified WLF-Yasutomi model (applied to these computations) are drawn with continuous black lines. The values of the parameters of this second correlation are given in the last line of Table III-1: it should be emphasized that the $T_g(0)$ value was the same as for the regression to the high pressure measurements, meaning that this experimental parameter was used to fit the results of numerical simulations. The regression has led to a rather good estimate of the MD predictions, with a standard deviation of 8.8 % obtained for 19 (T, P) cases out of the 21 studied here. The two cases at 550 K were not considered as the temperature is out of the range that the WLF model can estimate accurately. This has also enabled to keep the (T, P) domain not too large compared with the experimental one, also not to overburden the graph with values obtained at unusual temperatures for a lubricant.

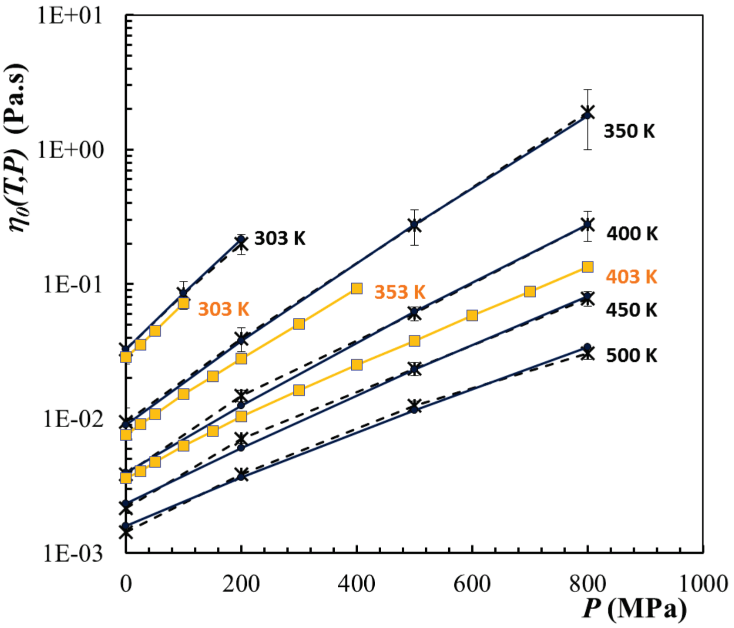

Figure III-3. Viscosity versus pressure at different temperatures for the [mmIm$^+$][NTf$_2^-$] ionic liquid. The experimental results are plotted with yellow squares and the corresponding modified WLF-Yasutomi predictions with yellow lines. NEMD results are represented by black stars and dashed lines, the results of the modified WLF-Yasutomi expression applied to these computations are traced with dark blue lines.

The comparison between experiments and simulations shows a fair quantitative agreement at 303 and 350 K, where the visual differences on the pressure influence are amplified by i) the deviation between the initial viscosities at 303 K and ii) by a temperature difference between the tests and the computations (353 vs. 350 K). However, a clear overestimation of the pressure influence on viscosity by molecular computations is observed at 403 K. The Newtonian viscosity is linked to the self-diffusion coefficient D through the Stokes-Einstein equation:

$$D = \frac{k_B T}{6\pi\eta R} \tag{III.3}$$

with k_B the Boltzmann's constant, T the temperature and R the hydrodynamic radius of the molecule. Hence, the observed deviation of the Newtonian viscosity is consistent with some previous observations stating that the self-diffusion coefficient is underestimated when calculated by means of MD simulations [161,162].

III.1.3 Pressure viscosity coefficient

At this stage, it appeared necessary to compare these results with reference data in order to assess both the experimental and the computational studies, and to validate the models used so far. Considering the frame and the main objective of this work, *i.e.* the EHD and very thin film regimes and to offer a new way to access the lubricant characteristics required for estimating film thickness, the more critical and discussed parameter is certainly the PVC at the contact inlet temperature. In the literature, several definitions of the PVC coexist. One commonly used is the secant PVC coming from the Barus relation [163]:

$$\eta(T,P) = \eta(T,0)e^{\alpha(T,P)P} \qquad \text{(III. 4)}$$

where α is the PVC. This definition is extremely accurate but α depends on the pressure what greatly limits its range of application. Otherwise, in their reference work for predicting film thickness in EHL, Hamrock and Dowson [164] actually used α^*, the reciprocal asymptotic isoviscous pressure coefficient proposed by Blok [165] and defined by:

$$\frac{1}{\alpha^*} = \int_{0.1}^{\infty} \frac{\eta_0(T,\ 0.1)}{\eta_0(T,P)} dP \qquad \text{(III. 5)}$$

This PVC has first the advantage to be pressure independent. Using the Hamrock and Dowson expressions [164], it is also relevant to properly foresee the EHD film forming capacity as it was, for instance, reported by Chaomleffel *et al.* [166] for a very wide range of operating conditions, including the EHL and thin film regimes, and also for a broad collection of lubricants of different molecular natures. There is, however, a limitation for using α^*: as it is derived from an integration, the residue must be negligible or nearly negligible, which means that the ratio $\frac{\eta_0(T,0.1)}{\eta_0(T,P)}$ must tend to zero when P becomes sufficiently high. Since most of the PVC data arise from experiments, this condition implies that the pressure range and thus, the maximum pressure, should be large enough. In his book, Bair [167] recommends to reach a maximum pressure P_{max} of, at least, $3/\alpha^*$to make sure that the derived PVC value is correct.

The observation reported in 2008 by Pensado *et al.* [48], who emphasized the lack of conclusive works in the literature on the viscosity-pressure dependence in ionic fluids, is still topical. Up to now, no pressure-viscosity data were published on the [mmIm$^+$][NTf$_2^-$] ionic fluid. Ahosseini and Scurto [159] studied the [emIm$^+$] [NTf$_2^-$] (1-ethyl-3-methylimidazolium bis(trifluoromethylsulfonyl)imide) whose molecular structure is very similar to that of the fluid under consideration in this work. However, the pressure domain in [159] was limited to 125 MPa making it impossible to determine a pressure-viscosity coefficient like α^* within an acceptable accuracy. In fact, the PVC of this type of fluids is expected to be rather low [48,159], in the typical range from 10 to 7 GPa^{-1} at 313-353 K, meaning that the pressure domain must extend to a minimum of respectively 330 to 430 MPa, in accordance with the $P_{max} \geq 3/\alpha^*$ condition.

The α^* values calculated from the two regressions by the modified WLF-Yasutomi correlation to both experimental and MD results on [mmIm$^+$][NTf$_2^-$] are plotted in Figure III-4, for temperatures lying from 298 to 450K. In this range, compared with the values obtained from the experiments, those calculated from molecular computations overestimate α^* by 6 to 14%, respectively. As the absolute gap remains nearly constant when T varies, it is the continuous drop of α^* with T which leads to an increase of the relative deviation. The reciprocal asymptotic isoviscous pressure coefficients from the works of Harris *et al.* [1] on [bmIm$^+$][NTf$_2^-$] are also reported in Figure III-4, with brown diamonds: α^* was calculated from the tabulated data obtained at 298, 323 and 348 K. This ionic fluid has a similar molecular structure to the one considered in this study, except one longer alkyl chain in the cation, 1-butyl-3methylimidazolium instead of 1-3-dimethylimidazolium. According to the literature, a longer alkyl chain results on a significant increase of the viscosity at ambient pressure [48], but has a rather weak influence on the PVC [168]. By analogy with other fluids of similar molecular size, the low values of the PVC found here can also be attributed to the very compact shape of the ions. It must also be noticed that the corresponding maximum pressure in [1] are equal to 150, 250 and 300 MPa, meaning that the $P_{max} \geq 3/\alpha^*$ condition is somewhat violated. The P_{max} value should have been higher by approximately 100 MPa at each temperature step: this lack of data at appropriate pressures has a higher effect at 298 K compared to 348 K. Given the above remarks and comments, it can be concluded that the results derived from the tests by Harris *et al.* [1] on [bmIm$^+$][NTf$_2^-$] confirm qualitatively and quantitatively the viscosity-pressure coefficients found from experiments and MD simulations on the [mmIm$^+$][NTf$_2^-$] ionic fluid. This is particularly well verified at 348 K, where the uncertainty on α^* from [1] is certainly the lowest.

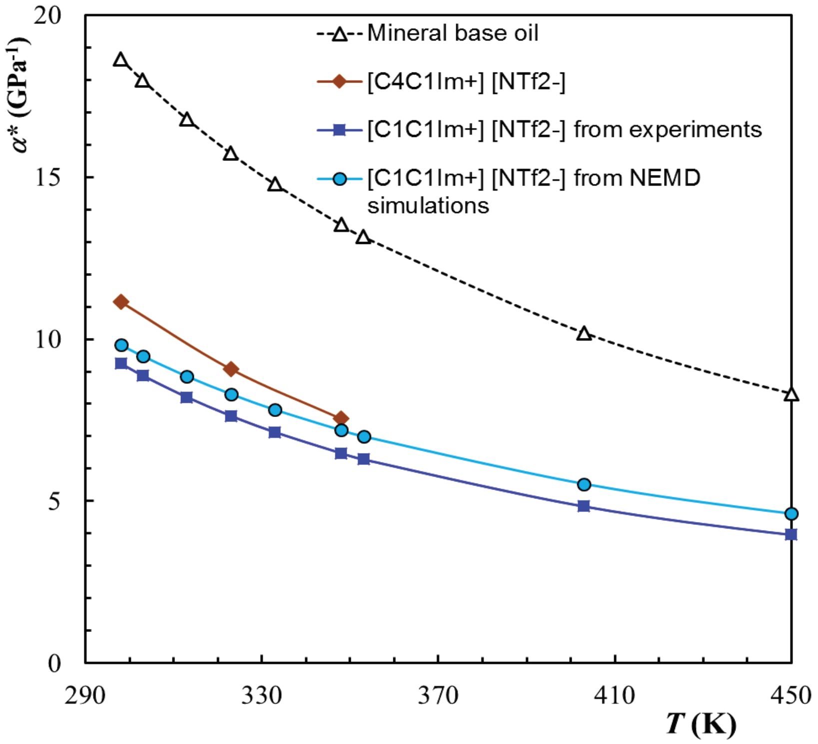

Figure III-4. Variations of α^*, the reciprocal asymptotic isoviscous pressure coefficient [165], **as a function of temperature calculated from: i) WLF-like correlation applied to experimental results (blue squares) and MD simulations on [mmIm$^+$][NTf$_2^-$] (light blue circles), ii) Harris et al. experimental results [1] on [bmIm$^+$] [NTf$_2^-$] and iii) WLF-like correlation applied to experimental results on a mineral base oil** [160] **(triangles).**

The gap found between the two approaches is acceptable, given that α^* appears in film thickness formulae with a power exponent of nearly 0.5 which limits the consequences of this deviation. For comparison with the properties of conventional lubricants, the α^* variations with T obtained on a hydrocracked mineral base oil (from [160]) are also plotted in Figure III-4. This lubricant was chosen in such a way that its viscosity at ambient pressure is close (lower by 10 to 20%) to that of the ionic fluid. This further comparison clearly evidences that this class of ionic fluids exhibits lower PVC but that its variations with temperature are very similar to those of the lubricants currently in use. Thus, their potential, from the film thickness capacity point of view, is clearly evidenced: it is equal or better than that of conventional fluids, given that ionic fluids properties at ambient pressure are more stable with T variations, and that it is easily possible to adapt their structure (*e.g.* the length of the alkyl chains of the cations) for adjusting / optimizing their characteristics.

III.2 Non-linear regime

After having confirmed the prediction of the viscosity plateau at low shear rates through molecular computations, this section is devoted to the analysis of the nonlinear response of the ionic liquid rheology at high shear rates (see Figure III-1). As a large number of cases were simulated, the first step consists in normalizing the viscosity with respect to a reference configuration. This way, a comparison is possible between the evolutions of the viscosity with the shear rate when shear thinning occurs. Once on the same basis, the evolution of the parameters issued from the regression of each cases to the Carreau model introduced in section I.1.3 can be analyzed. The expression of the Carreau law is recalled here as it will be widely referred to in this section:

$$\eta = \eta_0[1 + (t_{rel}.\dot{\gamma})^2]^{\frac{N-1}{2}} \tag{I.1}$$

with the Newtonian viscosity η_0, the relaxation time t_{rel} and the exponent N, three values inherent to the fluid, and $\dot{\gamma}$ the shear rate taken by the fluid.

First the physical meaning of relaxation time is put forward to explain its evolution. Second, the N exponent is carefully characterized and is described by an analytical expression in order to improve the viscosity prediction of the Carreau model.

III.2.1 Normalization procedure

Given the very large number of computed cases and the wide extension of the domains in both viscosity and shear rate, the simulations results of the 21 (T, P) conditions cannot be directly treated as such as it is quite impossible to directly compare them either quantitatively or qualitatively. At this point, the method of reduced variables, which is the standard rheological application of time–temperature–pressure superposition [4,53,169], is put into practice. It is a well-established technique for collapsing the rheological results of a given material obtained at different temperatures, pressures and shear rates onto a unique (or master) curve, characteristic of that material. In accordance with Bair *et al.* [169], it is possible to calculate the reduced viscosity $\eta^* \left(= \eta / a_\eta\right)$ and the reduced shear rate $\dot{\gamma}^* \left(= a_{\dot{\gamma}} . \dot{\gamma}\right)$, with a_η and a_γ the shift factors given by

$$a_\eta = \frac{\eta_0(T,P)}{\eta_0\left(T_{Ref}, P_{Ref}\right)} \tag{III.6}$$

$$a_{\dot{\gamma}} = \frac{\eta_0(T,P).T_{Ref}.\rho\left(T_{Ref}, P_{Ref}\right)}{\eta_0\left(T_{Ref}, P_{Ref}\right).T.\rho(T,P)} \tag{III.7}$$

where T_{Ref} and P_{Ref} define a reference state for the rescaling of η and $\dot{\gamma}$, ρ and ρ_{Ref} are the fluid density values at any (T,P) condition and at the reference state, respectively.

The reference state was chosen at T_{Ref} = 303 K and P_{Ref} = 0.1 MPa as it is the closest to ambient conditions. The technique was thus applied to the entire set of MD results and the corresponding values are plotted in Figure III-5.

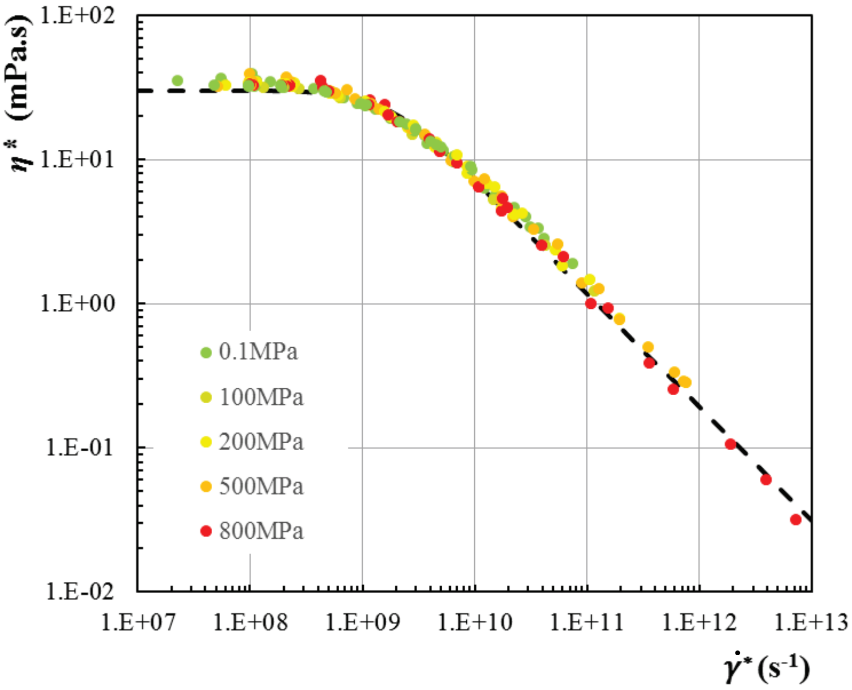

Figure III-5. Results obtained from nearly 200 NEMD simulations, after viscosity and shear rate rescaling using Equations III.6 and III.7, with a reference state defined by T_{Ref} = 303 K and P_{Ref} = 0.1 MPa.

This figure firstly illustrates how the MD rheological data obtained for [mmIm$^+$][NTf$_2^-$], initially spreading over many orders of magnitude of viscosity, now converge well onto a single master curve, justifying this way the employed shift factors expressed by Equations III.6 and III.7. Secondly, the good overlap shown in Figure III-5 enables the estimation of the viscosity value of this ionic liquid at any (T,P) condition, provided that the corresponding $\rho(T,P)$ and $\eta_0(T,P)$ values are known. However the ideal way to quantitatively foresee the rheological properties at any $(T,P,\dot{\gamma})$ condition requires the introduction of a relevant model. To achieve this goal, the Carreau relationship, as expressed by Equation I.1 in [51], comprises three parameters which have a fundamental meaning for describing the rheological response of a material submitted to extreme values of shear rate at any (T, P) condition: η_0, the Newtonian viscosity already introduced, t_{rel}, the relaxation time directly related to the shear rate for which the onset of non-Newtonian (or non-linear) behavior occurs, and N, the power-law exponent reflecting the degree of non-linearity of the viscosity-shear rate dependency.

III.2.2 Improvement of the Carreau model

The regression to the Carreau law was carried out on the entire set of almost 200 rescaled cases and is plotted in Figure III-5 by the dashed black line. It gave the following values: η_0 = 29.7 mPa.s, t_{rel} = 0.605 ns and N = 0.212. In order to evaluate the quality of the regression, the coefficient of determination R^2 was introduced:

$$R^2 = 1 - \frac{SS_{residual}}{SS_{total}} \tag{III.8}$$

where $SS_{residual}$ and SS_{total} are respectively the sum of the squares of residuals and the total sum of the squares and are defined as :

$$SS_{residual} = \sum_i \left(\eta_i(P, T, \dot{\gamma}) - \eta_{c_i}(P, T, \dot{\gamma})\right) \tag{III.9}$$

$$SS_{total} = \sum_i (\eta_i(P, T, \dot{\gamma}) - \bar{\eta}) \tag{III.10}$$

with $\eta_i(P, T, \dot{\gamma})$ the viscosities for all the conditions of pressure P, temperature T and shear rate $\dot{\gamma}$; $\eta_{c_i}(P, T, \dot{\gamma})$ the viscosities predicted by the Carreau model for all the same conditions and $\bar{\eta}$ the overall mean of the viscosity. R^2 is equal to 0.994 what reflects the pretty good prediction capability of the Carreau model. Nevertheless, even if the Newtonian viscosity is very close to the experimental values mentioned before, a significant discrepancy is found on both t_{rel} and N, indicating an apparent inadequacy or incompleteness of the model. As a matter of fact, the regressions to the Carreau model computed for each of the 21 (T, P) couples give non constant N values, which range from 0.20 to 0.52 (see Table III-2). Note that η_0 and t_{rel} are missing at 303 K for pressures of 500 MPa, because it has been impossible, at those (T, P) conditions, to get reliable results in the linear domain with acceptable simulation times. Also, the N values obtained at 0.1 MPa and temperatures of 450, 500 and 550 K have to be considered with care because, for those conditions, the studied nonlinear domain was rather limited.

$\boldsymbol{P}$ (MPa)	$\boldsymbol{T}$ (K)	$\boldsymbol{\eta_0}$ (mPa.s)	$\boldsymbol{t_{rel}}$ (ns)	$\boldsymbol{N}$
0.1	303	32.5	1.15	0.375
	350	9.46	0.31	0.419
	400	3.87	0.12	0.470
	450	2.17	0.07	0.483
	500	1.44	0.04	0.505
	550	1.01	0.03	0.521
100	303	85.0	2.56	0.323
200	303	200	4.72	0.277
	350	39.5	1.01	0.342
	400	14.8	0.41	0.420
	450	7.04	0.17	0.448
	500	3.84	0.09	0.475
500	350	275	5.21	0.257
	400	60.6	1.28	0.340
	450	23.5	0.46	0.381
	500	12.6	0.25	0.433
	550	7.67	0.16	0.481
800	350	2109	38.4	0.211
	400	277	5.23	0.285
	450	78.3	1.39	0.337
	500	30.7	0.54	0.389

Table III-2. η_0, t_{rel} and N values from regressions to the Carreau model of the NEMD viscosity-shear rate curves obtained at different pressures and temperatures.

To explore the possible improvements of the Carreau model, the relaxation time t_{rel} and the exponent N are successively considered to characterize their evolution.

Relaxation time predictions

It is imperative to analyze the relevance of the t_{rel} values derived from the regressions to the Carreau equation (Equation I.1), given that it was previously observed that the Newtonian viscosities found this way are quantitatively comparable with those obtained numerically. The relaxation time t_{rel}, fitted from a Carreau formula is comparable to the molecular relaxation time, estimated from the equilibrium fluid properties by using the following expression:

$$t_{rel} = \frac{d^2}{D} \qquad \text{(III.11)}$$

where D is the average self-diffusion coefficient and d the typical ion size. For instance at the reference conditions ($T = 303$ K and $P = 0.1$ MPa), the fitted relaxation time of 1.15 ns is close to the ca. 2 ns estimated through the Equation III.11. However, the multiple combinations of T and P simulated in the current work lead to t_{rel} variations extending over a wide range, typically from 0.03 to more than 30 ns (Table III-2). Thus, another way, more consistent, was needed for the assessment of the t_{rel} values. In the Carreau expression, the relaxation time is analogous to the inverse of the critical shear rate $\dot{\gamma}_c$, where the viscosity vs. shear rate curve departs from the Newtonian trend. Furthermore, it is possible to express Equation III.7 as follows, multiplying each term by $\dot{\gamma}$:

$$\dot{\gamma}^* = \left(\eta_0(T,p).T_{Ref}.\rho_{Ref}\right)/\left(\eta_0\left(T_{Ref},p_{Ref}\right).T.\rho(T,P)\right)\cdot\dot{\gamma} = a_{\dot{\gamma}}\cdot\dot{\gamma}$$

Considering that $\dot{\gamma}^*$, T_{Ref}, ρ_{Ref} and $\eta_0\left(T_{Ref},p_{Ref}\right)$ are constants, after substitution of these parameters in the two terms of the left hand side equality into a single one, one gets

$\dot{\gamma} = \rho(T,P)\cdot T/\left(K\cdot\eta_0(T,P)\right)$, where K is a constant

Finally, at the critical shear rate, $\dot{\gamma}_c$, one may writes

$$t_{rel} = \frac{1}{\dot{\gamma}_c} = K\cdot\frac{\eta_0(T,P)}{\rho(T,P)\cdot T} \qquad \text{(III.12)}$$

On the basis of Equation III.12, it is now possible to check if the t_{rel} values, given by regressions of the viscosity variation obtained at different (T,P) to the Carreau model, vary proportionally with the ratio $\eta_0(T,P)/\,(\rho\cdot T)$. The variations of t_{rel} derived from the Carreau fits as a function of $\frac{\eta_0(T,P)}{\rho\cdot T}$ are plotted in Figure III-6.

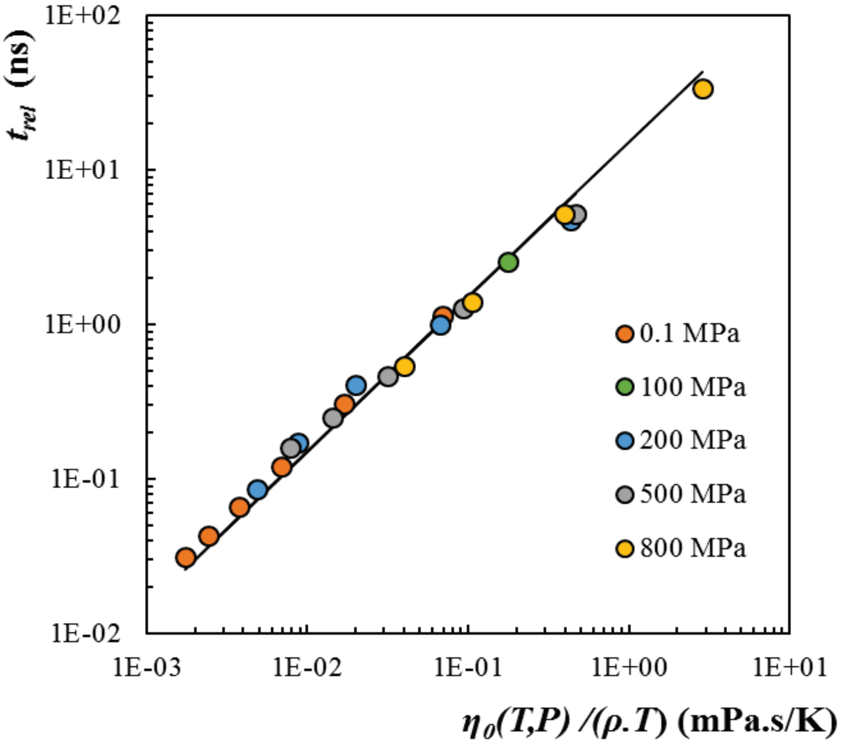

Figure III-6. Relaxation times in the [mmIm$^+$] [NTf2$^-$] ionic fluid obtained from regressions to the Carreau equation as a function of $\eta_0(T,P)/\rho\cdot T$. The color of the symbols refers to the different pressures simulated by NEMD, the black line represents a linear regression of t_{rel} vs $\eta_0(T,P)/\rho\cdot T$.

For K = 15.17, a linear relationship is clearly found (see black line in Figure III-6), characterized by a coefficient of determination R^2 = 0.993, meaning that Equation III.12 is verified. More important here, it indicates that the relaxation times derived from regressions to the Carreau model are not purely numerical parameters without meaning, but relevant results from the rheological and physical points of view.

Characterization of the evolutions of the N exponent

The variations of N as a function of temperature at different pressures, as reported in Table III-2, are plotted in Figure III-7, which clearly evidences that N can no longer be taken as a constant parameter. The clear trends on the temperature and pressure dependencies of N incite to propose a model. In the absence of theoretical background, arbitrarily plausible forms were selected to permit an accurate estimation of N for various (T, P) conditions. Firstly, a logarithmic function is used to represent the temperature influence on t_{rel}, at constant pressure. Thus, one may write:

$$N = A_{N,P} \cdot ln(T) - B_{N,P} \tag{III.13}$$

at a given pressure P, where $A_{N,P}$ and $B_{N,P}$ are two pressure dependent parameters.

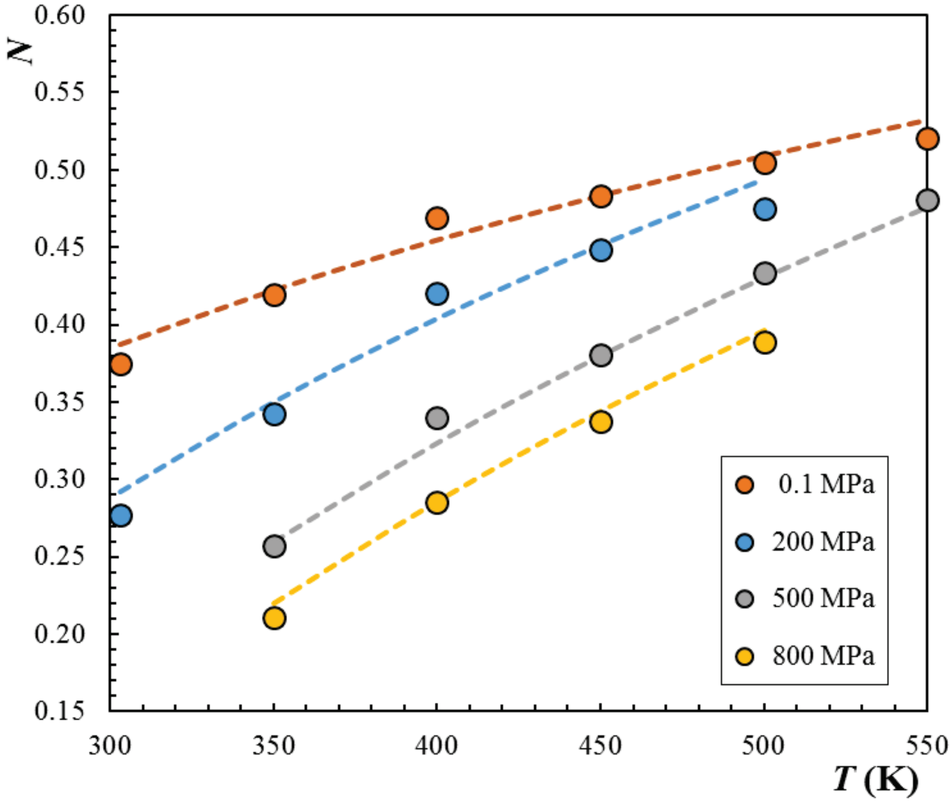

Figure III-7. Variations of N, obtained by regressions of the NEMD results to the Carreau equation (circles), versus temperature at different pressures. The dashed lines represent the values computed from Equation III-13.

In addition, the two parameters of Equation III.13 were found to vary monotonically with P, as shown in Table III-3 and by Figure III-8.

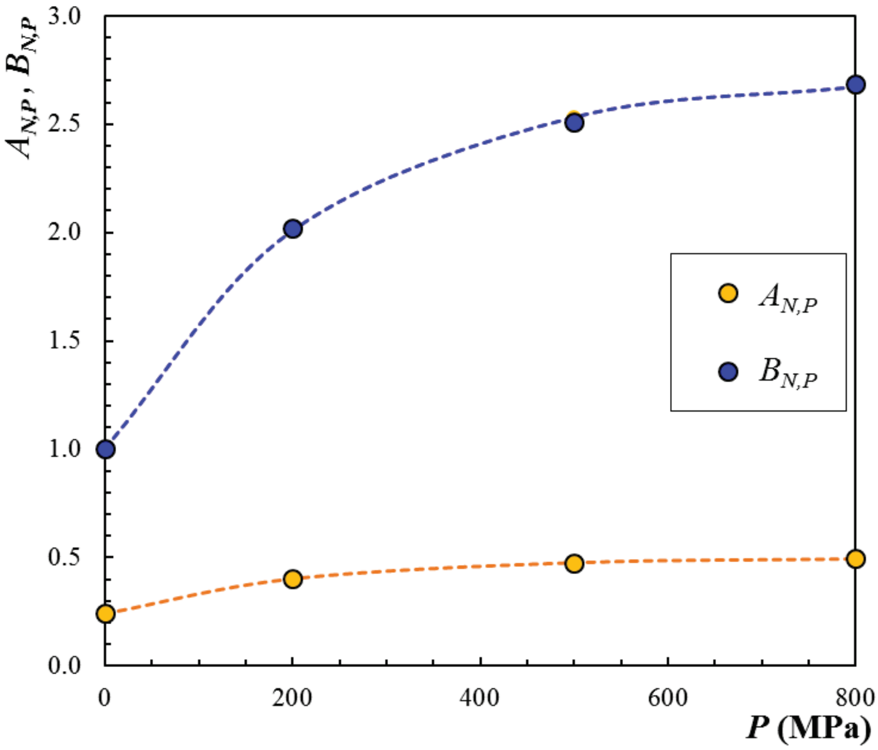

Figure III-8. Variations of $A_{N,P}$ and $B_{N,P}$ with pressure and their fitting (dashed lines) to arbitrary exponential-like expressions (Equations III.14 and III.15).

P (MPa)	$A_{N,P}$	$B_{N,P}$
0.1	0.243	1.001
200	0.403	2.019
500	0.474	2.512
800	0.495	2.684

Table III-3. Pressure dependence of the parameters of Equation III.13 proposed to represent the variations of the Carreau exponent, N, with T.

The two parameters $A_{N,P}$ and $B_{N,P}$ are arbitrarily approximated by exponential-like expressions

$$A_{N,P} = 0.2557 \cdot \left(1 - e^{(1-0.0049 \cdot P)}\right) + 0.243 \qquad \text{(III.14)}$$

$$B_{N,P} = 1.7209 \cdot \left(1 - e^{(1-0.0044 \cdot P)}\right) + 1.001 \qquad \text{(III.15)}$$

Equations III.14 and III.15 give a very accurate representation of $A_{N,P}$ and $B_{N,P}$ variations with pressure. Thus, combining now Equations III.13, III.14 and III.15 enables to express the variation of N, the Carreau exponent which reflects the ionic liquid non-linear behavior, by:

$$N = \left[0.2557 \cdot \left(1 - e^{(1-0.0049 \cdot P)}\right) + 0.243\right] \cdot ln(T) - \left[1.7209 \cdot \left(1 - e^{(1-0.0044 \cdot P)}\right) + 1.001\right] \qquad \text{(III.16)}$$

with T and P expressed in K and MPa.

The values of N calculated from Equation III.16 are plotted with the dashed lines in Figure III-7, and compared with those obtained from regressions of the NEMD results to the Carreau equation. From this figure, it is clearly demonstrated that the empirical model described before predicts N with a good precision, within a standard deviation of 0.006 (R^2=0.994), for T and P ranging from 300 to 500 K and from 0.1 to 800 MPa, respectively.

Besides, the MD results made it possible to describe the N variations in a rather more straightforward and physical way. Indeed, it was found that the N variations with T and P could be related to t_{rel}, the Carreau relaxation time, itself varying as a function of $\frac{\eta_0(T,P)}{\rho(T,P)\cdot T}$, as shown in Figure III-6. More remarkably, the drop of N with increasing t_{rel} (e.g. when P is increased or T is decreased) follows a logarithmic function, as clearly revealed in the graph of Figure III-9. The black line in this figure was obtained by a logarithmic regression to the N values expressed as:

$$N = a.\ln(t_{rel}) + b \qquad (\mathrm{III.17})$$

where a, b and R^2 were found equal to -0.0474, 0.362 and 0.973, respectively.

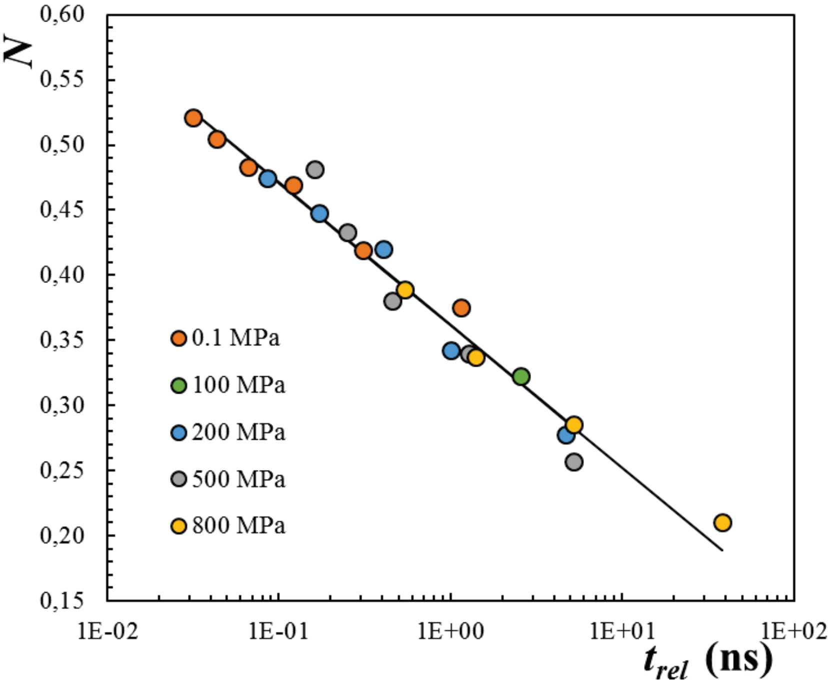

Figure III-9. Variations of N, the Carreau exponent with t_{rel}, the relaxation time and their regression (black line) to a logarithmic dependence (Equation III.17).

Equation III.17 gives a fairly accurate representation of N variations with pressure and temperature: the results are plotted with dotted lines in Figure III-10, and compared with the values from Table 2. The proposed model predicts N within a standard deviation of 0.031 (R^2=0.986), for T and P ranging from 300 to 550 K and from 0.1 to 800 MPa, respectively. Thus, it is clearly demonstrated that N, which reflects the ionic liquid non-linear behavior, can be predicted with a good precision from the relaxation time. The longer t_{rel} (or the higher the pressure or the lower the temperature), the lower N (or the higher the shear-thinning effect).

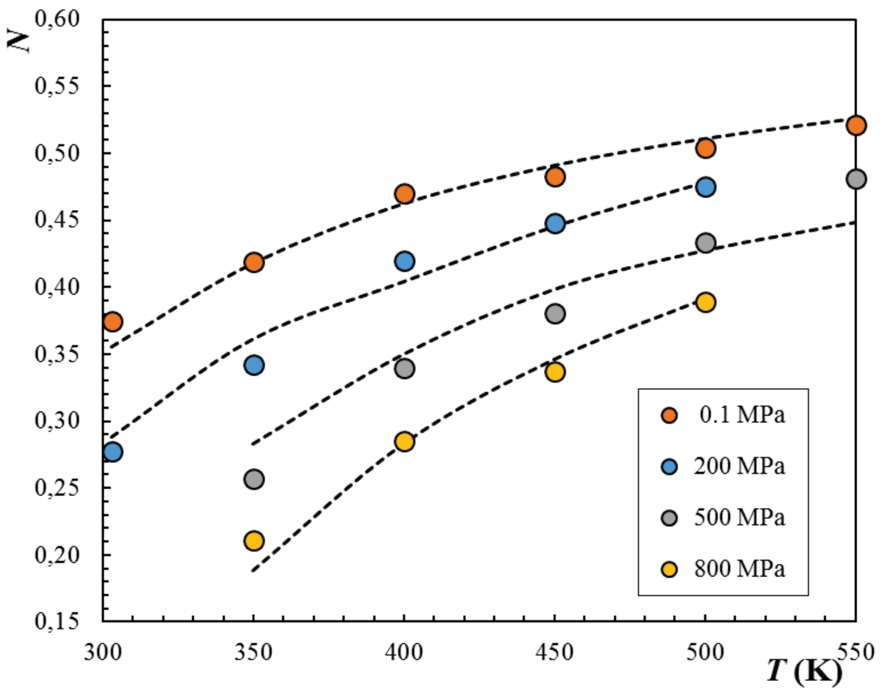

Figure III-10. Prediction of N at different pressures and temperatures (black dotted lines) compared with the results from the regressions of the molecular simulations to the Carreau law.

Finally, beyond the prediction of N with two different expressions, the variation of the exponent shows that at high pressure and low temperature, the influence of the shear rate on the viscosity is more important (lower N). This observation has a direct influence on film thickness, which one might decrease quickly leaded by an important drop of viscosity.

III.3 Conclusion

In this chapter was described the rheological characterization, for application in the EHD and thin film lubrication regimes, of the [mmIm$^+$][NTf$_2^-$] ionic liquid. Representative temperature, pressure and shear rate domains were investigated by a complete approach, comparing over 200 molecular dynamics computations results to rheological measurements.

The comparisons between experimental results and those obtained by MD simulations in the linear domain have demonstrated the ability of the employed numerical techniques to quantitatively predict two essential properties: the viscosity and the pressure viscosity coefficient (PVC), and their variations with temperature. Compared with a conventional mineral lubricant oil of almost the same Newtonian viscosity at room condition, the PVC of the ionic fluid is lower, but its variation with temperature remains very similar.

The application of the time-temperature-pressure superposition principle and regressions of the NEMD results to the Carreau expression have shown that appropriate time relaxation values can be derived from the latter. However, MD simulations has revealed, for the first time, the variations of N, the nonlinear exponent, as a function of temperature and pressure. An empirical modeling of the N changes versus T and P was proposed as well as a direct relation with the relaxation time was evidenced. The observed variations of the exponent also demonstrate a higher sensibility of the viscosity, and thus of the film thickness, at high pressure and low temperature.

Overall, this study provides the evidence that the behavior of rather complex fluids, like ionic liquids, can be studied in a meaningful way by means of molecular simulations with an experimental contribution. A full picture of the [mmIm$^+$][NTf$_2^-$] shear-rheology to representative conditions is now accessible. It is a complementary way to purely experimental measurements.

In the next chapter, the exhaustive characterization of the [mmIm$^+$][NTf$_2^-$] bulk rheology will be compared to the response of [mmIm$^+$][NTf$_2^-$] in nanoconfinements and the associated molecular lubrication mechanisms can be investigated.

Chapter IV: Confinement and shearing

In this chapter, the [mmIm$^+$][NTf$_2^-$] ionic liquid is confined between two model surfaces of a steel-steel contact: iron oxide surfaces (see Figure II-6). The system response to confinement and shearing were studied qualitatively and quantitatively to better understand the mechanisms of molecular lubrication. A large part of the results and discussions of this chapter were published in the journal Physical Chemistry Chemical Physics (PCCP).

First without shearing, the structuration and the orientation of the fluid molecules near the interfaces were analyzed. Hypothesis could be drawn up on their incidence on the lubrication performances. The response of the fluid and of the liquid/solid interface to shearing were analyzed one after another. Then, the complex role of the temperature were carefully depicted.

IV.1 Structuration and orientation under confinement

Some specific structuration and orientation of the fluid molecules take place near the liquid/solid interfaces. They result from the reaction of the fluid with the structured atoms of the solid surface and from the nanoconfinement. Both are studied in this section as they can influence i) the fluid rheology near the interface and ii) the fluid/solid interaction and that way, the interfacial velocity slip, the tribofilm formation and the possible chemical reactions.

IV.1.1 Density profile

When confined between two surfaces, the ionic liquid loses its homogeneous structure with respect to the direction perpendicular to the walls. Figure IV-1 shows the ion density profiles of 188 [mmIm$^+$][NTf$_2^-$] pairs confined between two iron oxide (FeO) surfaces at T = 350 K and under a normal pressure P_{conf} = 500 MPa. The resulting film thickness is 28.4 Å for a non-sheared confinement. Well-defined ion layers were observed close to the surfaces, with first density peaks reaching ca. 220 and 135 % of the bulk density for the cations and anions, respectively. Cations and anions were well represented in every formed layer, implying that no monolayer of a single ionic type was present at the interface. The amplitude of the layers density declined with the distance from the walls, and almost vanished after two occurrences. Thus, the average density in the central region of the confinement was very close to the IL bulk one: the mean density in the central zone of the confinement (between 25 and 35 Å in Figure IV-1) is 1.69 g/cm^3 vs. 1.72 g/cm^3 for the bulk density computed from the bulk simulations of Chapter III in the same conditions of pressure and temperature (P_{conf} = 500 MPa and T = 350 K).

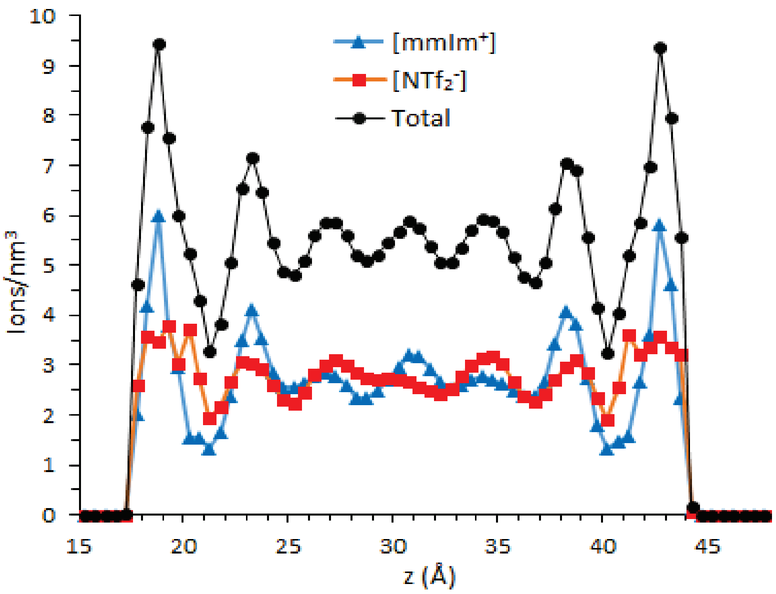

Figure IV-1. Ion number density profiles of the [mmIm$^+$] [NTf$_2^-$] IL confined between FeO surfaces with a pressure P = 500 MPa and a wall temperature T_{wall} = 350 K: [mmIm$^+$] cations (blue triangles), [NTf2$^-$] anions (red squares), and total density (black circles).

The organization of the simulated solid material can explain the absence of separated layers of cations or anions: even though the studied surfaces were polar, including both iron (2+) and oxygen (2-) ions, and so subject to Coulombic interactions, they remained globally uncharged and their first atomic layer in contact with the fluid was equally composed of alternating Fe and O ions. The distance between Fe and O ions in the solid being significantly smaller than the size of IL ions, the latter did not experience a net Coulombic attraction/repulsion and could mix freely near the surfaces. As mentioned in Chapter I, the formation of mixed anion-cation layers was also proven experimentally for ILs confined between neutral, non-polar graphitic or gold surfaces [22,27], and numerically between polar iron surfaces [28]. However, successive monolayers of separated cations and anions were distinctly observed next to negatively charged surfaces like mica [105,170].

The radial distribution function (Figure IV-2) describes how the density varies according to the distance between two particles. For 3D-domains, it is defined with the following expression:

$$g(r) = \frac{dn_{\alpha\beta}(r)}{4\pi r^2 \rho_{\alpha,N} dr}$$

where $dn_{\alpha\beta}(r)$ is the number of ions β between two spheres of radius r and $r + dr$ and with an ion α as the origin ; and $\rho_{\alpha,N} = n_{mol,\alpha}/V$ with $n_{mol,\alpha}$ the number of ions α in the system and V the volume. To ensure an accurate sampling of g(r), dr = 0.15 Å was taken. The results were obtained from an EMD simulation of the bulk [mmIm$^+$][NTf$_2^-$].

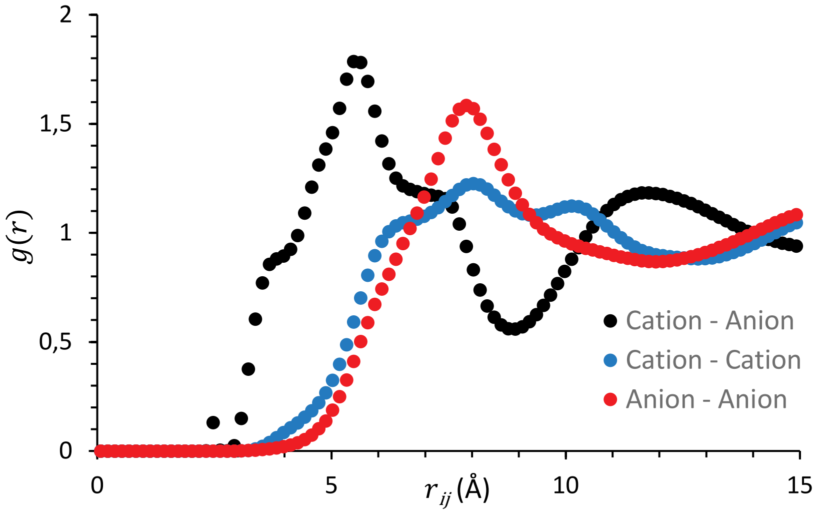

Figure IV-2. Radial distribution function of the ions in bulk fluid simulations.

The IL exhibits long-range spatial correlation (> 15 Å). It can first be noticed that the mean distance between ions of the same type is equivalent for cations and anions but is significantly higher than the mean distance between a cation and an anion. This is a consequence of the ions' partial charge that forces a 3D chessboard-like arrangement of the molecules to screen the electrostatic interaction forces.

Further, while the width of the anion density peak in bulk fluid is just about the same than the one in the first layer near the interface in Figure IV-1 (roughly 4 Å), the cation density peak in the same first layer is a lot more narrow than the bulk one. This denotes a specific orientation of the cation ions at the interface that can be detected through further analyses.

IV.1.2 Orientation at the interface

Referring back to Figure IV-1, the width of the density peaks should be correlated to the size of the molecules; nevertheless the width of the first [mmIm$^+$] and [NTf$_2^-$] density peaks was significantly different although the ions were of similar size. The organization of the molecules in the first layers nearby the surfaces provided an explanation, as it can be seen in Figure IV-3 where the orientation taken by the ions in that region is reported. Open circles on Figure IV-3a show the variation of α_{CR}, the average angle between the normal to the wall and the vectors normal to cation rings: a low α_{CR} value indicates that cations tend to be oriented parallel to the surface. Open circles on Figure IV-3b show the variation of α_{AS}, the average angle between the normal to the wall and the vectors $\overrightarrow{SS'}$ of the anions, S and S' being the two sulfur atoms. Similarly, black squares on Figure IV-3b display the variation vs. the distance from the wall of α_{AC}, the average angle between the normal to the solid-walls and the sum of the two vectors $\overrightarrow{SC}$ and $\overrightarrow{S'C'}$ of an anion, (S, S') and (C, C') being the couples of sulfur and carbon atoms, respectively. From the last two cases, the closer to 90° the value of α_{AS} and the closer to 0° the value of α_{AC} , the more the anions are oriented parallel to the surfaces with their CF$_3$ groups pointing toward the center of the confinement and with their oxygen atoms positioned near the surfaces.

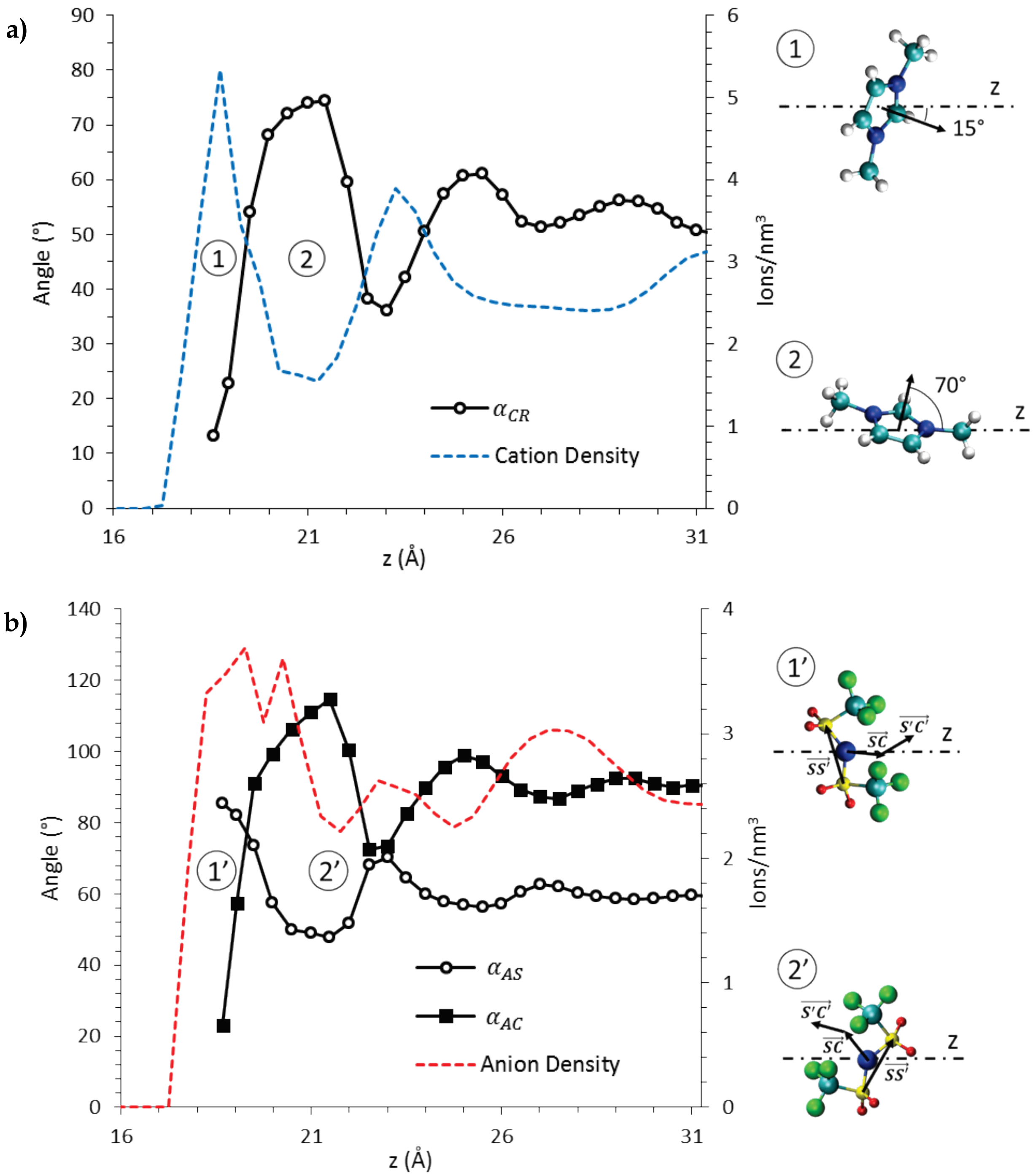

Figure IV-3. Ions orientation close to the wall under confinement, at 350 K and 500 MPa. a) Cations orientation with respect to the surface: variation of α_{CR}, the average angle between the normal to the surfaces (z axis) and the vector normal to cation rings. The cation density profile is superimposed for comparison (blue dashed line). b) Anions and CF_3 orientations with respect to the z axis represented by the variation of α_{AS} and α_{AC} angles (see text for detail). The anion density profile is superimposed for comparison (red dashed line).

Figure IV-3a and Figure IV-3b show that, at the solid-liquid interface, both cations and anions were oriented parallel to the walls. Nevertheless, the CF_3 groups of the anions in contact with the walls were distinctly oriented perpendicular to the walls, which explains the broader density peak of the anions. These results are in accordance with the observations of two others research groups who studied the same [mmIm$^+$][NTf$_2^-$] IL pairs confined between either non-charged gold surfaces [27] or negatively-charged mica surfaces [119]. [mmIm$^+$] cations were found to be oriented parallel to mica surfaces and [NTf$_2$-] anions oriented with their CF_3 group pointing toward the bulk. Other works carried out with different IL pairs presented comparable results regarding ions orientation. Atkin and Warr [22] and Mendonça *et al.* [28] observed the following trends on graphite and iron surfaces, respectively: the cation rings tended to align parallel to the surfaces while the anions alkyl chains were oriented toward the bulk. However in the same study but on mica surfaces, Atkin *et al.* observed a slightly different orientation of [emIm$^+$] cations with their alkyl chain pointing toward the bulk. The positive charge of the cations attracted by mica being located in the imidazolium ring, it was suggested that long alkyl-chains tend to get away from mica surfaces. Those tendencies were also confirmed through MD works [171] on confined [emIm$^+$][NTf$_2^-$].

Finally, combining our results with results from the literature, the layering structuration of the ions in confinement appears to strongly depend on the surface charge, with the formation of:

- separated cation and anion monolayers when confined between charged surfaces,
- mixed layers when confined between uncharged surfaces, either polar or nonpolar.

On the contrary, the orientation of IL ions is found to be less sensitive to the surface charge.

Overall, it results from the orientation of the ions that the anion oxygen and the cation hydrogen could chemically react with the substrate. The confining material must be chosen in consequence to avoid undesirable corrosion or to favor the formation of a tribofilm. Finally, to analyze the real effect of the fluid structuration on the fluid rheology and on the interfacial slip, shearing must be added to the system.

IV.2 Anomalous effective dynamics of the nano-contact

A shearing was imposed to the confined system by setting opposite velocities of $\pm U/2$ to the confining walls (Figure II-8). The temperature of the solid surfaces was kept constant and equal to 350 K while the temperature of the fluid was free to evolve. The pressure applied to the system was held to P_{conf} = 500 MPa and the shear velocity, U, was varied from 2 to 160 m/s, leading to apparent shear rates, $\dot{\gamma}_{app} = U/h$ (with h the contact thickness), ranging between ca. 8x10^8 and 6x10^{10} s^{-1}.

IV.2.1 Apparent response

Under shearing, the global film thickness increased slightly but regularly with the shear velocity up to ca. 7 % for the extreme case of U = 160 m/s. This feature will be explained later in the chapter. On the other hand, the structuration of the [mmIm$^+$][NTf$_2^-$] IL remained remarkably similar to the non-sheared one shown in Figure IV-1.

The Figure IV-4 represents the evolution of the global shear stress τ in the lubricated contact as a function of the shear velocity. The shear stress is invariable in the contact thickness as a steady state was achieved for each studied shearing velocity. Remarkably, it varied only slightly when the shear velocity spanned over almost 2 orders of magnitude, and reached a plateau at high shear velocities. The corresponding coefficient of friction (COF), equals to $/P_{conf}$, ranged between 0.1 and 0.2. This is consistent with experimental measurements on nanoconfined IL [128,172].

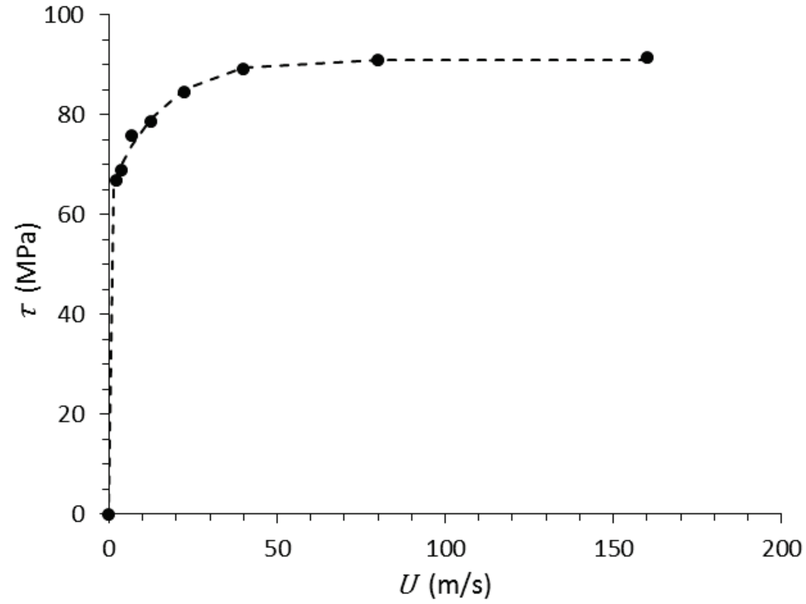

Figure IV-4. Evolution of the global shear stress τ in the lubricated contact as a function of the shear velocity, for an confining pressure of 500 MPa and a wall temperature of 350 K. The dashed line is a guide for the eyes.

As the control of friction is one major concern of the tribological community, the following investigation aims to uncorrelate the distinct mechanisms at stakes to estimate their individual influences.

IV.2.2 Shearing of the fluid

In order to explain the saturation of the shear stress τ with the shear velocity, the local IL response were investigated. Figure IV-5 represents a typical velocity profile, obtained for a shear velocity of U = 40 m/s at a confining pressure of 500 MPa and a wall temperature of 350 K.

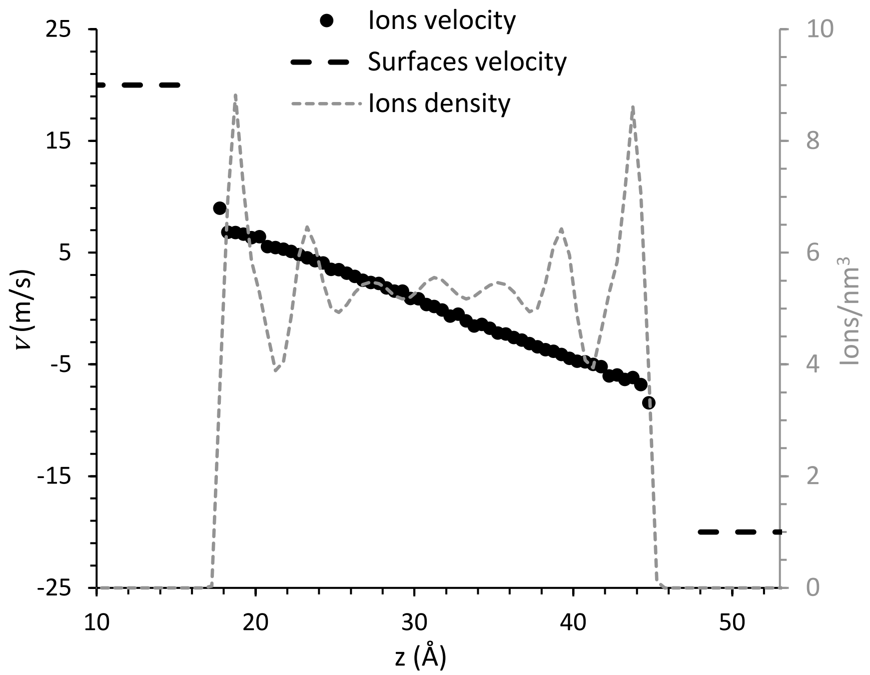

Figure IV-5. Typical velocity profile (for U = 40 m/s); the total density profile of the IL is superimposed for comparison.

Overall, the velocity profile was little affected by the IL layering close to the walls and remained linear throughout the whole fluid film. This homogeneity was not always ascertained with other fluids: a numerical study quantified the viscosity profiles of different Lennard-Jones fluids in confinement [173] and detected some viscosity reduction between well-formed layers near the surfaces. The strong interaction between the formed mixed layers in our study could explain the absence of similar variations.

The confined fluid then underwent a homogeneous effective shear rate, defined as $\dot{\gamma}_{eff} = -dv/dz$ in the linear region of the velocity profile. The rheology of the confined IL was characterized by computing the viscosity $\eta(\dot{\gamma}_{eff}) = \tau/\dot{\gamma}_{eff}$, as represented in Figure IV-6. As both the shear stress τ and the effective shear rate $\dot{\gamma}_{eff}$ are homogeneous across the lubricant film thickness, the viscosity is also constant.

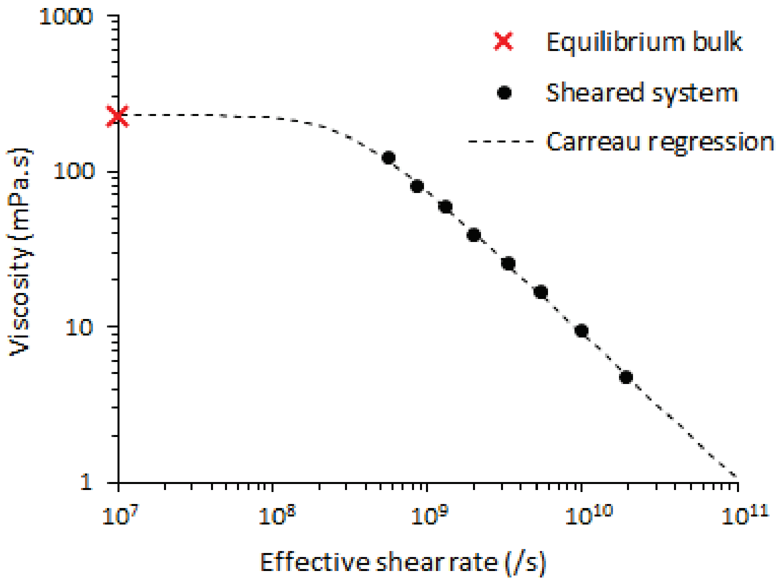

Figure IV-6. Viscosity of the confined IL as a function of the effective shear rate $\dot{\gamma}_{eff} = -dv/dz$ in the confined fluid. The dashed line is a Carreau regression of the viscosity. The red cross indicates the value of the Newtonian viscosity at 500 MPa and 350 K (Chapter III).

As for the bulk IL at ambient temperature and pressure, the evolution of the viscosity with the effective shear rate was well described by a Carreau law (Equation I.1), with a Newtonian viscosity η_N = 229 mPa.s, a relaxation time t_{rel} = 3.21 ns, and an exponent N = 0.038 (note that although the MD data did not reach the Newtonian plateau, the lowest effective shear rates simulated were sufficiently close to it so as to estimate the Newtonian viscosity with good accuracy). Remarkably, the Newtonian viscosity obtained from the Carreau fit matched the value obtained independently from equilibrium bulk simulations at 500 MPa and 350 K, using a Green-Kubo formula: 225 ± 17 mPa.s. However, the exponent N was significantly larger for the confined IL (N = 0.038, at a pressure of 500 MPa and a wall temperature of 350 K) than in bulk (N = 0.257, at a pressure of 500 MPa and a fluid temperature of 350 K, cf. Chapter III).

IV.2.3 Wall slip

Remarkably, the velocity profile in Figure IV-5 also revealed the presence of a velocity jump at the interfaces between the IL and the oxide surfaces, a phenomenon referred to as liquid/solid slip [87]. Hydrodynamic slip is described with the partial-slip boundary condition, which links the slip velocity v_{slip} (i.e. the velocity jump at the liquid/solid interface) to the shear rate in the liquid at the solid surface. In a simple shear flow as considered here, the slip velocity is directly related to the effective shear rate in the liquid as follows:

$$v_{slip} = L_s \times \dot{\gamma}_{eff} \qquad \text{(IV. 1)}$$

where L_s is the so-called slip length, which can be interpreted as the depth inside the wall where the linear extrapolation of the fluid velocity profile reaches the wall velocity [87]. For a given shear velocity, liquid/solid slip reduces the effective shear rate inside the IL, which can be expressed as:

$$\dot{\gamma}_{eff} = U/(h + 2L_s) = \dot{\gamma}_{app}/(1 + 2L_s/h) \tag{IV.2}$$

where $\dot{\gamma}_{app} = U/h$ with U the shearing velocity and h the contact thickness. Liquid/solid slip has therefore a significant influence on the effective shear rate when the slip length compares with the lubricating film width, as it was the case here.

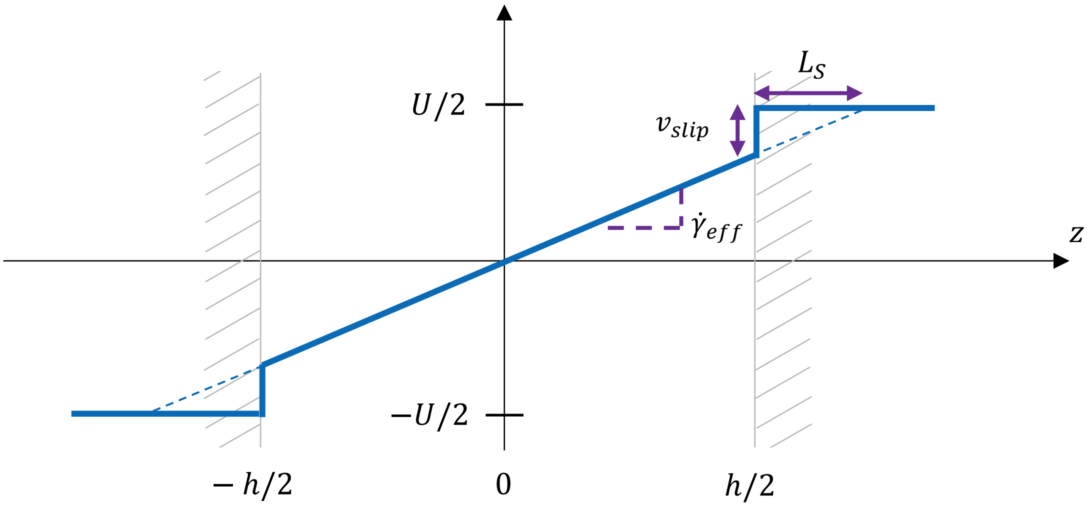

Figure IV-7. Schematic definition of the slip length.

The characteristic velocity profile is drawn in blue.

To offer some insight into the origin of slip in the present system, it should be emphasized that the slip length, though it has a simple kinematic interpretation, is not a fundamental property of the liquid/solid interface. Indeed, the partial slip boundary condition (Equation IV.2) stems physically from the identification of the bulk viscous shear stress:

$$\tau = \eta \times \dot{\gamma}_{eff} \tag{IV.3}$$

with an interfacial liquid/solid friction stress :

$$\tau = \lambda \times v_{slip} \tag{IV.4}$$

where λ is the liquid/solid friction coefficient [87,174,175]. Combining Equation IV.3 and Equation IV.4, one obtains the partial slip boundary condition of Equation IV.1, where the slip length is given by:

$$L_s = \eta/\lambda \tag{IV.5}$$

The slip length is accordingly a combination of the bulk liquid viscosity η and the interfacial friction coefficient λ. Figure IV-8 shows the evolution of the slip length L_s as a function of the effective shear rate. It increases significantly from a few angstroms at low velocities and tend to saturate at higher velocities to roughly 30 Å.

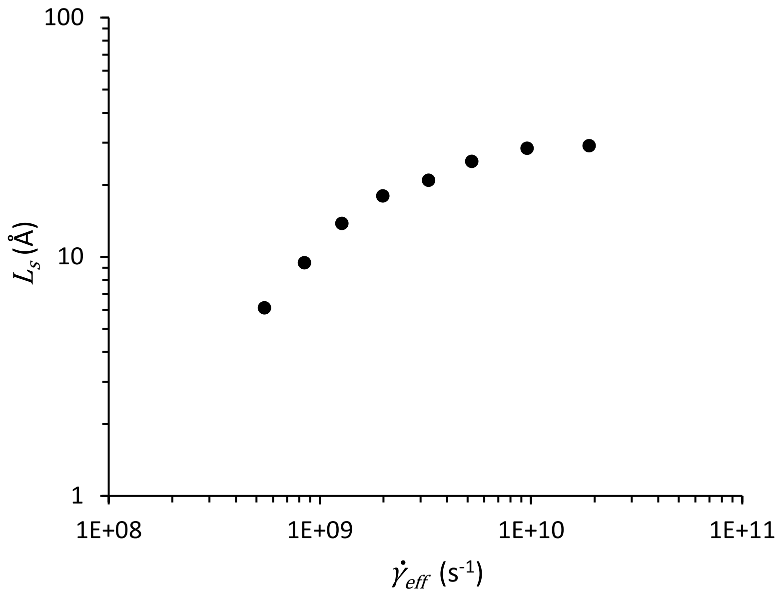

Figure IV-8. Effective shear rate dependence of the slip length $L_s = v_{slip}/\dot{\gamma}_{eff}$

So far, no hydrodynamic slip has been observed experimentally with sheared ionic liquids. However, previous studies on alkanes confined between various non-polar surfaces identified wall-slip occurrence and its strong relationship with the surface composition and orientation [83]. Depending on the atom nature of the solid body in contact with the fluid, the commensurability and the corrugation forces at the interface can profoundly change, and directly influence the presence and intensity of wall slip [83,174,175]. Oxygen and iron atoms (both present at the interface of the IL/oxide system of the current study) present Lennard-Jones energy coefficients [150] favoring wall slip in the absence of Coulombic interactions [83]. Nevertheless, when considering ionic liquids, Coulombic interactions are predominant at the interface and should modify the corrugation forces opposed to slip. Other MD works simulating different confined ILs encountered little to no slip response to shearing with metallic (polar) or silica (charged) surfaces [131,176].

In order to understand the origin of slip in the current study, it became essential to characterize the liquid/solid interactions. For simple liquids at low pressure and small shear rate (i.e. in the linear response regime), a large experimental and numerical effort over the last 20 years has highlighted the existence of a quasi-universal relationship between the slip length and the wetting properties of the liquid/solid couple [173,177], although some recent works have shown that the wetting properties alone can fail to predict the slip length [178,179]. This quasi-universal relationship predicts that slippage is favored on non-wetting substrates, and that it should not occur for contact angles below ca. 80°. Therefore, the wetting properties of the IL/FeO couple were measured in an independent simulation of an IL droplet (40 IL ion pairs) on a FeO substrate at 350 K and a rather wetting behavior was found, with a contact angle of 43°. Hence, the relationship between wetting and slippage fails for the system under consideration. On Figure IV-9 is plotted the liquid/solid friction coefficient λ as a function of the effective shear rate.

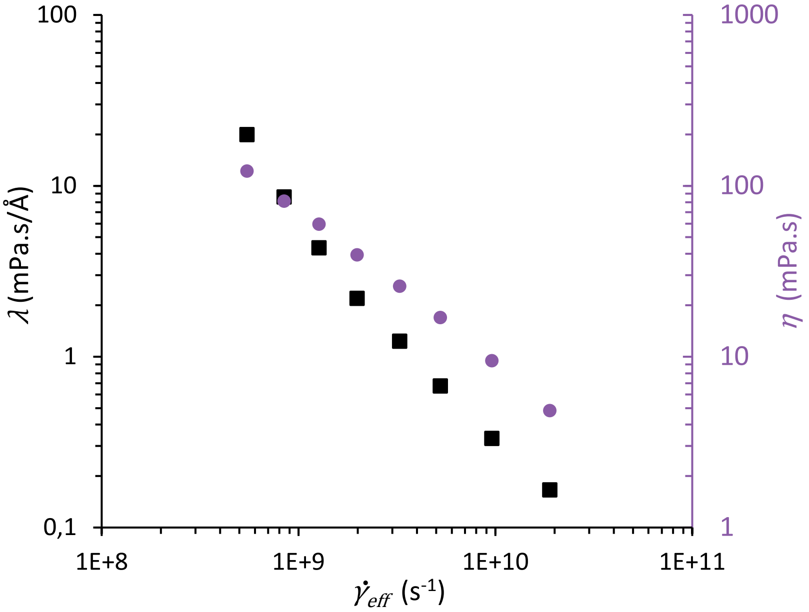

Figure IV-9. Variation of the liquid/solid friction coefficient $\lambda = \tau/v_{slip}$ at the IL/FeO interface in relation with the effective shear rate. By way of comparison, the viscosity is also reported on a secondary axis.

The inaptitude of the wetting properties to explain the observed wall slip suggests that the presence of slip in our study was due to the particular working conditions of high pressure and high shear rates typical of a lubricated contact. Specifically, the combination of two factors can explain the presence of significant slip. Firstly, the important viscosity resulting from the severe confinement of the system (up to 225mPa.s at P = 500 MPa) tends to increase the slip length as the two values are directly proportional (Equation IV.5). Secondly, the comparison of the evolution with the shear rate of both the bulk viscosity and the fluid/solid friction coefficient (see Figure IV-9) reveals that the first decreases more slowly than the second at the lowest studied shear rates. This results in an increase of the slip length with the shear rate (Equation IV.5). In other words, the strong viscosity of the fluid has a higher influence on slip than the friction of the fluid/solid interface.

Another interesting feature concerns the fact that the slip length saturated in the large shear rate limit (Figure IV-8). This contrasts with previous numerical results on simple fluids obtained in less severe thermodynamic conditions, where the slip length has been shown to diverge [180], although other works also observed a saturation when using thermostated walls [90,181]. In the high shear rate limit λ scales exactly as the fluid viscosity (cf. Figure IV-9). Consequently, the slip length, which is the ratio between the two quantities, reached a constant value. In other words, the vanishing liquid/solid friction at high shear rates did not result in a diverging slip length because it was exactly compensated by the vanishing fluid viscosity. To understand the cause behind this behavior, it is thus necessary to have a look at the origin of this anomalous drop of the viscosity.

IV.3 The complex influence of the temperature

The following analysis aims to explain the anomalous rheology observed in the contact. This involves a focus on the thermal behavior of the system as it directly impacts the lubricant viscosity. Therefore, the link between the viscosity, the thermal behavior and the interfacial thermal resistance is first explored. In a second part, an analytical expression is proposed to predict the thermal behavior occurring in a confined system.

IV.3.1 Interfacial thermal resistance

To understand the viscosity variation, a look at the thermal behavior of the contact is crucial. Figure IV-10 displays a typical temperature profile (for U = 40 m/s). As the shear stress induces a viscous strain of the fluid, the latter heats up with its strain:

$$Q = \eta . \dot{\gamma}_{eff}{}^{2} \tag{IV.6}$$

where Q is the generated energy per unit volume of the IL.

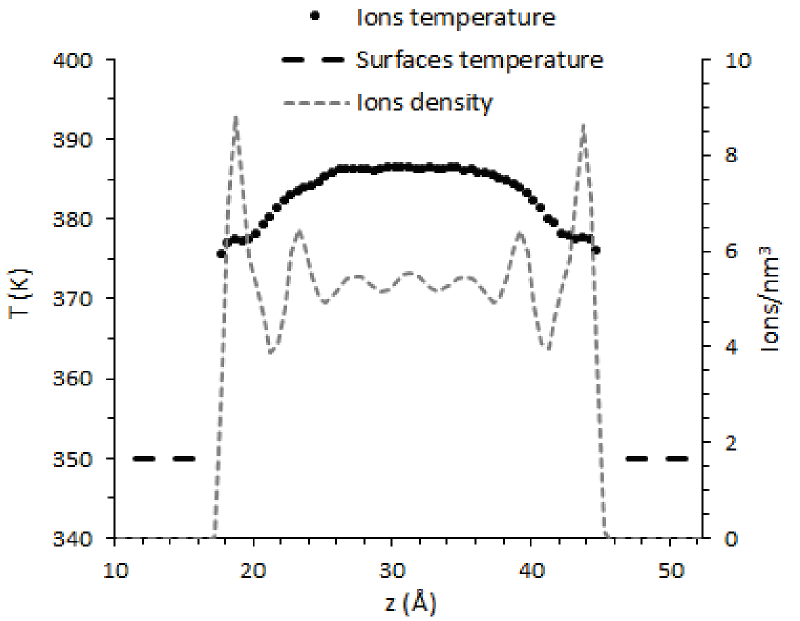

Figure IV-10. Typical temperature profile of the sheared IL, for a shear velocity U = 40 m/s.

Only the thermostated surfaces have a frontier with the fluid. Hence, they dissipate the transferred energy so a steady state can be reached. It is noteworthy that at the liquid/solid interface a thermal slip operates simultaneously the velocity slip, this can be associated to a non-null thermal resistance of the interface.

Figure IV-11 represents the evolution of the interface thermal resistance:

$$R_{th} = \Delta T / \phi_q \tag{IV.7}$$

with ΔT the temperature jump at the liquid/solid interface and ϕ_q the heat flux through the interface.

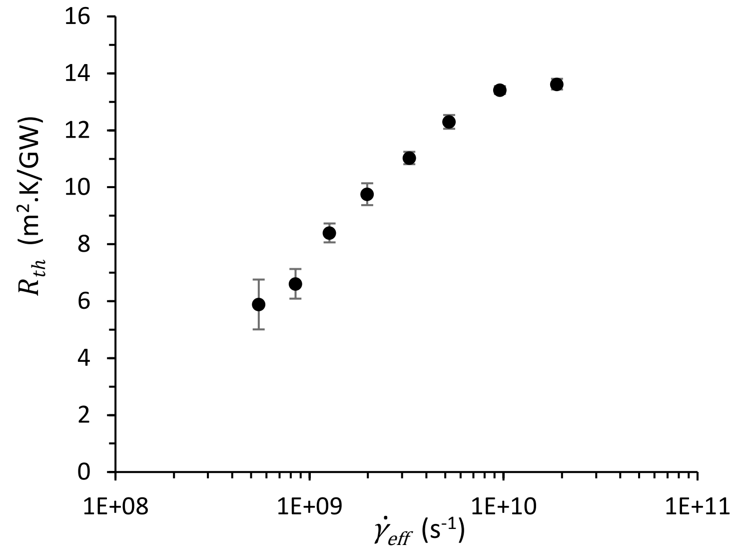

Figure IV-11. Evolution of the thermal resistance of the fluid/solid interface with the effective shear rate.

The variation of the resistance appeared to be comparable to the evolution of the slip length (Figure IV-8). This is consistent with previous observations of a correlation between hydrodynamic and thermal slips [93], and could result from shared underlying mechanisms occurring at the molecular level.

As a consequence of the limited heat transfer between the lubricant and the walls, the average temperature of the confined fluid increased progressively and significantly with the effective shear rate, as shown in Figure IV-12.

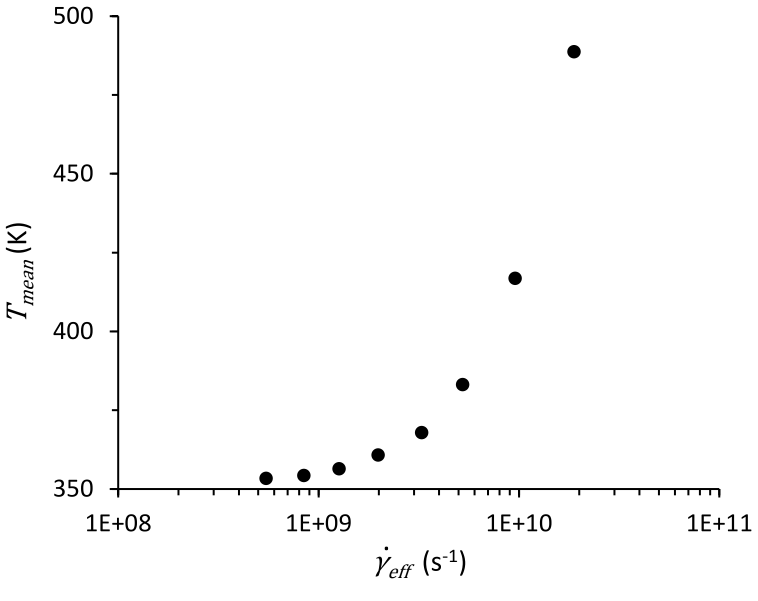

Figure IV-12. Evolution of the average temperature of the confined IL with the effective shear rate.

This temperature rise is the key to the specific behavior of the confined IL. In particular, it could explain the observed increase of the lubricant film thickness with the shear velocity, through thermal expansion of the fluid. More importantly, the increase of fluid temperature is expected to amplify the decrease of viscosity with the shear rate, what explains the larger exponent N in the Carreau law measured for the confined fluid, as compared to the bulk one Figure III-1. One can note here that the Carreau law for the confined fluid is therefore an effective one, hiding a complex mechanism involving the coupling between the variations of the fluid temperature and the shear thinning, both leaded by the shear rate.

To evaluate the contribution of both effects, the evolution of the Newtonian viscosity with the temperature is compared to the variation of the viscosity in nanoconfined simulations. Through data of section III.2, an arbitrary analytical expression of the Newtonian viscosity variation with the temperature was established to predict the viscosity variation at P = 500 MPa. The Newtonian viscosity corresponding to the mean temperature of each nanoconfined simulated configurations is computed and plotted in Figure IV-13. As in nanoconfinements, the viscosity variation depends on the effect of shear thinning and temperature elevation, it can be deduced from the evolution of the Newtonian viscosity that the effect of the shear thinning is prominent at moderate shear rates ($4.10^8\ \mathrm{s}^{-1} < \dot{\gamma}_{eff} < 4.10^9\ \mathrm{s}^{-1}$) whereas the effect of the temperature is prominent at high shear rates ($\dot{\gamma}_{eff} > 4.10^9\ \mathrm{s}^{-1}$).

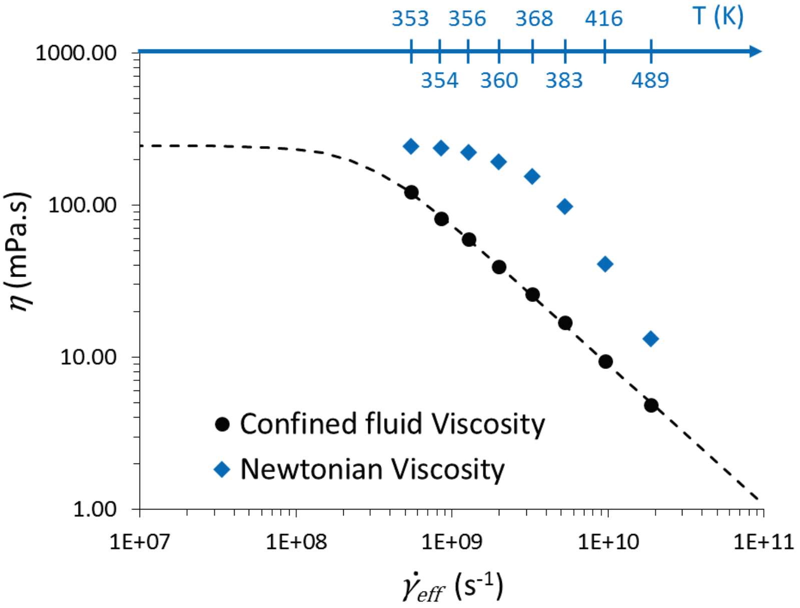

Figure IV-13. Comparison of the operating viscosities resulting from nanoconfined simulations (black circles) with the bulk Newtonian viscosities at the corresponding temperatures (blue diamonds).

IV.3.2 *Toward a control of the heating in the lubricated contact*

Mastering the whole heating process could allow to enhance the tribological performances of a lubricated contact through a better design of the surface and fluid involved. Hence, an analytic description of the heating process in depicted in the following.

As the fluid exhibits a homogenous viscosity across the film thickness, the velocity profile is linear (Figure IV-6) and so the energy generated by the fluid viscous strain is constant. The subsequent heat flux is obtained by integrating the work of the shearing per unit area over z:

$$\phi_q(z) = \int_0^z \frac{1}{2}\eta\dot{\gamma}_{eff}{}^2 dz = \frac{\eta\dot{\gamma}_{eff}{}^2 z}{2} \qquad \text{(IV.8)}$$

For simplification purpose, the frame origin ($z = 0$) is taken at the film thickness center so that $\phi_q(z_0) = 0$. According to Fourier's law, the heat flux is also defined by the temperature gradient:

$$\phi_q = -k\frac{\partial T}{\partial z} \qquad \text{(IV.9)}$$

With k the thermal conductance of the fluid. As a consequence:

$$\frac{\partial T}{\partial z} = -\frac{\eta\dot{\gamma}_{eff}{}^2 z}{2k} \qquad \text{(IV.10)}$$

$$T(z) = \frac{\eta\dot{\gamma}_{eff}{}^2}{4k}(A - z^2) + T_{wall} \qquad \text{(IV.11)}$$

With A a constant to be determined. It is noteworthy that the evolution of the temperature within the fluid can be fitted with a parabola, this is in accordance with temperature profiles specific to the nanoconfinements as the one plotted Figure IV-10.

The thermal jump at the liquid/solid interface can also be described analytically. To do so, Barrat and Chiaruttini used the Kapitza length l_k to characterize its prominence [93]. As illustrated in Figure IV-14, this parameter is the ratio between two specific values of the interface: the temperature jump ΔT and the gradient temperature in the fluid $\frac{\partial T}{\partial z}$.

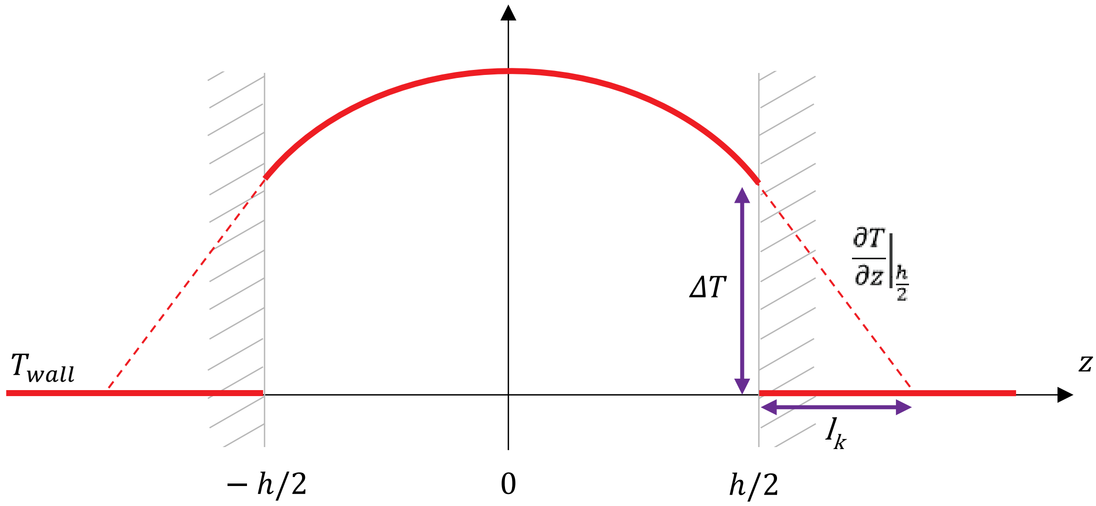

Figure IV-14. Schematic definition of the Kapitza length l_k.
The characteristic temperature profile was drawn in red.

Given that $\phi_q = R_{th}\Delta T$, and according to the Equation IV.9, the Kapitza length can also be defined as the ratio between both fluid and interface conductivities: $l_k = R_{th}k = k/\Lambda$ with $\Lambda = 1/R_{th}$ the interface conductance. Considering the fluid temperature at the interface, Equation IV.11 gives the following:

$$\Delta T = T\left(\frac{h}{2}\right) - T_{wall} = \frac{\eta \dot{\gamma}_{eff}{}^{2}}{4k}\left(A - \left(\frac{h}{2}\right)^{2}\right) = -\, l_k \frac{\partial T}{\partial z}\bigg|_{\frac{h}{2}} = \frac{\eta \dot{\gamma}_{eff}{}^{2} h l_k}{4k} \qquad \text{(IV.12)}$$

And therefore:

$$A = h\left(l_k + \frac{h}{4}\right) \qquad \text{(IV.13)}$$

$$T(z) = \frac{\eta \dot{\gamma}_{eff}{}^{2}}{4k}\left(h\left(l_k + \frac{h}{4}\right) - z^2\right) + T_{wall} \qquad \text{(IV.14)}$$

Through this explicit expression of the fluid temperature, the thermal behavior of the confinement can be predicted providing that some characteristical values of the fluid and surface properties or known. In particular two distinct regimes are identified.

For $h \gg l_k$ (i.e. large thickness or good interface conductance):

$$T(z) \approx \frac{\eta \dot{\gamma}_{eff}{}^{2}}{4k}\left(\frac{h^2}{4} - z^2\right) + T_{wall} \qquad \text{(IV.15)}$$

In such a configuration, the temperature rise is mostly fluid-dependent and varies significantly in the system thickness. As a consequence the viscosity is as well quite heterogeneous along *z* with a minimum at the center of the film thickness causing the shear to be mainly absorbed around this location. Besides, in this configuration, if the fluid viscosity and the wall temperature are known, the fluid conductivity and the film thickness only are required to predict the thermal behavior.

For $h \ll l_k$ (i.e. nanoconfinements or low interface conductance):

$$T = \frac{\eta \dot{\gamma}_{eff}{}^{2}}{4k} h l_k + T_{wall} = \frac{\eta \dot{\gamma}_{eff}{}^{2} h}{4\Lambda} + T_{wall} \qquad \text{(IV.16)}$$

In that case, the temperature is homogeneous in the lubricant film as well as the viscosity. A special consideration should be given to the lubricant choice as for low interface conductance at high shearing velocities, the temperature can rise to the point it accelerates its oxidation. However, the Kapitza length l_k is generally of the same order of magnitude than the slip length L_s [93] so the shear can be mostly absorbed at the liquid/solid interface, limiting the stress of the fluid. More features of this aspect are detailed in the following chapter for different surface natures. Finally, in this case, the evaluation of the interfacial conductance Λ and of the film thickness h are sufficient to predict the thermal behavior.

IV.4 Outcome and limiting shear stress

Now that the interfacial response of the confined IL to shearing were investigated in detail, the saturation of the global shear stress (Figure IV-4) can be related to the particular rheology of the confined IL, measured inside the lubricated contact. Due to this particular rheology, it is noteworthy that the presence of liquid/solid slip has no significant influence on the plateau value of the global shear stress.

Indeed, the global shear stress in the lubricated contact can be expressed as the viscous shear stress inside the fluid: $\tau = \eta_{eff} \times \dot{\gamma}_{eff}$. As previously depicted, the viscosity of the confined IL followed a Carreau law (Equation I.1), with an exponent N = 0.038. Beyond the Newtonian plateau (i.e. when $\dot{\gamma}_{eff} \gg 1/t_{rel}$), the Carreau law simplifies to a simple power law:

$$\eta_{(\dot{\gamma}_{eff})} \sim \eta_N \times \left(\dot{\gamma}_{eff} \times t_{rel}\right)^{N-1} \tag{IV.17}$$

The shear stress in the IL then becomes proportional to:

$$\eta_N \times t_{rel}{}^{N-1} \times \dot{\gamma}_{eff}{}^{N} \tag{IV.18}$$

For an exponent of precisely 0, τ becomes independent of the effective shear rate, and reaches a plateau at a value: $\tau_{max} \sim \eta_N / t_{rel}$. Remarkably, in that specific situation, the reduction of effective shear rate due to liquid/solid slip would therefore not help to reduce the global shear stress. In the simulated cases, N is very low but as the slip is also remarkably high, the latter contributes to reach the saturation of the shear stress at a lower shearing velocity than if the shear thinning were acting alone.

Beyond the interest of previous results for the chemical physics community, the response of the system to shearing gives some insight on the choice of using ILs as lubricants in steel-steel contacts under severe working conditions. As the shear rate rises, this work revealed that the presence of both an anomalous effective shear thinning and a velocity wall slip lead to a limitation of the shear stress and thus of the global friction. It is important to note that this friction limitation is accompanied by a significant temperature increase. In that regard, the high thermal stability of ILs (and especially of the [mmIm$^+$][NTf$_2^-$] compound) makes them particularly suitable lubricants compared with conventional ones.

In Appendix C the case of the ultra-confined IL (contact thickness under one nanometer) were also briefly studied to foresee the response of the friction to almost solid/solid contacts. In this configuration, the role of the fluid structuration becomes determining. It is noticed that the friction reaches an optimal minimum value when only two well-formed layers of IL remain between the shearing surfaces.

Now that the incidence of shearing and of the coupled effect of slip and temperature elevation on viscosity and friction were examine in detail, the next chapter aims to apprehend the influence of the surface nature on the nanoscale rheology and more globally on the lubrication performances of the contact. In particular, despite the wetting properties of the FeO, significant wall slip was observed in the latter simulation. The question then arise on the prominence of slip with less adhesive materials.

Chapter V: From rough to very low friction surfaces

As described in Chapter I, the thickness of industrial lubricated contacts has gradually decreased during the last decades, down to the size of a few tens of nanometers and even locally to a few molecular layers at the junction of asperities [32]. It was shown in Chapter IV that at this scale, the interfacial friction between the fluid lubricant and the solid surface at the origin of velocity wall slip, is a key component of the dynamics of such systems. In particular, Savio *et al.* [29] illustrated that if the slip is different at each surface in a contact controlled by an elasto-hydrodynamic (EHD) regime, the film thickness is greatly impacted and can either increases and prevents solid-solid contact or drops toward apparition of local film breakdown that would damage the system. So far, iron oxide were considered as the more representative component of the surface of classic steel-steel lubricated systems [149]. However, compared to non-polar surfaces, this oxide is subject to significant fluid friction [83]. As a consequence, all the shearing motion is absorbed by the fluid, bringing about more viscous friction in EHD or very thin film (VTF) regimes. With this in mind, a limitation of friction losses is sought with the use of particularly smooth surfaces. Among the promising materials for tribological applications, the non-polar DLC (diamond like carbon) coatings exhibit very low friction and high wear resistance [30,31] and might present low wetting properties [182].

To understand the ruling physics behind novel lubricated systems, the present study aims to characterize the influence of the surface nature on the shearing response. The [mmIm$^+$][NTf$_2^-$] was nanoconfined between five different materials (including four DLC alike surfaces) and sheared over a large velocity range.

V.1 Introduction to DLC coatings

DLC coatings are amorphous carbon materials essentially made of sp^3 and sp^2 hybridized carbons. They are more or less hydrogenated depending on the production method and on the desired properties of the coatings. Figure V-1 shows the family of DLCs depending on the concentration of each component (carbon sp^2, carbon sp^3 or H).

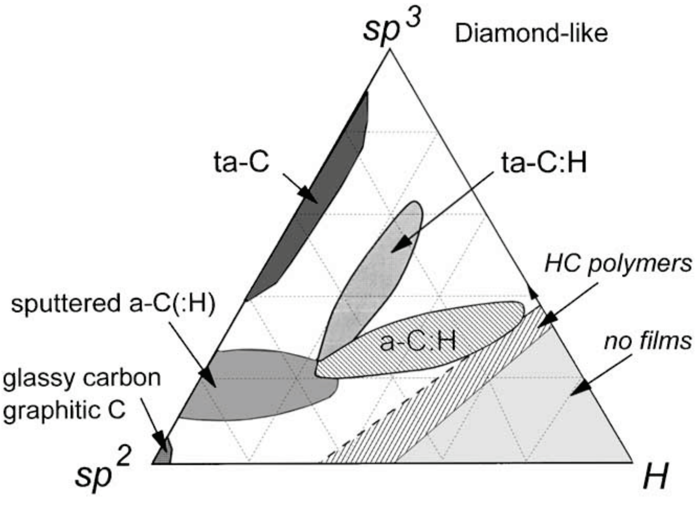

Figure V-1. Ternary phase diagram of bonding in amorphous carbon-hydrogen alloys [31]

The more sp^3 bonds and the less hydrogenated, the harder and more wear resistant the coating will be [31]. The ideal fully sp^3-hybridised and non-hydrogenated allotrope of carbon is diamond, hence the name of the coating. On the other hand, the fully sp^2-hybridised and non-hydrogenated allotrope of carbon is graphite. Between the two, when the DLC is dense and structured (more than 40 % sp^3-hybridised carbon [153]), it is referred to as tetrahedral amorphous carbon (ta-C). It is the best quality coating done in the industry but also the most expensive. A less dense carbon material is simply named amorphous carbon (a-C). It is noteworthy that a-C is formed at the interface of two shearing ta-c surfaces when direct contact occurs [153]. In today industries, hydrogenated DLC (a-C:H or ta-c:H) are more widely used as they are cheaper to produce and present satisfactory tribological performances. However, with the enhancement of coatings deposition technics, DLC are less and less hydrogenated.

Further to showing good performances with some classic lubricated systems, DLC coatings were experimentally investigated within IL-lubricated contacts: less friction and wear were noticed using IL lubricants rather than standard ones (PAO, MAC, Zdol or PFPE) [183–185]. The explanation partially lies in the formation of a protective tribofilm caused by the reaction of the IL anion with the DLC film. With IL-lubricated contacts, experimental studies also confirmed the better performances of DLC-steel surfaces compared to steel-steel surfaces [186,187] or even to other coatings depending on the considered IL [188]. Several works were also conducted using MD simulations to study some aspects of the lubrication capability or of the IL mobility when confined between DLC or graphite materials [118,189–192]. Pushing forward, Mendonça and coworkers characterized the friction of a nanoconfined IL between two amorphous carbon surfaces for different normal loads and speeds [192]. While the friction force evolves linearly with the normal load, it increases more slowly with the shearing velocity (for any fixed value of the normal load, the ratio of the shear stress and the shearing velocity decreases significantly with the velocity). Either the IL viscosity decreases with increasing velocity, either an important hydrodynamic slip takes place at the liquid/solid interface. Some investigations of the {DLC+IL} systems are still needed to optimize them. A comparative study of the involved mechanisms for different surfaces is necessary to quantify the improvements.

To study the lubrication mechanisms of the DLC coatings in EHD and VTF regime, MD simulations are run with the carbon-based materials introduced in Chapter II as confining and shearing surfaces. Hence, the friction behavior associated to diamond, graphite and two a-C surfaces with different roughness are evaluated and compared to the one displayed with the iron oxide surfaces.

V.2 Surface-driven friction and rheology

V.2.1 Coefficient of friction

Focus was first made on the global coefficient of friction (COF) of the lubricated contact. The simulations bring out large disparities of the value according to the surfaces nature (Figure V-2).

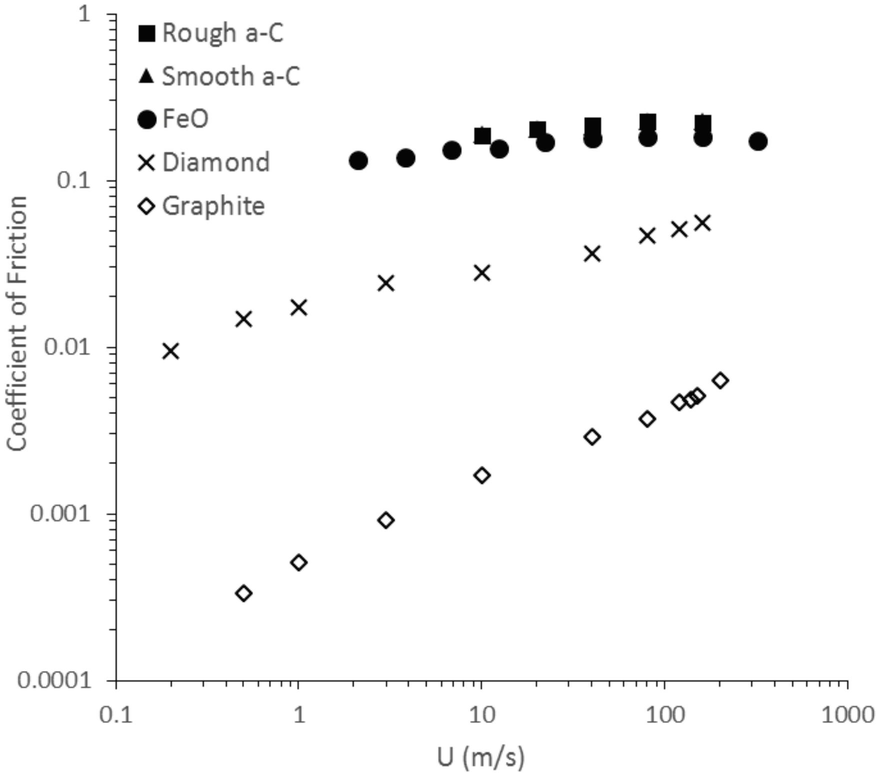

Figure V-2. Coefficient of friction of the sheared system with a confining pressure of 500 MPa between five different surfaces: iron oxide, diamond, graphite and two a-C coatings

The coefficient is extremely low for graphite surfaces: from 0.00033 (at 0.5 m/s) to 0.0063 (at 160 m/s). It is also low with perfect diamond structures: from 0.0094 (at 0.2 m/s) to 0.056 (at 160 m/s). On the other hand, the COF is remarkably close for the two amorphous carbon surfaces and the iron oxide one. Overall, high differences are obtained with the same fluid as lubricant, and comparable operating conditions, making unquestionable the major role of surfaces in the lubrication at this scale.

V.2.2 *Interfacial velocity slip*

Focusing on the liquid/solid interface, high velocity slips v_{slip} of the ionic liquid on the surfaces were detected. The order of magnitude of those slips varies significantly with the surface nature and could explain the large disparities of the COF (Figure V-3).

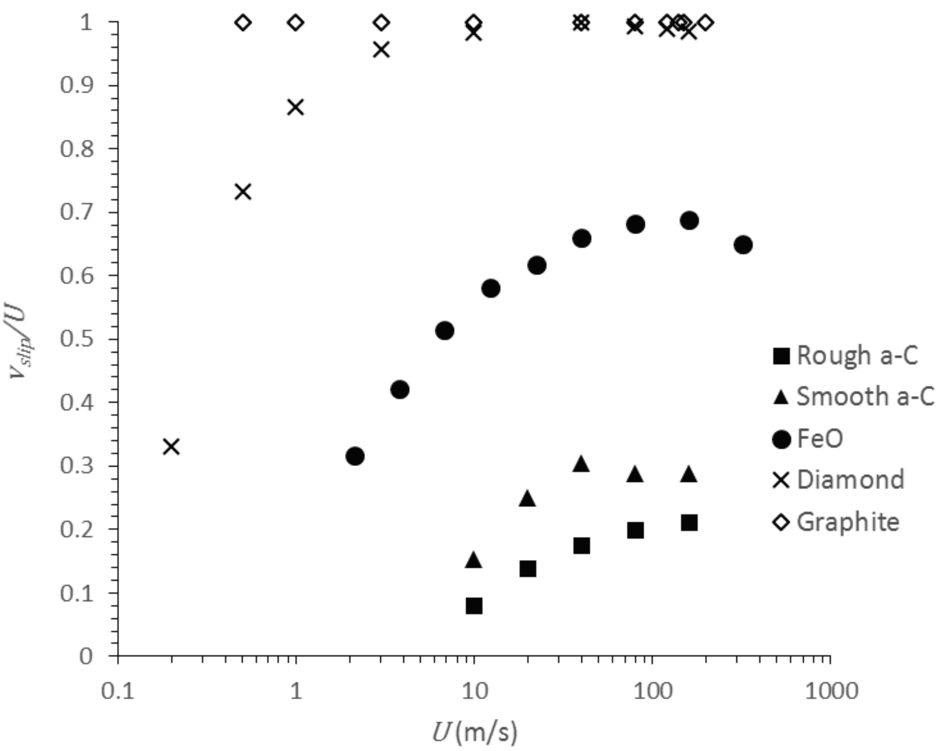

Figure V-3. Ratio of the interfacial velocity slip on the imposed shearing velocity as a fonction of the imposed shearing velocity.

Distinct regimes take place depending on the shearing surfaces. Graphite brings a surface-controlled regime with a complete absorption of the shearing at the liquid/solid interface and no shear of the fluid. Close to this configuration, diamond induces an uptake of the shearing by the interfaces starting from 57 % at low speed (0.2 m/s) to more than 90 % at higher shear rates (from 3 m/s). Interfacial slip with iron oxide follows the same trend but in a more assorted regime: from 16 % of absorption of the shear at a 2 m/s shearing velocity to a maximum of 62% at higher velocity. While similar COFs are featured by a-C and FeO surfaces, the slip is lower for both DLC surfaces than for the iron oxide one. As explained in detailed in the following section V.3.2, the slight difference of the film thickness between the simulations is at the origin of this discrepancy. It results in a mainly fluid-sheared regime with amorphous carbon surfaces.

The last cases (FeO and a-C surfaces) also reveal a saturation of the wall slip over a given shearing velocity. This contrasts with previous numerical results on simple fluids obtained in less severe thermodynamic conditions, where the slip length has been shown to diverge [180]. Nevertheless, other studies also observed saturation when using thermostated walls [90,181]. To understand both singularities of slip dissimilarity and slip saturation, further analysis of the interface behavior are needed.

V.2.3 *Interfacial Fluid friction coefficient*

To provide insight into the origin of slip, the fluid friction coefficient λ was computed and is plotted in Figure V-4 as a function of the interfacial velocity slip v_{slip}.

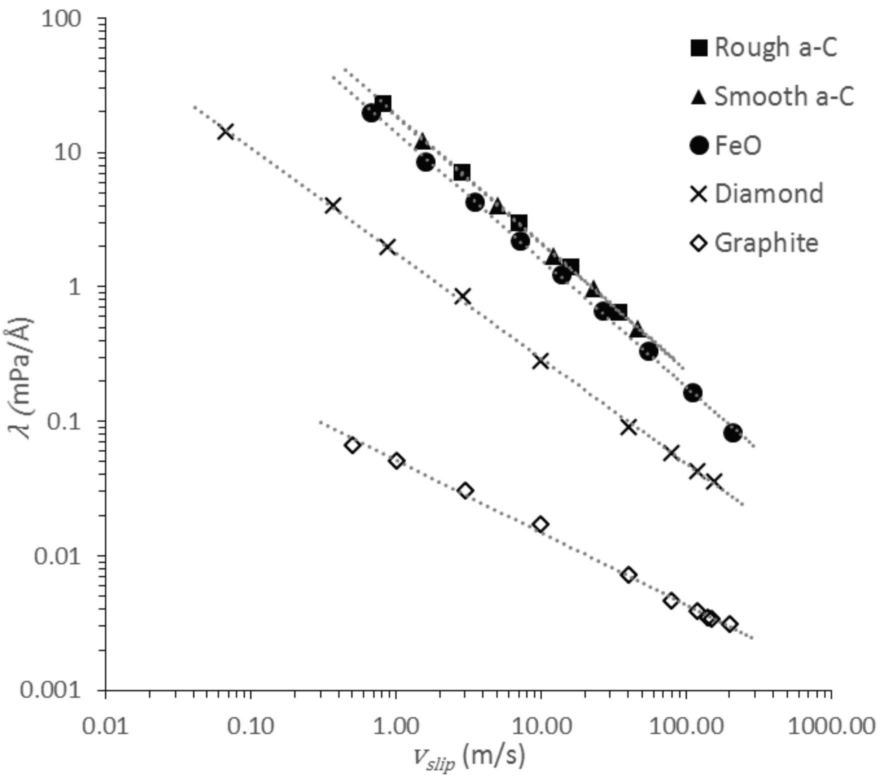

Figure V-4. Fluid friction versus interfacial slip velocity of five different surfaces: iron oxide, diamond, graphite and two DLC coatings.

The evolution of the coefficient λ with the velocity slip at the liquid/solid interface v_{slip} is comparable for every surfaces. Ideal surface of graphite (flat, non-polar) has the lowest fluid friction while the polar (but smooth) surface of iron oxide and the rough (but non-polar) surfaces of a-C give rise to more interfacial friction. Each variations can be fitted by a negative power law whose exponents specific to each surfaces are listed in Table V-1. It is noteworthy that the higher the friction, the more important the exponent. As a consequence, the discrepancy between the low friction surface (graphite) and high friction ones (FeO, a-C) is slightly reduced at high v_{slip}.

Graphite	Diamond	FeO	Smoothest a-C	Roughest a-C
-0.535	-0.781	-0.944	-0.944	-0.947

Table V-1. Power law exponent of the evolution of the fluid friction coefficient λ with the interfacial velocity slip v_{slip}.

Over the past 20 years, many MD studies claimed the existence of a quasi-universal relationship between the previously introduced slip length (Equation IV.1) and the wetting properties of the liquid/solid couple [173,177], although some recent studies have shown that the wetting properties alone can fail to predict the slip length [178,179]. In the present study, comparable wetting properties are expected for all the carbon based surfaces as they are composed of the same elements, and yet they display extremely different coefficient λ (up to 2+ orders of magnitude).

The global COF (Figure V-2), is logically linked to the fluid friction: the lower the λ, the lower the COF, and to equivalent values of λ for the iron oxide and a-C surfaces correspond equal values of COF. Nonetheless, the variation of the fluid friction does not explain the saturation of the slip (Figure V-3). An overall picture of the mechanisms at the origin the uptake of the shearing motion according to the confining surfaces would bring new answers.

V.2.4 *Slip length*

As the slip length is the ratio between the interfacial velocity slip and the effective shear rate through the fluid, it is a relevant indicator to compare the velocity accommodation at the interface and in the fluid. It is related to the ${v_{slip}}/{U}$ ratio by:

$$\frac{v_{slip}}{U} = \frac{1}{2 + {h}/{L_s}} \qquad (V.1)$$

with h the lubricant film thickness. According to this expression, the shearing is assimilated at the interface (i.e. $v_{slip} \approx U$) when $L_s \gg h$ and in return, the fluid uptakes the shearing when $L_s \ll h$. The slip length is likewise linked to the fluid friction and the fluid viscosity (see Equation IV.5). In Figure V-5 the slip length variations with the shearing velocity is plotted for the five studied surfaces.

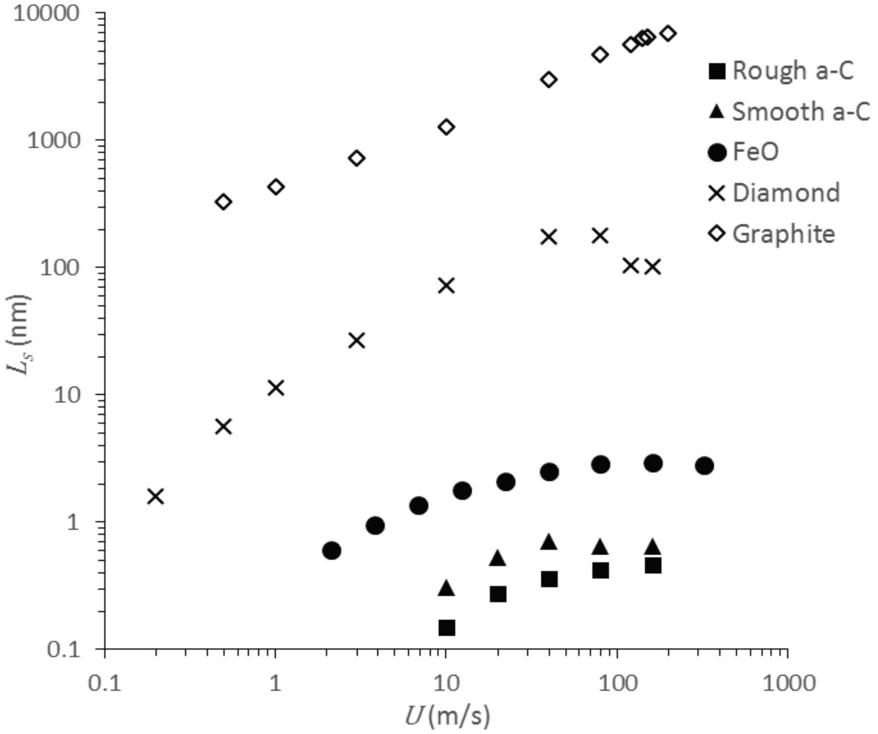

Figure V-5. Slip length variation with the Shearing Velocity computed for five shearing surfaces

The slip length varies over five orders of magnitude with the considered surfaces, graphite being the most slippery material. As for the evolution of the velocity ratio between the interfacial slip and the imposed shearing (Figure V-3), the slip length of iron oxide and a-C surfaces saturates over a given shearing velocity. This behavior was observed and explained in Chapter IV for the iron oxide and the same mechanism occurs here with non-slippery a-C surfaces. The effective shearing of the fluid initiates two effects causing a drop of the viscosity: shear thinning and temperature increase. As the slip length characterizes the competition between the interfacial slip and the fluid strain to absorb the shearing (cf. Equation IV.5), when the fluid viscosity η decreases as fast as the fluid friction λ, the slip length saturates as the fluid is more prone to absorb the shear. The slip follows the same trend as the film thickness does not change.

Now that the dynamic behavior occurring in the fluid and at the fluid/solid interface has been detailed, its origins will be identified. Indeed, from this knowledge, the contact behavior could be controlled by better-informed design of the fluid and surfaces of the contact.

V.3 Origins of the dynamical behavior

V.3.1 Influence of the temperature

As detailed in the previous chapter, the temperature has also a major and complex role directly impacting the fluid viscosity and consequently, the slip length. When sheared by an adhesive surface, the fluid accommodates the shear. As a consequence, shear thinning effects and elevation of the lubricant temperature occur, drastically reducing its viscosity at high shear rates. When sheared by a more slippery surface, no shear thinning takes place and the fluid heats up more slightly. However, the generated energy might dissipate less as the interfacial thermal resistance R_{th} is generally higher with low friction surfaces [93], although it is not a universal assumption [193]. Hence, the surface material has a proven impact on the temperature but which is complex to foresee as the effects of thermal interfacial resistance and fluid shearing add to one another.

To assess the thermal properties of the studied surfaces, a comparison between the rise of the fluid temperature according to the produced energy reflects the interfacial thermal resistance R_{th}. In Figure V-6, for each surfaces is plotted the evolution of the fluid average temperature as a function of $Q.h$ the produced energy by a unit area of a contact nanopatch in each simulation, with Q the generated energy per unit volume and h the contact thickness. As the surfaces are the only frontiers with the lubricant, it also corresponds to the total heat flux through both surfaces.

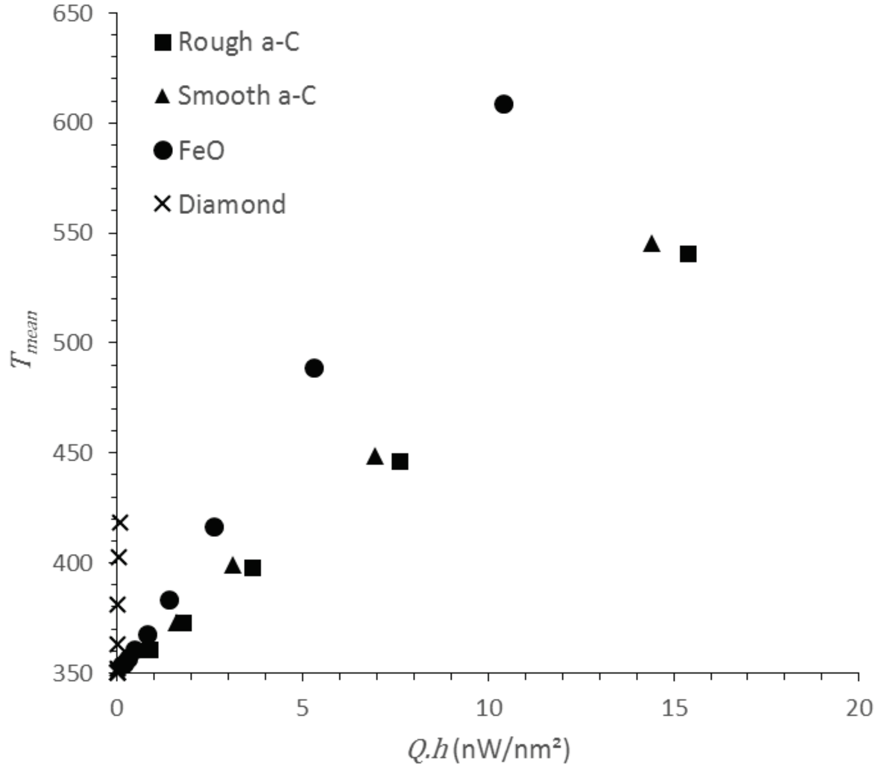

Figure V-6. Average temperature of the fluid with respect to the produced energy Q and the surface nature.

The case of the graphite-sheared systems is not computed as the effective shearing of the fluid is extremely low and consequently no heat is generated. For the other systems, it can be noticed that, even though a-C and FeO have close λ values, FeO surfaces exhibit higher thermal resistances than a-C ones as the temperature elevation resulting from similar energy production is higher. This can especially be explained by the greater effective contact area inherent to the rough a-C surfaces. This is also consistent with previous observations stating that the thermal resistance R_{th} is generally higher with surfaces featuring a lower friction [93]. Finally, the difference of the temperature rises has moderate influences on the viscosity (see Figure V-7): the viscosity variations between FeO and a-C simulations with the shear rate remain equivalent while the quick elevation of temperature with diamond surfaces induces an anticipated drop of the viscosity.

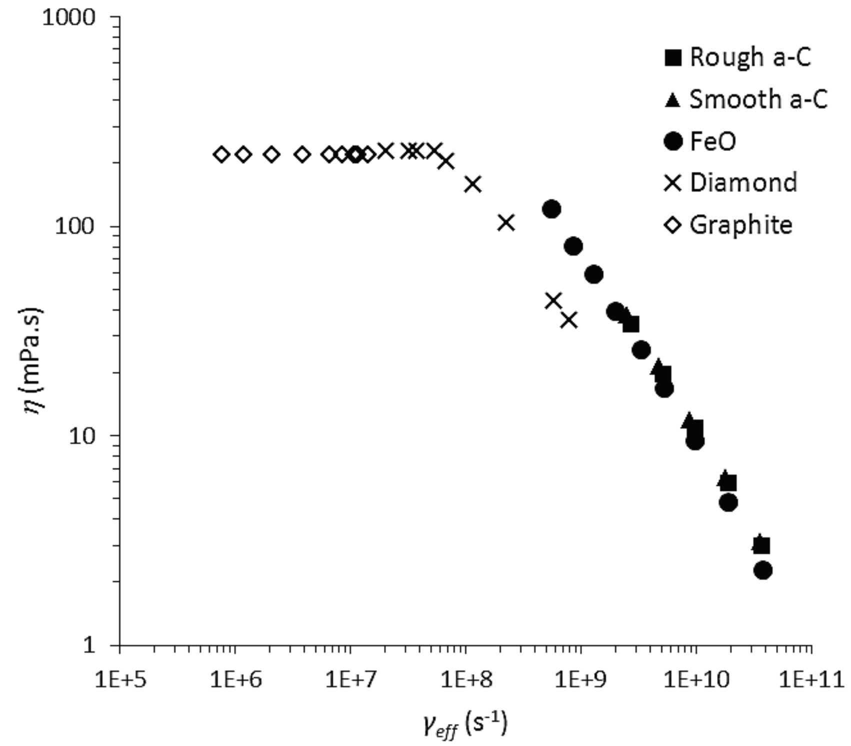

Figure V-7. Viscosity with respect to the effective shear rate and the surface nature.

According to the equation IV.5, this result suggests that the slip length induced by FeO surfaces should be lower than the one induced by a-C ones. Nonetheless, the opposite is observed (Figure V-5) as the slip length computed with FeO systems is up to two times the one computed with a-C ones. To explain the difference between the system dynamics featured by both kinds of surfaces, the slight differences between the film thicknesses of the simulated configuration must be considered.

V.3.2 *Influence of the film thickness*

In each simulated configuration, the number of molecules is the same but the film thickness features little variations depending on the shearing velocity (see Section IV.2.1) and the domain dimensions. Indeed, in order to guarantee the exact periodicity of the system, small variations of the domain dimensions in the x and y directions are necessary and induce slight disparities of the contact thickness h. Hence, at the same shearing velocity, the film thickness in simulations with FeO surfaces is roughly 15 % smaller than in ones with a-C surfaces.

Those small variations induce consequent modifications of the contact dynamics that are quite complex to predict as it acts on multiple intricate mechanisms. As $L_s = \eta/\lambda$ (Equation IV.5), {Fluid+surface} couples with similar interfacial fluid friction λ and similar η present the same slip length. Besides, according to Equations IV.1 and IV.2:

$$v_{slip} = L_s \times \dot{\gamma}_{eff} = \frac{U}{{}^{h}/_{L_s} + 2} \qquad (V.2)$$

Hence, with equivalent slip length L_s and shearing velocity U, both v_{slip} and $\dot{\gamma}_{eff}$ increase with a reduction of the contact thickness h. However, it has been shown than v_{slip} and $\dot{\gamma}_{eff}$ respectively impact the fluid friction coefficient λ and the fluid viscosity η and so the slip length… Predictions of the system dynamics thus depend on many intricate factors.

An approach to explain the difference between the dynamic behaviors featured with FeO surfaces and the a-C surfaces consist in taking the system with a-C materials as a reference one and compare the system with FeO to it. Given that the fluid friction coefficient λ of the FeO and of the a-C surfaces with the IL is of the same order of magnitude (see Figure V-4), and that the same liquid is used (so with equivalent fluid viscosity behavior, see Figure V-7), the slip length featured by both surfaces should be similar for equivalent operating conditions. Thus the smaller thickness in FeO simulations tends to increase the slip and the effective shear rate for the same imposed shearing velocity. Hence, it contributes to explain the discrepancy between the wall slip featured by FeO and a-C observed in Figure V-3, what is strengthened by the somewhat lower λ of FeO surfaces. Still in the case of the iron oxide surfaces, according to Figure IV-8, the slip length increases with the effective shear rate. This finally explicates the higher slip length of FeO simulations compared to a-C ones for equivalent shearing velocities U (see Figure V-5).

V.3.3 Surfaces specificities and fluid friction coefficient.

The effects of the interfacial fluid friction λ were computed for 5 distinct materials. The differences between each of them stem from the surface nature (composing atoms) and from their geometrical arrangement [83,174,175]. To estimate the influence of both of these factors, two parameters were computed: the geometrical roughness of the surface and its force corrugation (i.e. the maximum shear stress that the wall can transfer tangentially to the fluid molecules before the occurrence of wall slip) (Table V-2).

The geometrical roughness parameter was defined as follow: a plan of 200 by 200 probing atoms was set parallel to the tested surface and relaxed in the orthogonal direction to both the plan and the surface. The probing atoms interact with the surface atoms by the mean of a Lennard-Jones potential. The LJ parameters are the same for every probing atoms: a default energy ε of 1 Kcal/mole and a size σ of 3.2 Å characteristic of the [mmIm$^+$][NTf$_2^-$] atoms. The geometrical roughness is then estimated with the following expression.

$$h_{roughness} = \sqrt{\frac{1}{N}\sum_{i=1}^{N}(h(x,y)-\bar{h})^2} \qquad (V.3)$$

The force corrugation parameter is estimated by roaming the energy-mapping of the tested surface as previously described by Savio *et al.* [83]. This method computes the force needed to initiate a tangential movement between a model non-polar atom and the probed surface. Several directions are tested and the force corrugation parameters F_{corr} takes the value of the minimum force according to the different direction. Therefore, a minimum-force path is calculated, based on the assumption that the atoms try to slip in the direction opposing the least resistance to their movement. For both $h_{roughness}$ and F_{corr} parameters, the LJ potential alone is considered in their computations. Coulombic interactions of the iron oxide surfaces are not taken into account given that the probing atoms are non-polar ones. In the following analysis, the fluid friction λ of the different cases is compared for interfacial velocity slip of 5 m/s. To do so, interpolations are made between the data plotted in the Figure V-4.

	Graphite	Diamond	Smoothest a-C	Roughest a-C	FeO
$h_{roughness}$ (Å)	0.0115	0.0534	0.5709	0.8202	0.0705
F_{corr} (kcal/mol/Å)	0.1347	0.5475	1.7112	2.2688	0.3498 (non-polar)
λ (mPa.s/Å)	0.0217	0.5061	4.0353	4.1484	3.06

Table V-2. Geometrical roughness and force corrugation parameter for every five surfaces. The fluid friction coefficient at 5 m/s is added for comparison.

For carbon-based materials, a direct correlation exists between the surface characteristics of geometrical roughness and force corrugation, and the resulting fluid friction with the ionic liquid. As an example, to a geometrical roughness of 0.0115 Å and a force corrugation of 0.1347 kcal/mol/Å for the graphite corresponds a fluid friction of 0.0217 mPa/Å. Comparatively, a fluid friction of 4.1484 mPa/Å is attributed to the roughest a-C material, for a geometrical roughness of 0.8202 Å and a force corrugation of 2.2688 kcal/mol/Å. More generally, at low friction, λ is very sensitive to the increase of geometrical roughness and force corrugation: between graphite and diamond, both parameters are increased by a factor ≈ 5 and the fluid friction is multiplied by ≈ 20. While at higher friction, λ is much less sensitive: while there is about 30% of discrepancy between the corrugation and the roughness of DLCs surfaces, the fluid friction only varies by 3%. This behavior is consistent with the result obtained by Savio and coworkers studying the interactions of alkanes with surfaces of various natures [83]. In particular, as soon as a nanoroughness is present at the surfaces, the slip is greatly reduced [131].

With iron oxide the friction is substantially high (3.06 mPa.s/Å at a 5 m/s interface velocity slip), whereas the measured geometrical roughness and force corrugation are close to the values obtained for diamond. As the Coulombic interactions are not considered in the calculation of the surface parameters, this large differences between the measured value of λ and the one that could be expected from the previous correlations, suggest a large influence of the surface polarity on friction when interacting with a polar fluid (as a ionic liquid) that is reflected by an substantial increase of the force corrugation. On the other hand, experimental observations exposed with a very similar IL ([emIm][NTf_2^-]) sheared by mica surfaces (charged material) [121] point out the locking of the counterions of IL on the mica that considerably reduces the flow of the fluid near the interface. This feeds the debate on the influence of the surface charges on friction: friction is higher with polar (but not necessarily charged) solid materials than with non-polar materials for short alkyl-chain ionic liquids and in a dry (water-free) environment.

V.4 Implications for the lubrication performance

The order of magnitude of the slip length for the graphite goes from 1 to 10 µm. Considering the average film thickness in the EHL regime is around 0.1-1 µm, and given the relation between the slip length and the contact thickness made explicit in Equation V.1, a contact of this size implying at least one perfect graphite surface would be exclusively driven by the surface and the fluid would be very little sheared. However, lubrication would still be ensured as the thickness at the contact inlet would always be higher than the slip length what guarantees that the lubricant is drag into the contact. Diamond slip length rises up to 0.1 µm at high shearing velocities so slip would still be significant for diamond-sheared contacts with standard film thicknesses (roughly 0.1 µm) and predominant in the VTF regime (1-10 nm). For iron oxide and a-C surfaces, the slip length is comprised between 0.0001 and 0.003 µm and become negligible compared to classic film thicknesses. In this case, the shearing is mainly absorbed by the viscous fluid. Nonetheless, thanks to the progress made in surface conception and with the use of less viscous lubricants, the film thickness might decrease significantly in the future what would intensify the role of wall slip [55,58]. Yet, in today lubricated systems the surface roughness causes local film thickness reductions under 10 nanometers (see Figure I-4). This strengthen the importance of slip in the contact response. Knowing the slip capability of the fluid/surface couple is crucial in those cases to predict local film breakdown [29].

In a lubricated contact, the two confining surfaces move in the same direction and a relative sliding velocity might take place between the two. The wall with the higher velocity in the direction of the flow is considered as the entraining surface. According to Savio and coworkers [194], systems with surfaces of different nature are subject to complex lubrication responses depending on the slippage properties of both surfaces. It turns out from nano-EHL simulations that two opposite situations are willing to take place. If the entraining surface slips more than the other one, less lubricant is drag out of the confinement and as the mass flow is conservative, the thickness of the fluid film increases. On the other hand, when the entraining surface grips the fluid more than the other, the lubricant is expelled out of the confinement and local film breakdown might occurs.

During the design of a DLC/IL lubricated system, it is also important to estimate the range of the temperature rise as it has a consequent impact on the chemical reactivity between the two species and graphitization might occurs impacting friction and wear [185]. This effect could be amplified all the more given that the amorphous carbon thermal diffusion is relatively low [195,196].

Conclusion

Nowadays, the demand for smaller, more durable, more efficient and environmentally friendly lubricated systems is growing. The significant decrease in the quantity of oil and additives, as well as the use of low viscosity operating fluids as lubricants and of better manufacturing techniques, are inevitably leading to a reduction of film thickness, which can reach a few nanometers. At this scale, the classical continuum dynamics formulations are no longer valid as fluid molecules introduce a specific behavior when nanoconfined between two sliding surfaces. In fact, the structuration in layers near the interfaces, the wall slip, the anomalous rheological response and the particular thermal behavior lead to a highly complex response of the lubricated contact (**Chapter I**).

Simultaneously, due to their promising capabilities, the search for new lubricants to overcome the performance of those commonly employed leads inevitably to consider the ionic liquids. In addition to their valuable resistance to extreme environments (as ultra-low pressures or high temperatures), they can also exhibit superior tribological performance than conventional lubricating oils in the most common conditions. However, various natures and properties of ionic liquids exist, due to the quasi-infinite number of ions combinations available.

In this work one model ionic liquid was considered with rheological properties close to the conventional lubricants. Molecular Dynamics simulations were used to study its transport properties (**Chapter II**), completed by some in-house experiments.

A first objective of this work was to characterize the rheological behavior of the model ionic liquid in the EHD and very thin film lubrication regimes. MD simulations of the bulk ionic liquid provided quantitative agreement with experiments regarding viscosity-pressure and viscosity-temperature dependencies (**Chapter III**). The linear and non-linear regimes were explored through more than 200 bulk simulations. They provided a basis for an original improvement of a classical rheological model, and established the high sensibility of the ionic liquid viscosity to shearing at high pressures and low temperatures in the non-linear regime.

A second objective was to further study the molecular phenomena occurring at nanoscale. Simulations of the same ionic liquid confined between two surfaces representative of a common steel-steel lubricated contact were considered in **Chapter IV.** First by means of static simulations, the orientation of the ions at the interface gave indications on the fluid/substrate reactivity. Then, a relative motion was introduced between the confining surfaces. It was first noticed that shearing has no effect on the fluid structuration. Classic wall slip and a saturation of the shear stress were observed. The atypical response of the effective viscosity, depending on the shear thinning and on the temperature, was investigated. Therefore, a predictive model of the temperature in nanoconfinements submitted to shearing was also established. Finally, it is noteworthy that the large temperature elevation induced by the considerable shearing of nanoconfined fluids is relevant with the trend to use highly thermally stable ionic liquids as lubricants.

At last, the interaction with carbon-based surfaces were studied in **Chapter V**. Comparing surfaces with different structures and compositions led to very distinct lubrication regimes. First, the graphite surfaces induce enormous wall slip, so the fluid is no longer sheared and the velocity difference is entirely absorbed at the liquid/solid interfaces. On the contrary, the non-flat amorphous carbon surfaces produce high fluid friction coefficients so the shearing fully takes place within the fluid thickness. Although small variations of interfacial fluid friction or fluid thickness slightly impact the shear stress, they imply very different slip regimes with slip lengths discrepancies of several orders of magnitude. Finally, polar surfaces of iron oxide lead to a significantly higher friction than non-polar diamond with comparable roughness.

Perspectives

The results of this thesis bring about relevant information to understand the lubrication mechanisms and for a better design of future lubricated systems. Besides, complementary investigations could also lead to further knowledge on this field.

Firstly, the relevance of the previous conclusions would benefit from a confrontation with different ionic liquids. Moreover, as it was experimentally observed, ionic liquids performed well with additives or as additives. It was shown by means of experimental studies that the presence of water in the ionic liquid composition has a great and complex influence on the lubrication performances. Numerical simulations could give an insight on the underlying mechanisms for the different cases of multi-component lubricants [197]. Finally, tests of short-alkyl chain ionic liquids with charged surfaces would complete the picture of the influence of charges on friction, as the formation of well-formed monolayers could increase the liquid mobility and thus reduce the friction.

Secondly, the mechanisms leading to a limitation of the shear stress at high shear rate shall be further investigated. Molecular dynamics simulations with fluid and surfaces of different natures would confirm the mechanisms highlighted here.

Besides, a more extensive investigation of the influence of the film thickness in ultra-confined systems would provide precious information on the transition between full film and mixed/boundary lubrication regimes.

Moreover, the high wall slip behavior of some carbon-based tested surfaces should deeply impact the friction and the dynamics of the contact, what remains to be verify by means of realistic experimental tests.

At last, the general rheological model proposed here to predict the viscosity in the non-linear regime shall be tested with different kinds of fluids of evaluate its relevance and universality.

Appendices

Appendix A. The r RESPA Integration Algorithm

The reversing Reference System Propagator Algorithm (r RESPA) is a multi-timescale integrator. Compared to the conventional Verlet integration algorithm, it allows to optimize the simulation times through a differentiation of the integration time steps. This way, an appropriate integration frequency is defined for each type of interatomic interaction, according to their respective sensitivity. Distinct studies validated this approach to model ionic liquids in Molecular Dynamics simualtions [198,199]

Algorithm theory

As defined in Section II.1.3, the conservative force F_c acting on one atom is the opposite of the gradient of its potential energy E:

$$F_c = -\nabla E \tag{II.1}$$

Decomposing the total interactive forces F_c between short range forces F_s and long range forces F_l , the positions $\boldsymbol{x}$ and velocity $\dot{\boldsymbol{x}}$ of each atoms are computed considering all forces every time step Δt using the following equations:

$$\boldsymbol{x}(t+\Delta t) = \boldsymbol{x}_s\left\{t+\Delta t; \boldsymbol{x}(t), \dot{\boldsymbol{x}}(t) + \frac{\Delta t}{2m} F_l[\boldsymbol{x}(t)]\right\} \tag{A.2}$$

$$\dot{\boldsymbol{x}}(t+\Delta t) = \dot{\boldsymbol{x}}_s\left\{t+\Delta t; \boldsymbol{x}(t), \dot{\boldsymbol{x}}(t) + \frac{\Delta t}{2m} F_l[\boldsymbol{x}(t)]\right\} + \frac{\Delta t}{2} F_l[\boldsymbol{x}(t+\Delta t)] \tag{A.3}$$

Where $\boldsymbol{x}_s$ and $\dot{\boldsymbol{x}}_s$ are respectively the position and velocity of atoms numerically solved for n time step $\delta t = \Delta t/n$ with the velocity Verlet algorithm [200] seeing only the short range forces:

$$\boldsymbol{x}_s(t+\delta t) = \boldsymbol{x}_s(t) + \Delta t . \dot{\boldsymbol{x}}_s(t) + \frac{\delta t}{2m} F_s[\boldsymbol{x}_s(t)] \tag{A.4}$$

$$\dot{\boldsymbol{x}}_s(t+\delta t) = \dot{\boldsymbol{x}}_s(t) + \frac{\delta t}{2m}\{F_s[\boldsymbol{x}_s(t)] + F_s[\boldsymbol{x}_s(t+\delta t)]\} \tag{A.5}$$

With the following initial conditions:

$$\boldsymbol{x}_s(t) = \boldsymbol{x}(t) + \frac{\Delta t}{2m} F_l[\boldsymbol{x}(t)] \quad \& \quad \dot{\boldsymbol{x}}_s(t) = \dot{\boldsymbol{x}}(t) + \frac{\Delta t}{2m} F_l[\boldsymbol{x}(t)] \tag{A.6}$$

Time step configuration

By iterating the position and velocity computation, cumulative errors are introduced, depending on the chosen time steps. The swifter displacement of atoms correspond to their thermal agitation and start to be appreciated at roughly 10^{-12} s. To ensure energy conservation in the thermodynamic ensemble, time steps closed to the femtosecond (10^{-15} s) are generally taken. However, as the errors introduced at each iteration depends on the interaction forces, a differentiation can be made between the hard ones (with high energy potential) and the soft ones (with low energy potential). Hard forces must be integrated more often than the soft ones as they can lead to consequent accelerations over small time steps.

More specifically, the long range interactions of Coulomb and Lennard-Jones (Equation II.7) present softer potential that the short range ones of Tersoff (Equation II.18) and bonded interactions (Equation II.9). Hence, the short range interaction integration time step δt was taken equal to 0.5 fs and the long range interaction one Δt was taken equal to 2 fs.

Appendix B. Force field parameters

Long range interactions

In this study, all the long range interactions are non-bonded ones and bring together a classic 12-6 Lennard-Jones potential [138] and the Coulomb's law:

$$\boldsymbol{E_{non-bonded}} = \sum 4\varepsilon_{ij}\left(\left(\frac{\sigma_{ij}}{r_{ij}}\right)^{12} - \left(\frac{\sigma_{ij}}{r_{ij}}\right)^{6}\right) + \frac{1}{4\pi\varepsilon_0}\frac{q_i q_j}{r_{ij}} \qquad \text{(II.7)}$$

for $r_{ij} \leq 12$ Å and using the Lorentz-Berthelot mixing rules for Lennard Jones coefficients (Equation II.8). Within molecules, the non-bonded interactions are weighted not to interfere with the configured bonded interaction terms. The weighting factors are as follow:

- 0 for 1-bond separated atom
- 0 for 2-bonds separated atom
- 0.5 for more than 3-bonds separated atom

The following table present the mass, the Lennard-Jones coefficients and charges of the different simulated atoms.

	Atom	**Mass (g/mol)**	**σ_{ij} (Å)**	**ϵ_{ij} (kcal/mol)**	**q_i (e)**
Iron oxide	Fe	55.845	4.9059	9.0298E-06	2
	O	15.999	3.166	0.1554	-2
1,3-dymethylimidazolium [mmIm$^+$] (see Figure B-1 for the atom denominations)	N_A	14.0067	3.25	0.17	0.1125
	C_R	12.011	3.55	0.07	-0.0825
	C_W	12.011	3.55	0.07	-0.0975
	C_1	12.011	3.5	0.065999	-0.1275
	H_A	1.008	2.5	0.03	0.1575
	H_1	1.008	2.5	0.03	0.0975
Bis(trifluoromethylsulfonyl)imide [NTf$_2^-$]	O	15.9994	2.96	0.21	-0.3975
	S	32.065	3.55	0.25	0.765
	F	18.998	2.95	0.053	-0.12
	N	14.0067	3.25	0.17	-0.495
	C	12.0107	3.5	0.066	0.2625
Graphite	C	12	3.412	0.05511	-
Diamond and a-C	C	12	3.5	0.066	-

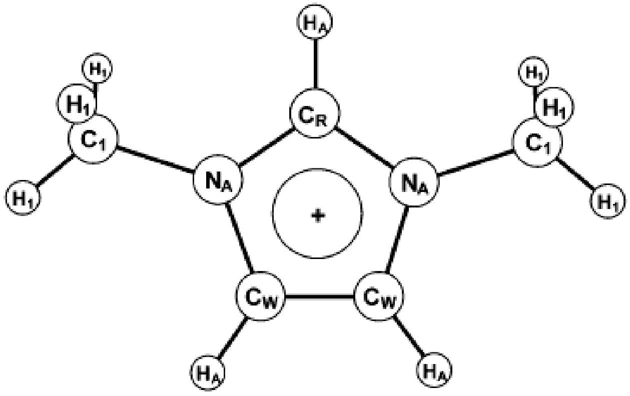

Figure B-1. 1,3-dymethylimidazolium [mmlm$^+$] molecule with atom denominations.

As the Coulombic interactions are very long range interactions, they must still be effective in simulations beyond the cut-off distance (for $r_{ij} > 12$ Å). As it would be too computationally expensive to describe them directly with the standard Coulomb's law, they are approximated through a particle-particle mesh (PPM) solver [139] which maps atom charge to a 3d mesh, uses 3d FFTs to solve Poisson's equation on the mesh, then interpolates electric fields on the mesh points back to the atoms.

As 3d FFTs are used, the PPM solver must operate in an infinite domain. Thus, as the confined simulations have periodic boundaries in the direction normal to the surfaces, a virtual empty space of 4 times the length of the domain is defined between the two non-periodic boundaries to simulate a 3d periodic (and so infinite) domain for the PPM solver.

Bonded-interactions

To describe the complex structure of ionic liquid molecules, their numerous degrees of freedom and the bond flexibility, the bonded term of the interaction potential energy is the combination of three components:

$$\boldsymbol{E_{bonded}} = \boldsymbol{E_{bond}} + \boldsymbol{E_{angle}} + \boldsymbol{E_{dihedral}} \qquad \text{(II.9)}$$

Atoms pairs linked with covalent bonds are model as tension/extension springs:

$$\boldsymbol{E_{bond}} = \sum_{bonds} K_b(r_{ij} - r_0) \qquad \text{(II.10)}$$

with K_b the bond stiffness, r_{ij} the distance between atoms i and j and r_0 the equilibrium distance.

	Bonds	r_0 (Å)	K_b (kcal/mol)
1,3-dymethylimidazolium [mmIm$^+$] (see Figure B-1 for the atom denominations)	C_R-N	1.315	477.0555
	C_W-N	1.378	427.1033
	C_1-N	1.466	336.9981
	C_R-H	1.08	339.762926[1]
	C_W-H	1.08	339.762926[1]
	C_W-C_W	1.341	520.076481
Bis(trifluoromethylsulfonyl)imide [NTf$_2^-$]	O-S	1.442	637.0545
	N-S	1.57	372.0035
	S-C	1.818	235.415
	C-F	1.323	441.7915

Forces between triplets of atoms are represented by an angle bending potential:

$$\boldsymbol{E_{angle}} = \sum_{angles} K_a\left(\theta_{ijk} - \theta_0\right) \tag{II.11}$$

with K_a the angle stiffness, θ_{ijk} the bending angle and θ_0 the equilibrium angle.

	Angles	θ_0 (°)	K_a (kcal/mol)
1,3-dymethylimidazolium [mmIm$^+$] (see Figure B-1 for the atom denominations)	C_W-N-C_R	108	69.93308
	C_R-N-C_1	126.4	69.93308
	C_W-N-C_1	125.6	69.93308
	N-C_R-N	109.8	69.93308
	N-C_R-H	125.1	34.96653
	N-C_W-H	122	34.96653
	N-C_W-C_W	107.1	69.93308
	C_W-C_W-H	130.9	34.96653
	N-C_1-H	110.7	74.8566
	H-C_1-H	107.8	65.98948
Bis(trifluoromethylsulfonyl)imide [NTf$_2^-$]	O-S-O	118.5	115.7955
	O-S-N	113.6	94.2855
	O-S-C	102.6	103.965
	N-S-C	100.2	97.512
	S-N-S	125.6	80.1845
	S-C-F	111.8	82.933
	F-C-F	107.1	93.3295

---

[1] Coefficient values taken from the AMBER96 force field [201]

Finally, torsion forces of covalent bonds between quadruplets of atoms are modeled with a dihedral potential:

$$\boldsymbol{E_{dihedral}} = \sum_{dihedrals} \frac{1}{2} K_{d,1}\left[1+\cos\left(\phi_{ijkl}\right)\right] + \frac{1}{2} K_{d,2}\left[1-\cos\left(2\phi_{ijkl}\right)\right] + \frac{1}{2} K_{d,3}\left[1+\cos\left(3\phi_{ijkl}\right)\right] \tag{II.12}$$

with $K_{d,i}$ the torsion stiffness of the different modes and ϕ_{ijkl} the torsion angle.

	Dihedrals	$\boldsymbol{K_{d,1}}$**(kcal/mol)**	$\boldsymbol{K_{d,2}}$**(kcal/mol)**	$\boldsymbol{K_{d,3}}$**(kcal/mol)**
1,3-dymethylimidazolium [mmIm$^+$] (see Figure B-1 for the atom denominations)	N-C_R-N-C_W	0	4.651	0
	H-C_R-N-C_1	0	4.651	0
	C_R-N-C_W-C_W	0	3	0
	C_W-N-C_1-H	0	3	0
	C_R-N-C_1-H	0	0	0
	N-C_R-N-C_1	0	4.651	0
	H-C_R-N-C_1	0	4.651	0
	C_1-N-C_W-C_W	0	3	0
	C_1-N-C_W-H	0	3	0
	C_W-N-C_1-H	0	0	0.1314
	N-C_W-C_W-N	0	10.75	0
	N-C_W-C_W-H	0	10.75	0
	H-C_W-C_W-H	0	10.75	0
1,3-dymethylimidazolium (improper dihedrals)	N	0	2.0004	0
	$C_{R/W}$	0	2.1988	0
Bis(trifluoromethylsulfonyl)imide [NTf$_2^-$]	O-S-N-S	0	0	-0.003585
	O-S-C-F	0	4.651	0.34679
	C-S-N-S	7.83294	-2.49044	-0.76362
	N-S-C-F	0	0	0.31596

Tersoff potential

Tersoff is a reactive potential able to model the breakable bonded interactions of some atoms. It was used in this study to represent most of the C-C interactions in carbon based-materials. The Equation II.8 introduced in section II.3.1 is completed here:

$$\boldsymbol{E_{Tersoff}} = \frac{1}{2}\sum_{i \neq j} f_C\left(r_{ij}\right).\left(Ae^{-\lambda_1 r_{ij}} - b_{ij}Be^{-\lambda_2 r_{ij}}\right) \tag{II.18}$$

with A and B two constants, λ_1 and λ_2 two atom-dependent parameters and b_{ij} a weighting coefficient including a three-body term to embody the bond ordering:

$$
\begin{aligned}
f_C(r) &= \begin{cases} 1 & : \; r < R - D \\ \frac{1}{2} - \frac{1}{2}\sin\left(\frac{\pi}{2}\frac{r-R}{D}\right) & : \; R - D < r < R + D \\ 0 & : \; r > R + D \end{cases} \\
b_{ij} &= \left(1 + \beta^n {\zeta_{ij}}^n\right)^{-\frac{1}{2n}} \\
\zeta_{ij} &= \sum_{k \neq i,j} f_C(r_{ik}) g(\theta_{ijk}) \exp\left[{\lambda_3}^m (r_{ij} - r_{ik})^m\right] \\
g(\theta) &= \gamma_{ijk}\left(1 + \frac{c^2}{d^2} - \frac{c^2}{\left[d^2 + (\cos\theta - \cos\theta_0)^2\right]}\right)
\end{aligned}
$$

The values of the parameters are given in the following table.

Parameter	Unit	Graphite	Diamond and a-C
$\boldsymbol{m}$	-	3	3
$\boldsymbol{\gamma_{ikj}}$	-	1	1
$\boldsymbol{\lambda_3}$	Å^{-1}	0	0
$\boldsymbol{c}$	-	38049	38049
$\boldsymbol{d}$	-	4.3484	4.3484
$\boldsymbol{\cos\theta_0}$	-	-0.57058	-0.930
$\boldsymbol{n}$	-	0 .72751	0 .72751
$\boldsymbol{\beta}$	-	1.5724.10^{-7}	1.5724.10^{-7}
$\boldsymbol{\lambda_2}$	Å^{-1}	2.2119	2.2119
$\boldsymbol{B}$	kcal/mol	7995.09	9916.00
$\boldsymbol{R}$	Å	1.95	1.95
$\boldsymbol{D}$	Å	0.15	0.15
$\boldsymbol{\lambda_1}$	Å^{-1}	3.4879	3.4879
$\boldsymbol{A}$	kcal/mol	32137.17	32137.17

Appendix C. Toward extreme confinements

It had been shown that the structuration of the nanoconfined fluid has a direct impact on the fluid viscosity and thus on the friction [173]. In the previous configuration of roughly 3 nm thick confinements, no influence of the structuration on the viscosity were noticed. However, the question still ran for ultra-confined systems (< 1 nm thick) for which the structuration of the fluid in the thickness is extreme. Hence, four new systems with fewer ionic liquid molecule pairs were simulated over several shearing velocities. The resulting friction is plotted in Figure D-1.

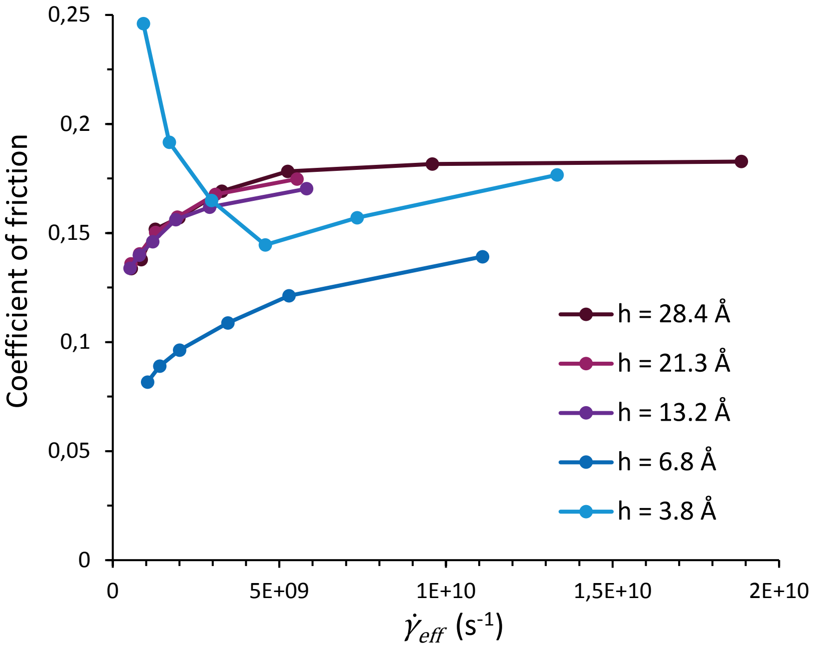

Figure D-1. Evolution of the coefficient of friction with the shearing and the lubricant film thickness.

Firstly, it can be noticed that whatever the film thickness, the coefficient of friction (COF) always tends to saturate with increasing shear rate. As the effects of slip and warming are still occurring, those last results comfort with the idea that the same mechanisms induce a limitation of the shear stress. Secondly, the film thickness reduction has a significant influence only under about ten Angstroms. Indeed, from 28.4 Å to 13.2 Å, the measured friction is quite stable whereas it is reduced of roughly 25 % when the film thickness reaches 6.8 Å and increase once again when reducing the thickness to 3.8 Å. To understand this unintuitive behavior, a look at the fluid structuration is crucial.

Considering the normalized coordinate z/h, the Figure D-2 represents the numerical density of the ions in layers perpendicular to the thickness. For more than one nanometer thick contacts, one well-formed layer is present at each fluid/solid interfaces and more heterogeneous layers takes place between them. The lowest friction is reached when those two layers are not separated by structured fluid (h = 6.8 Å) and the friction increased when the layers merge into a single one (h = 3.8 Å). This is in accordance with the observations of Savio on n-hexadecane [15]. To explain the discontinuity of the COF with the reduction of the thickness, Savio claims that the two well-formed layers will easily slip on one another, whereas a single layer is more difficult to shear. In a recent experimental study, Sweeney *et al.* compared the friction resulting from the shear of a single layer of IL and for ILs with different ion structures [170]. In this "boundary regime" friction is also found to be higher than with multilayer confinements. In fact, as a single layer of fluid cannot be sheared, mechanisms requiring more energy take place. When interfacial slip is prevailing, the energy is mainly dissipated by expulsion of near contact fluid. With lesser slip, the energy is mainly dissipated to deform and rotate the ions in the boundary layer.

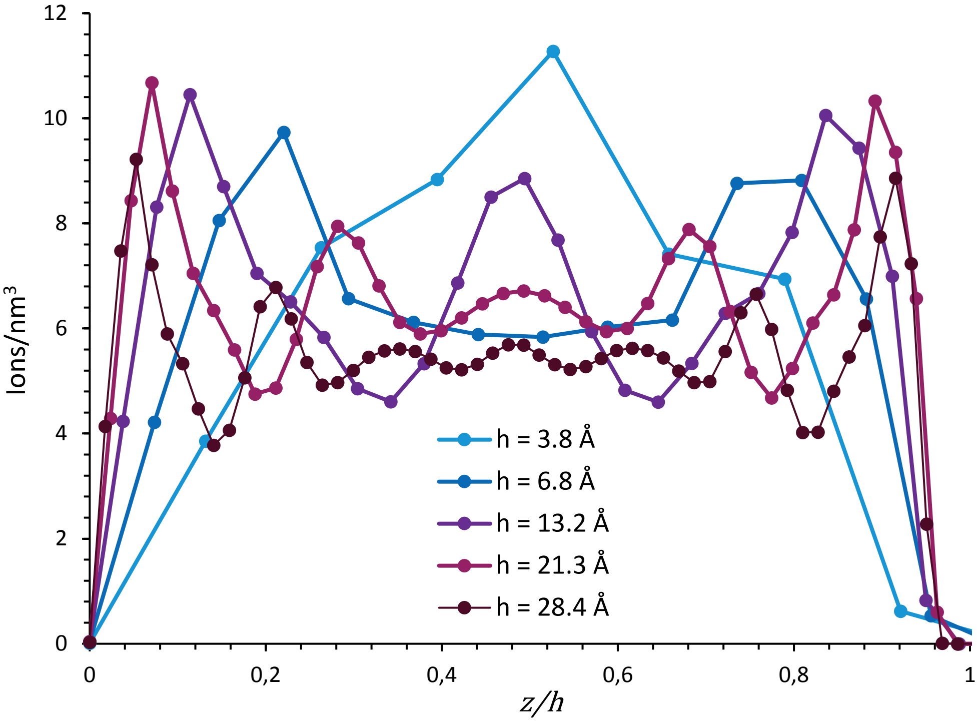

Figure D-2. Evolution of the density profile in relation with the film thickness. The abscissa is normalized by the film thickness.

A last singularity inherent to the reduction of the film thickness is the important increase of friction at low shearing velocity. Further investigation are necessary to fully characterize this anomalous behavior. A first hypothesis can be formulated. At low shear rate, the thin dense layer of ionic liquid crystalizes (as it was experimentally observed in chapter III) and exhibit a solid-like behavior. On the other hand, the increase of the shearing forces the strain of the fluid and introduces a dynamic lift between the two surfaces generating less friction than at low shear.

References

[1] Harris KR, Kanakubo M, Woolf LA. Temperature and Pressure Dependence of the Viscosity of the Ionic Liquids 1-Hexyl-3-methylimidazolium Hexafluorophosphate and 1-Butyl-3-methylimidazolium Bis(trifluoromethylsulfonyl)imide. J Chem Eng Data 2007;52:1080–5. doi:10.1021/je700032n.

[2] Ramasamy US, Bair S, Martini A. Predicting Pressure--Viscosity Behavior from Ambient Viscosity and Compressibility: Challenges and Opportunities. Tribol Lett 2015;57:1–7. doi:10.1007/s11249-014-0454-5.

[3] Liu P, Yu H, Ren N, Lockwood FE, Wang QJ. Pressure--Viscosity Coefficient of Hydrocarbon Base Oil through Molecular Dynamics Simulations. Tribol Lett 2015;60:1–9. doi:10.1007/s11249-015-0610-6.

[4] Gupta SA, Cochran HD, Cummings PT. Shear behavior of squalane and tetracosane under extreme confinement. III. Effect of confinement on viscosity. J Chem Phys 1997;107:10335–43. doi:10.1063/1.474173.

[5] Chan DYC, Horn RG. The drainage of thin liquid films between solid surfaces. J Chem Phys 1985;83:5311–24. doi:10.1063/1.449693.

[6] Granick S. Motions and Relaxations of Confined Liquids. Science (80-) 1991;253:1374–9. doi:10.1126/science.253.5026.1374.

[7] Jabbarzadeh A, Harrowel P, Tanner RI. Crystal Bridge Formation Marks the Transition to Rigidity in a Thin Lubrication Film. Phys Rev Lett 2006;96:1–4. doi:10.1103/PhysRevLett.96.206102.

[8] Bitsanis I, Somers SA, Davis HT, Tirrell M. Microscopic dynamics of flow in molecularly narrow pores. J Chem Phys 1990;93:3427–31. doi:10.1063/1.458823.

[9] Thompson PA, Grest GS, Robbins MO. Phase Transitions and Universal Dynamics in Confined Films. Phys Rev Lett 1992;68:3448–51. doi:10.1103/PhysRevLett.68.3448.

[10] Alsten J Van, Granick S. Molecular Tribometry of Ultrathin Liquid Films. Phys Rev Lett 1988;61:2570–3. doi:10.1103/PhysRevLett.61.2570.

[11] Gee ML, McGuiggan PM, Israelachvili JN, Homola AM. Liquid to solidlike transitions of molecularly thin films under shear. J Chem Phys 1990;93:1895–906. doi:10.1063/1.459067.

[12] Magda JJ, Tirrell M, Davis HT. Molecular dynamics of narrow, liquid-filled pores. J Chem Phys 1985;63:1886–901.

[13] Horn RG, Israelachvili JN. Direct measurement of structural forces between two surfaces in a nonpolar liquid. J Chem Phys 1981;75:1400–11. doi:10.1063/1.442146.

[14] Gao J, Luedtke WD, Landman U. Layering Transitions and Dynamics of Confined Liquid Films. Phys Rev Lett 1997;79:705–8.

[15] Savio D. Nanoscale phenomena in lubrication: from atomistic simulations to their integration into continuous models. phdthesis. INSA de Lyon, 2013.

[16] Lauga E, Brenner MP, Stone HA. Microfluidics: The no-slip boundary condition. ArXiv Condens Matter E-Prints 2005.

[17] Berro H, Fillot N, Vergne P. Molecular dynamics simulation of surface energy and {ZDDP} effects on friction in nano-scale lubricated contacts. Tribol Int 2010;43(10):1811–22. doi:http://dx.doi.org/10.1016/j.triboint.2010.02.011.

[18] Freemantle M. An Introduction to Ionic Liquids. The Royal Society of Chemistry; 2009.

[19] Dold C, Amann T, Kailer A. Influence of structural variations on imidazolium-based ionic liquids. Lubr Sci 2013;25:251–68. doi:10.1002/ls.1219.

[20] Zhou F, Liang Y, Liu W. Ionic liquid lubricants: designed chemistry for engineering applications. Chem Soc Rev 2009;38:2590–9. doi:10.1039/B817899M.

[21] Perkin S, Crowhurst L, Niedermeyer H, Welton T, Smith AM, Gosvami NN. Self-assembly in the electrical double layer of ionic liquids. Chem Commun 2011;47:6572–4. doi:10.1039/C1CC11322D.

[22] Atkin R, Warr GG. Structure in Confined Room-Temperature Ionic Liquids. J Phys Chem C 2007;111:5162–8. doi:10.1021/jp067420g.

[23] Bou-Malham I, Bureau L. Nanoconfined ionic liquids: effect of surface charges on flow and molecular layering. Soft Matter 2010;6:4062–5. doi:10.1039/C0SM00377H.

[24] Stolte S, Matzke M, Arning J, Boschen A, Pitner W-R, Welz-Biermann U, et al. Effects of different head groups and functionalised side chains on the aquatic toxicity of ionic liquids. Green Chem 2007;9:1170–9. doi:10.1039/B711119C.

[25] Canongia Lopes JN, Pádua AAH. Molecular Force Field for Ionic Liquids Composed of Triflate or Bistriflylimide Anions. J Phys Chem B 2004;108:16893–8. doi:10.1021/jp0476545.

[26] Canongia Lopes JN, Deschamps J, Pádua AAH. Modeling Ionic Liquids Using a Systematic All-Atom Force Field. J Phys Chem B 2004;108:2038–47. doi:10.1021/jp0362133.

[27] Cremer T, Stark M, Deyko A, Steinrück H-P, Maier F. Liquid/Solid Interface of Ultrathin Ionic Liquid Films: [C1C1Im][Tf2N] and [C8C1Im][Tf2N] on Au(111). Langmuir 2011;27:3662–71. doi:10.1021/la105007c.

[28] Mendonça ACF, Malfreyt P, Pádua AAH. Interactions and Ordering of Ionic Liquids at a Metal Surface. J Chem Theory Comput 2012;8:3348–55. doi:10.1021/ct300452u.

[29] Savio D, Fillot N, Vergne P. A Molecular Dynamics Study of the Transition from Ultra-Thin Film Lubrication Toward Local Film Breakdown. Tribol Lett 2013;50:207–20. doi:10.1007/s11249-013-0113-2.

[30] Robertson J. Properties of diamond-like carbon. Surf Coatings Technol 1992;50:185–203. doi:http://dx.doi.org/10.1016/0257-8972(92)90001-Q.

[31] Robertson J. Diamond-like amorphous carbon. Mater Sci Eng R Reports 2002;37:129–281. doi:http://dx.doi.org/10.1016/S0927-796X(02)00005-0.

[32] Dowson D. History of Tribology. London: Longman; 1979.

[33] Reynolds O. On the Theory of Lubrication and its Application to {Mr. Beauchamp Tower's} Experiments, including an Experimental Determination of the Viscosity of Olive Oil. Philos Trans Roy Soc London 1886;177:157–234.

[34] Jacobson B. The Stribeck memorial lecture. Tribol Int 2003;36:781–9.

[35] Hertz H. {Ü}ber die {B}erührung fester elastischer {K}örper. J Für Die Reine Und Angew {M}athematik 1881;92:156–71.

[36] Barus C. Isothermal, Isopiestics and Isometrics Relative to Viscosity. Am J Sci 1893;45:87–96.

[37] Roelands CJA. Correlational aspects of the viscosity-temperature-pressure relationship of lubricating oil. phdthesis. Techische Hogeschool Delft, 1966.

[38] Williams ML, Landel RF, Ferry JD. The Temperature Dependence of Relaxation Mechanisms in Amorphous Polymers and Other Glass-forming Liquids. J Am Chem Soc 1955;77:3701–7. doi:10.1021/ja01619a008.

[39] Dowson D, Higginson GR. Elasto-hydrodynamic lubrication: the fundamentals of roller and gear lubrication. Pergamon Press; 1966.

[40] Ertel A. Hydrodynamic lubrication based on new principles. Akad SSR Prikadnaya Math I Mekhanika 1939;2:41–52.

[41] Grubin AN, Vinogradova IE. Investigation of the contact of machine components. Central Scientific Research Institute for Technology and Mechanical Engineering Moscow; 1949.

[42] Doki-Thonon T, Fillot N, Morales Espejel GE, Querry M, Philippon D, Devaux N, et al. A Dual Experimental/Numerical Approach for Film Thickness Analysis in TEHL Spinning Skewing Circular Contacts. Tribol Lett 2013;50:115–26. doi:10.1007/s11249-013-0122-1.

[43] Habchi W, Vergne P, Bair S, Andersson O, Eyheramendy D, Morales-Espejel GE. Influence of pressure and temperature dependence of thermal properties of a lubricant on the behaviour of circular {TEHD} contacts. Tribol Int 2010;43:1842–50. doi:http://dx.doi.org/10.1016/j.triboint.2009.10.002.

[44] Bruyere V, Fillot N, Morales-Espejel GE, Vergne P. Computational fluid dynamics and full elasticity model for sliding line thermal elastohydrodynamic contacts. Tribol Int 2012;46:3–13. doi:http://dx.doi.org/10.1016/j.triboint.2011.04.013.

[45] Habchi W, Issa J. Fast and Reduced Full-system Finite Element Solution of Elastohydrodynamic Lubrication Problems: Line Contacts. Adv Eng Softw 2013;56:51–62. doi:10.1016/j.advengsoft.2012.11.009.

[46] Evans HP, Hughes G. Evaluation of deflection in semi-infinite bodies by a differential method. Proc IMechE Part C J Mech Eng Sci 2000;214(4):563–584.

[47] Venner CH, Lubrecht AA. Multi-Level Methods in Lubrication. Elsevier; 2000.

[48] Pensado AS, Comuñas MJP, Fernández J. The pressure-viscosity coefficient of several ionic liquids. Tribol Lett 2008;31:107–18.

[49] Sharma BK, and Arthur J. Stipanovic. Pressure Viscosity Coefficient of Lubricant Base Oils As Estimated by Nuclear Magnetic Resonance Spectroscopy. Ind Eng Chem Res 2002;41:4889–98. doi:10.1021/ie020360q.

[50] Sargent LBJ. Pressure-Viscosity Coefficients of Liquid Lubricants. A S L E Trans 1983;26:1–10. doi:10.1080/05698198308981471.

[51] Bair S. A Rough Shear-Thinning Correction for EHD Film Thickness. STLE Trib Trans 2004;47:361–5.

[52] Berro H. A molecular dynamics approach to nano-scale lubrication. phdthesis. INSA de Lyon, 2010.

[53] McCabe C, Manke CW, Cummings PT. Predicting the Newtonian viscosity of complex fluids from high strain rate molecular simulations. J Chem Phys 2002;116:3339–42. doi:http://dx.doi.org/10.1063/1.1446045.

[54] Kioupis LI, and Edward J. Maginn. Impact of Molecular Architecture on the High-Pressure Rheology of Hydrocarbon Fluids. J Phys Chem B 2000;104:7774–83. doi:10.1021/jp000966x.

[55] Lugt PM, Severt RWM, Fogelström J, Tripp JH. Influence of surface topography on friction, film breakdown and running-in in the mixed lubrication regime. Proc Inst Mech Eng Part J J Eng Tribol 2001;215:519–33.

[56] Lugt PM, Morales-Espejel GE. A Review of Elasto-Hydrodynamic Lubrication Theory. Tribol Trans 2011;54:470–96. doi:10.1080/10402004.2010.551804.

[57] Habchi W. A full-system finite element approach to elastohydrodynamic lubrication problems: application to ultra-low-viscosity fluids. phdthesis. MEGA, INSA de Lyon, 2008.

[58] Habchi W, Vergne P, Eyheramendy D, Morales-Espejel GE. Numerical investigation of the use of machinery low-viscosity working fluids as lubricants in elastohydrodynamic lubricated point contacts. Proc IMechE Part J J Eng Tribol 2011;225:465–77.

[59] Bhushan B, Israelachvili JN, Landman U. Nanotribology: friction, wear and lubrication at the atomic scale. Nature 1995;374:607–16. doi:10.1038/374607a0.

[60] Israelachvili JN. Intermolecular and Surface Forces. 2nd revise. Academic Press Inc; 1991.

[61] Frantz P, Agrait N, Salmeron M. Use of Capacitance to Measure Surface Forces. 1. Measuring Distance of Separation with Enhanced Spatial and Time Resolution. Langmuir 1996;12:3289–3294. doi:10.1021/la960014b.

[62] Binnig G, Rohrer H, Gerber C, Weibel E. Surface Studies by Scanning Tunneling Microscopy. Phys Rev Lett 1982;49:57–61. doi:10.1103/PhysRevLett.49.57.

[63] Binnig G, Quate CF, Gerber C. Atomic Force Microscope. Phys Rev Lett 1986;56:930–3. doi:10.1103/PhysRevLett.56.930.

[64] Metropolis N, Ulam S. The monte carlo method. J Am Stat Assoc 1949;44:335–41.

[65] Metropolis N, Rosenbluth AW, Rosenbluth MN, Teller AH, Teller E. Equation of State Calculations by Fast Computing Machines. J Chem Phys 1953;21:1087–92. doi:http://dx.doi.org/10.1063/1.1699114.

[66] Allen MP, Tildesley DJ. Computer simulation of liquids. Oxford university press; 1989.

[67] Gao J, Luedtke WD, Landman U. Friction Control in Thin-Film Lubrication. J Phys Chem B 1998;102:5033–7. doi:10.1021/jp982150q.

[68] Stevens MJ, Mondello M, Grest GS, Cui ST, Cochran HD, Cummings PT. Comparison of shear flow of hexadecane in a confined geometry and in bulk. J Chem Phys 1997;106:7303–14.

[69] Jabbarzadeh A, Atkinson JD, Tanner RI. Nanorheology of molecularly thin films of n-hexadecane in Couette shear flow by molecular dynamics simulation. J Nonnewton Fluid Mech 1998;77:53–78. doi:DOI: 10.1016/S0377-0257(97)00094-3.

[70] Balasundaram R, Jiang S, Belak J. Structural and rheological properties of n-decane confined between graphite surfaces. Chem Eng J 1999;74:117–27.

[71] Luengo G, Israelachvili J, Granick S. Generalized effects in confined fluids: new friction map for boundary lubrication. Wear 1996;200:328–35. doi:http://dx.doi.org/10.1016/S0043-1648(96)07248-1.

[72] Gupta SA, Cochran HD, Cummings PT. Nanorheology of liquid alkanes. Fluid Phase Equilibr 1998;150–151:125–31.

[73] Coulomb. Premier mémoire sur l’électricité et le magnétisme. Histoire de l’Académie

Royale des Sciences; 1785.

[74] Thompson PA, Robbins MO. Shear flow near solids: Epitaxial order and flow boundary conditions. Phys Rev A 1990;41:6830–7. doi:10.1103/PhysRevA.41.6830.

[75] Gao J, Luedtke WD, Landman U. Structures, solvation forces and shear of molecular films in a rough nano-confinement. Tribol Lett 2000;9:3–13.

[76] Jabbarzadeh A, Harrowel P, Tanner RI. Low friction lubrication between amorphous walls: Unraveling the contributions of surface roughness and in-plane disorder. J Chem Phys 2006;125:34703. doi:10.1063/1.2216695.

[77] Jabbarzadeh A, Atkinson JD, Tanner RI. Effect of the wall roughness on slip and rheological properties of hexadecane in molecular dynamics simulation of Couette shear flow between two sinusoidal walls. Phys Rev E 2000;61:690–9. doi:10.1103/PhysRevE.61.690.

[78] Bitsanis I, Magda JJ, Tirrell M, Davis HT. Molecular dynamics of flow in micropores. J Chem Phys 1987;87:1733–50. doi:10.1063/1.453240.

[79] Heinbuch U, Fischer J. Liquid flow in pores: Slip, no-slip, or multilayer sticking. Phys Rev A 1989;40:1144–6.

[80] Somers SA, Davis HT. Microscopic dynamics of fluids confined between smooth and atomically structured solid surfaces. J Chem Phys 1992;96:5389–407. doi:10.1063/1.462724.

[81] Padilla P. Chemical structure effects on the equilibrium and under shear properties of thin films in confined geometries: A molecular dynamics simulation study. J Chem Phys 1995;103:2157–68.

[82] Jabbarzadeh A, Atkinson JD, Tanner RI. The effect of branching on slip and rheological properties of lubricants in molecular dynamics simulation of couette shear flow. Tribol Int 2002;35:35–46.

[83] Savio D, Fillot N, Vergne P, Zaccheddu M. A Model for Wall Slip Prediction of Confined n-Alkanes: Effect of Wall-Fluid Interaction Versus Fluid Resistance. Tribol Lett 2012;46:11–22. doi:10.1007/s11249-011-9911-6.

[84] Myers TG. Why are slip lengths so large in carbon nanotubes? Microfluid Nanofluidics 2011;10:1141–5. doi:10.1007/s10404-010-0752-7.

[85] Barrat J-L, Bocquet L or minute]ric. Influence of wetting properties on hydrodynamic boundary conditions at a fluid/solid interface. Faraday Discuss 1999;112:119–28. doi:10.1039/A809733J.

[86] Petrie CJS, Denn MM. Instabilities in polymer processing. Am Inst Chem Eng J 1976;22:209–36. doi:10.1002/aic.690220202.

[87] Bocquet L, Barrat J-L. Flow boundary conditions from nano- to micro-scales. Soft Matter 2007;3:685–693. doi:10.1039/b616490k.

[88] Ramamurthy A V. Wall Slip in Viscous Fluids and Influence of Materials of Construction. J Rheol (N Y N Y) 1986;30:337–57. doi:10.1122/1.549852.

[89] Jabbarzadeh A, Atkinson JD, Tanner RI. Wall slip in the molecular dynamics simulation of thin films of hexadecane. J Chem Phys 1999;110:2612–20. doi:10.1063/1.477982.

[90] Martini A, Hsu HY, Patankar NA, Lichter S. Slip at High Shear Rates. Phys Rev Lett 2008;100:1–4. doi:10.1103/PhysRevLett.100.206001.

[91] Tretheway D, Stone S, Meinhart C. Effects of Absolute Pressure and Dissolved Gasses on Apparent Fluid Slip in Hydrophobic Microchannels. APS Div. Fluid Dyn. Meet. Abstr., 2004.

[92] Fillot N, Berro H, Vergne P. From Continuous to Molecular Scale in Modelling Elastohydrodynamic Lubrication: Nanoscale Surface Slip Effects on Film Thickness and Friction. Tribol Lett 2011;43:257–66. doi:10.1007/s11249-011-9804-8.

[93] Barrat J-L, Chiaruttini F. Kapitza resistance at the liquid solid interface. Mol Phys 2003;101:1605–10. doi:10.1080/0026897031000068578.

[94] Raviv U, Perkin S, Laurat P, Klein J. Fluidity of Water Confined Down to Subnanometer Films. Langmuir 2004;20:5322–32. doi:10.1021/la030419d.

[95] Perkin S, Chai L, Kampf N, Raviv U, Briscoe W, Dunlop I, et al. Forces between Mica Surfaces, Prepared in Different Ways, Across Aqueous and Nonaqueous Liquids Confined to Molecularly Thin Films. Langmuir 2006;22:6142–52. doi:10.1021/la053097h.

[96] Perkin S, Kampf N, Klein J. Stability of Self-Assembled Hydrophobic Surfactant Layers in Water. J Phys Chem B 2005;109:3832–7. doi:10.1021/jp047746u.

[97] Kano M, Yasuda Y, Okamoto Y, Mabuchi Y, Hamada T, Ueno T, et al. Ultralow friction of DLC in presence of glycerol mono-oleate (GMO). Tribol Lett 2005;18:245–51. doi:10.1007/s11249-004-2749-4.

[98] Menter JW, Tabor D. Orientation of Fatty Acid and Soap Films on Metal Surfaces. Proc R Soc London Ser A Math Phys Sci 1951;204:514–24. doi:10.1098/rspa.1951.0008.

[99] Simic R, Kalin M, Hirayama T, Korelis P, Geue T. Fatty Acid Adsorption on Several DLC Coatings Studied by Neutron Reflectometry. Tribol Lett 2014;53:199–206. doi:10.1007/s11249-013-0257-0.

[100] Tomala A, Werner WSM, Gebeshuber IC, Dörr N, Störi H. Tribochemistry of monomolecular lubricant films of ethanolamine oligomers. Tribol Int 2009;42:1513–8. doi:http://dx.doi.org/10.1016/j.triboint.2009.06.004.

[101] Busselez R, Lefort R, Ji Q, Affouard F, Morineau D. Molecular dynamics simulation of nanoconfined glycerol. Phys Chem Chem Phys 2009;11:11127–33. doi:10.1039/B911859D.

[102] Müller-Plathe F, van Gunsteren WF. Solvation of poly(vinyl alcohol) in water, ethanol and an equimolar water-ethanol mixture: structure and dynamics studied by molecular dynamics simulation. Polymer (Guildf) 1997;38:2259–68. doi:http://dx.doi.org/10.1016/S0032-3861(96)00773-2.

[103] Loehle S, Matta C, Minfray C, Mogne T, Martin J-M, Iovine R, et al. Mixed Lubrication with C18 Fatty Acids: Effect of Unsaturation. Tribol Lett 2014;53:319–28. doi:10.1007/s11249-013-0270-3.

[104] Minami I. Ionic Liquids in Tribology. Molecules 2009;14:2286–305. doi:10.3390/molecules14062286.

[105] Perkin S. Ionic liquids in confined geometries. Phys Chem Chem Phys 2012;14:5052–62. doi:10.1039/C2CP23814D.

[106] Maginn EJ. Molecular simulation of ionic liquids current status and future opportunities. J Phys Condens Matter 2009;21:17.

[107] Morales W, Street KW, Richard RM, Valco DJ. Tribological Testing and Thermal Analysis of an Alkyl Sulfate Series of Ionic Liquids for Use as Aerospace Lubricants.

Tribol Trans 2012;55:815–21. doi:10.1080/10402004.2012.715322.

[108] Mordukhovich G, Qu J, Howe JY, Bair S, Yu B, Luo H, et al. A low-viscosity ionic liquid demonstrating superior lubricating performance from mixed to boundary lubrication. Wear 2013;301:740–6. doi:http://dx.doi.org/10.1016/j.wear.2012.11.076.

[109] Masuko M, Terawaki T, Kobayashi K, Aoki S, Suzuki A, Fujinami Y, et al. Contrasting Lubrication Properties of Imidazolium-Based Ionic Liquids Affected by the Nature of the Surface Under High Vacuum. Tribol Lett 2014;55:235–44. doi:10.1007/s11249-014-0353-9.

[110] Bosch. Conductive lubricants will protect the electric motors of the future. Press Releases 2014. http://www.bosch-presse.de/presseforum/details.htm?txtID=6814&locale=en.

[111] Kamimura H, Chiba T, Watanabe N, Kubo T, Nanao H, Minami I, et al. Effects of Carboxylic Acids on Friction and Wear Reducing Properties for Alkylmethylimidazolium Derived Ionic liquids. Tribol Online 2006;1:40–3. doi:10.2474/trol.1.40.

[112] Perkin S, Albrecht T, Klein J. Layering and shear properties of an ionic liquid, 1-ethyl-3-methylimidazolium ethylsulfate, confined to nano-films between mica surfaces. Phys Chem Chem Phys 2010;12:1243–7. doi:10.1039/B920571C.

[113] Somers AE, Howlett PC, MacFarlane DR, Forsyth M. A Review of Ionic Liquid Lubricants. Lubricants 2013;1:3–21. doi:10.3390/lubricants1010003.

[114] Amann T, Dold C, Kailer A. Rheological characterization of ionic liquids and ionic liquid crystals with promising tribological performance. Soft Matter 2012;8:9840–6. doi:10.1039/C2SM26030A.

[115] López Sánchez F, Otero I, López ER, Fernández J. Tribological Properties of Two Bis(trifluoromethylsulfonyl)imide-Based Ionic Liquids on Steel-Steel Contact. Tribol Trans 2014;57:637–46. doi:10.1080/10402004.2014.893475.

[116] Fernández J, Paredes X, Gaciño FM, Comuñas MJP, Pensado AS. Pressure-viscosity behaviour and film thickness in elastohydrodynamic regime of lubrication of ionic liquids and other base oils. Lubr Sci 2013;26:449–62. doi:10.1002/ls.1236.

[117] Spikes HA. A Thermodynamic Approach to Viscosity. Tribol Trans 1990;33:140–8. doi:10.1080/10402009008981940.

[118] Maolin S, Fuchun Z, Guozhong W, Haiping F, Chunlei W, Shimou C, et al. Ordering layers of [bmim][PF6] ionic liquid on graphite surfaces: Molecular dynamics simulation. J Chem Phys 2008;128. doi:http://dx.doi.org/10.1063/1.2898497.

[119] Deyko A, Cremer T, Rietzler F, Perkin S, Crowhurst L, Welton T, et al. Interfacial Behavior of Thin Ionic Liquid Films on Mica. J Phys Chem C 2013;117:5101–11. doi:10.1021/jp3115397.

[120] Beattie DA, Espinosa-Marzal RM, Ho TTM, Popescu MN, Ralston J, Richard CJE, et al. Molecularly-Thin Precursor Films of Imidazolium-Based Ionic Liquids on Mica. J Phys Chem C 2013;117:23676–84. doi:10.1021/jp4062863.

[121] Jitvisate M, Seddon JRT. Local Structure and Flow Properties of Ionic Liquids on Charged and Inert Substrates. J Phys Chem C 2016;120:4860–5. doi:10.1021/acs.jpcc.5b10727.

[122] Smith AM, Lovelock KRJ, Gosvami NN, Licence P, Dolan A, Welton T, et al. Monolayer

to Bilayer Structural Transition in Confined Pyrrolidinium-Based Ionic Liquids. J Phys Chem Lett 2013;4:378–82. doi:10.1021/jz301965d.

[123] Smith AM, Lovelock KRJ, Perkin S. Monolayer and bilayer structures in ionic liquids and their mixtures confined to nano-films. Faraday Discuss 2013;167:279–92. doi:10.1039/C3FD00075C.

[124] Liu X, Zhou F, Liang Y, Liu W. Tribological performance of phosphonium based ionic liquids for an aluminum-on-steel system and opinions on lubrication mechanism. Wear 2006;261:1174–9. doi:http://dx.doi.org/10.1016/j.wear.2006.03.018.

[125] Weng L, Liu X, Liang Y, Xue Q. Effect of tetraalkylphosphonium based ionic liquids as lubricants on the tribological performance of a steel-on-steel system. Tribol Lett 2007;26:11–7. doi:10.1007/s11249-006-9175-8.

[126] Jin C-M, Ye C, Phillips BS, Zabinski JS, Liu X, Liu W, et al. Polyethylene glycol functionalized dicationic ionic liquids with alkyl or polyfluoroalkyl substituents as high temperature lubricants. J Mater Chem 2006;16:1529–35. doi:10.1039/B517888F.

[127] Zeng Z, Phillips BS, Xiao J-C, Shreeve JM. Polyfluoroalkyl, Polyethylene Glycol, 1,4-Bismethylenebenzene, or 1,4-Bismethylene-2,3,5,6-Tetrafluorobenzene Bridged Functionalized Dicationic Ionic Liquids: Synthesis and Properties as High Temperature Lubricants. Chem Mater 2008;20:2719–26. doi:10.1021/cm703693r.

[128] Espinosa-Marzal RM, Arcifa A, Rossi A, Spencer ND. Ionic Liquids Confined in Hydrophilic Nanocontacts: Structure and Lubricity in the Presence of Water. J Phys Chem C 2014;118:6491–503. doi:10.1021/jp5000123.

[129] Espinosa-Marzal RM, Arcifa A, Rossi A, Spencer ND. Microslips to "Avalanches" in Confined, Molecular Layers of Ionic Liquids. J Phys Chem Lett 2014;5:179–84. doi:10.1021/jz402451v.

[130] Federici Canova F, Matsubara H, Mizukami M, Kurihara K, Shluger AL. Shear dynamics of nanoconfined ionic liquids. Phys Chem Chem Phys 2014;16:8247–56. doi:10.1039/C4CP00005F.

[131] Mendonça ACF, Padua AAH, Malfreyt P. Nonequilibrium Molecular Simulations of New Ionic Lubricants at Metallic Surfaces: Prediction of the Friction. J Chem Theory Comput 2013;9:1600–10. doi:10.1021/ct3008827.

[132] Amde M, Liu J-F, Pang L. Environmental Application, Fate, Effects, and Concerns of Ionic Liquids: A Review. Environ Sci Technol 2015;49:12611–27. doi:10.1021/acs.est.5b03123.

[133] Martini A. Molecular modeling and continuum analyses of thin film interfaces. phdthesis. Northwestern University, 2007.

[134] Martini A, Vadakkepatt A. Compressibility of Thin Film Lubricants Characterized Using Atomistic Simulation. Tribol Lett 2010;38:33–8. doi:10.1007/s11249-009-9568-6.

[135] Loehle S. Understanding of adsorption mechanisms and tribological behaviors of C18 fatty acids on iron-based surfaces: a molecular simulation approach. phdthesis. Ecole Centrale de Lyon, 2014.

[136] Tuckerman M, Berne BJ, Martyna GJ. Reversible multiple time scale molecular dynamics. J Chem Phys 1992;97:1990–2001.

[137] Jorgensen WL, David S. Maxwell, and Julian Tirado-Rives. Development and Testing of the OPLS All-Atom Force Field on Conformational Energetics and Properties of Organic

Liquids. J Am Chem Soc 1996;118:11225–36. doi:10.1021/ja9621760.

[138] Jones JE. On the Determination of Molecular Fields. II. From the Equation of State of a Gas. Proc R Soc London A Math Phys Eng Sci 1924;106:463–77. doi:10.1098/rspa.1924.0082.

[139] Hockney RW, Eastwood JW. Computer simulation using particles. CRC Press; 1988.

[140] Salanne M. Simulations of room temperature ionic liquids: from polarizable to coarse-grained force fields. Phys Chem Chem Phys 2015;17:14270–9. doi:10.1039/C4CP05550K.

[141] Nosé S. A unified formulation of the constant temperature molecular dynamics methods. J Chem Phys 1984;81:511–9. doi:http://dx.doi.org/10.1063/1.447334.

[142] Hoover WG. Canonical dynamics: Equilibrium phase-space distributions. Phys Rev A 1985;31:1695–7. doi:10.1103/PhysRevA.31.1695.

[143] Alfè D, Gillan MJ. First-Principles Calculation of Transport Coefficients. Phys Rev Lett 1998;81:5161–4. doi:10.1103/PhysRevLett.81.5161.

[144] Müller-Plathe F. Reversing the perturbation in nonequilibrium molecular dynamics: An easy way to calculate the shear viscosity of fluids. Phys Rev E 1999;59:4894–8. doi:10.1103/PhysRevE.59.4894.

[145] Schroder C. Comparing reduced partial charge models with polarizable simulations of ionic liquids. Phys Chem Chem Phys 2012;14:3089–102. doi:10.1039/C2CP23329K.

[146] Chaban V. Polarizability versus mobility: atomistic force field for ionic liquids. Phys Chem Chem Phys 2011;13:16055–62. doi:10.1039/C1CP21379B.

[147] Krummen M, Wasserscheid P, Gmehling J. Measurement of Activity Coefficients at Infinite Dilution in Ionic Liquids Using the Dilutor Technique. J Chem Eng Data 2002;47:1411–7. doi:10.1021/je0200517.

[148] Tokuda H, Hayamizu K, Ishii K, Susan MABH, Watanabe M. Physicochemical Properties and Structures of Room Temperature Ionic Liquids. 2. Variation of Alkyl Chain Length in Imidazolium Cation. J Phys Chem B 2005;109:6103–10. doi:10.1021/jp044626d.

[149] Gräfen H, Horn E-M, Schlecker H, Schindler H. Corrosion. Ullmann's Encycl. Ind. Chem., Wiley-VCH Verlag GmbH & Co. KGaA; 2000. doi:10.1002/14356007.b01_08.

[150] Cygan RT, Liang J-J, Kalinichev AG. Molecular Models of Hydroxide, Oxyhydroxide, and Clay Phases and the Development of a General Force Field. J Phys Chem B 2004;108:1255–66. doi:10.1021/jp0363287.

[151] Phan A, Ho TA, Cole DR, Striolo A. Molecular Structure and Dynamics in Thin Water Films at Metal Oxide Surfaces: Magnesium, Aluminum, and Silicon Oxide Surfaces. J Phys Chem C 2012;116:15962–73. doi:10.1021/jp300679v.

[152] Shaikhutdinov SK, Joseph Y, Kuhrs C, Ranke W, Weiss W. Structure and reactivity of iron oxide surfaces. Faraday Discuss 1999;114:363–80. doi:10.1039/A902633I.

[153] von Lautz J, Pastewka L, Gumbsch P, Moseler M. Molecular Dynamic Simulation of Collision-Induced Third-Body Formation in Hydrogen-Free Diamond-Like Carbon Asperities. Tribol Lett 2016;63:1–9. doi:10.1007/s11249-016-0712-9.

[154] Tersoff J. New empirical approach for the structure and energy of covalent systems. Phys Rev B 1988;37:6991–7000. doi:10.1103/PhysRevB.37.6991.

[155] Lindsay L, Broido DA. Optimized Tersoff and Brenner empirical potential parameters

for lattice dynamics and phonon thermal transport in carbon nanotubes and graphene. Phys Rev B 2010;81:205441. doi:10.1103/PhysRevB.81.205441.

[156] Cornell WD, Cieplak P, Bayly CI, Gould IR, Merz KM, Ferguson DM, et al. A Second Generation Force Field for the Simulation of Proteins, Nucleic Acids, and Organic Molecules. J Am Chem Soc 1995;117:5179–97. doi:10.1021/ja00124a002.

[157] Tokuda H, Tsuzuki S, Susan MABH, Hayamizu K, Watanabe M. How Ionic Are Room-Temperature Ionic Liquids? An Indicator of the Physicochemical Properties. J Phys Chem B 2006;110:19593–600. doi:10.1021/jp064159v.

[158] Angell CA. Formation of Glasses from Liquids and Biopolymers. Science (80-) 1995;267:1924–35. doi:10.1126/science.267.5206.1924.

[159] Ahosseini A, Scurto AM. Viscosity of Imidazolium-Based Ionic Liquids at Elevated Pressures: Cation and Anion Effects. Int J Thermophys 2008;29:1222–43. doi:10.1007/s10765-008-0497-7.

[160] Bair S, Mary C, Bouscharain N, Vergne P. An improved Yasutomi correlation for viscosity at high pressure. Proc Inst Mech Eng Part J J Eng Tribol 2013;228:424–34. doi:10.1177/1350650112474394.

[161] Cadena C, Zhao Q, Snurr RQ, Maginn EJ. Molecular Modeling and Experimental Studies of the Thermodynamic and Transport Properties of Pyridinium-Based Ionic Liquids. J Phys Chem B 2006;110 (6):2821–32. doi:10.1021/jp056235k.

[162] Liu H, Maginn E, Visser AE, Bridges NJ, Fox EB. Thermal and Transport Properties of Six Ionic Liquids: An Experimental and Molecular Dynamics Study. Ind Eng Chem Res 2012;51:7242–54. doi:10.1021/ie300222a.

[163] McCabe C, Cui S, Cummings PT, Gordon PA, Saeger RB. Examining the rheology of 9-octylheptadecane to giga-pascal pressures. J Chem Phys 2001;114:1887–91. doi:http://dx.doi.org/10.1063/1.1334676.

[164] Hamrock BJ, Dowson D. Isothermal Elastohydrodynamic Lubrication of Point Contacts: Part III - Fully Flooded Results. J Lubr Technol 1977;99:264–75. doi:10.1115/1.3453074.

[165] Blok H. Inverse problems: in hydrodynamic lubrication and design directives for lubricated flexible surfaces. Proc. Int. Symp. Lubr. Wear, McCutchan Publishing Corp.; 1963.

[166] Chaomleffel J-P, Dalmaz G, Vergne P. Experimental results and analytical film thickness predictions in EHD rolling point contacts. Tribol Int 2007;40:1543–52. doi:http://dx.doi.org/10.1016/j.triboint.2007.02.005.

[167] Bair S. High-pressure rheology for quantitative elastohydrodynamics. Elsevier; 2007.

[168] Vergne P. Habilitation thesis: Comportement Rhéologique des Lubrifiants et Lubrification : Approches Expérimentales. phdthesis. INSA de Lyon, 2002.

[169] Bair S, McCabe C, Cummings PT. Comparison of Nonequilibrium Molecular Dynamics with Experimental Measurements in the Nonlinear Shear-Thinning Regime. Phys Rev Lett 2002;88:58302. doi:10.1103/PhysRevLett.88.058302.

[170] Sweeney J, Webber GB, Rutland MW, Atkin R. Effect of ion structure on nanoscale friction in protic ionic liquids. Phys Chem Chem Phys 2014:16651–8. doi:10.1039/c4cp02320j.

[171] Rajput NN, Monk J, Hung FR. Structure and Dynamics of an Ionic Liquid Confined Inside a Charged Slit Graphitic Nanopore. J Phys Chem C 2012;116:14504–13.

doi:10.1021/jp3041617.

[172] Smith AM, Lovelock KRJ, Gosvami NN, Welton T, Perkin S. Quantized friction across ionic liquid thin films. Phys Chem Chem Phys 2013;15:15317–20. doi:10.1039/C3CP52779D.

[173] Hoang H, Galliero G. Local viscosity of a fluid confined in a narrow pore. Phys Rev E 2012;86:21202.

[174] Falk K, Sedlmeier F, Joly L, Netz RR, Bocquet L. Molecular origin of fast water transport in carbon nanotube membranes: superlubricity versus curvature dependent friction. Nano Lett 2010;10:4067–73. doi:10.1021/nl1021046.

[175] Falk K, Sedlmeier F, Joly L, Netz RR, Bocquet L. Ultralow liquid/solid friction in carbon nanotubes: comprehensive theory for alcohols, alkanes, OMCTS, and water. Langmuir 2012;28:14261–72. doi:10.1021/la3029403.

[176] Castejón HJ, Wynn TJ, Marcin ZM. Wetting and Tribological Properties of Ionic Liquids. J Phys Chem B 2014;118:3661–8. doi:10.1021/jp411765f.

[177] Huang DM, Sendner C, Horinek D, Netz RR, Bocquet L. Water slippage versus contact angle: A quasiuniversal relationship. Phys Rev Lett 2008;101:226101.

[178] Ho TA, Papavassiliou D V, Lee LL, Striolo A. Liquid water can slip on a hydrophilic surface. Proc Natl Acad Sci U S A 2011;108:16170–5. doi:10.1073/pnas.1105189108.

[179] Tocci G, Joly L, Michaelides A. Friction of Water on Graphene and Hexagonal Boron Nitride from Ab Initio Methods: Very Different Slippage Despite Very Similar Interface Structures. Nano Lett 2014;14:6872–7. doi:10.1021/nl502837d.

[180] Thompson PPA, Troian SSM. A general boundary condition for liquid flow at solid surfaces. Nature 1997;389:360–2.

[181] Martini A, Roxin A, Snurr RQ, Wang Q, Lichter S. Molecular Mechanisms of Liquid Slip. J Fluid Mech 2008;600:257–69. doi:10.1017/S0022112008000475.

[182] Kannam SK, Todd BD, Hansen JS, Daivis PJ. How fast does water flow in carbon nanotubes? J Chem Phys 2013;138:94701. doi:http://dx.doi.org/10.1063/1.4793396.

[183] Feng X, Xia Y. Tribological properties of Ti-doped DLC coatings under ionic liquids lubricated conditions. Appl Surf Sci 2012;258:2433–8. doi:http://dx.doi.org/10.1016/j.apsusc.2011.10.066.

[184] González R, Hernández Battez A, Blanco D, Viesca JL, Fernández-González A. Lubrication of TiN, CrN and DLC PVD Coatings with 1-Butyl-1-Methylpyrrolidinium tris(pentafluoroethyl)trifluorophosphate. Tribol Lett 2010;40:269–77. doi:10.1007/s11249-010-9674-5.

[185] Wang L, Liu X. Tribological behavior of DLC/IL solid-liquid lubricating coatings in a high-vacuum condition with alternating high and low temperatures. Wear 2013;304:13–9. doi:http://dx.doi.org/10.1016/j.wear.2013.04.004.

[186] Liu X, Wang L, Xue Q. DLC-based solid-liquid synergetic lubricating coatings for improving tribological behavior of boundary lubricated surfaces under high vacuum condition. Wear 2011;271:889–98. doi:http://dx.doi.org/10.1016/j.wear.2011.03.021.

[187] Liu X, Pu J, Wang L, Xue Q. Novel DLC/ionic liquid/graphene nanocomposite coatings towards high-vacuum related space applications. J Mater Chem A 2013;1:3797–809. doi:10.1039/C3TA00764B.

[188] Kondo Y, Koyama T, Tsuboi R, Nakano M, Miyake K, Sasaki S. Tribological Performance of Halogen-Free Ionic Liquids as Lubricants of Hard Coatings and Ceramics. Tribol Lett 2013;51:243–9. doi:10.1007/s11249-013-0159-1.

[189] Okada Y, Ito T, MINAMIKAWA T, KAMISUKI H, HIGAI S, SHIRATSUYU K. Molecular Dynamics Study of Ionic Liquids in Graphite Nanopores. Electrochemistry 2013;81:808–10. doi:10.5796/electrochemistry.81.808.

[190] Wang S, Li S, Cao Z, Yan T. Molecular Dynamic Simulations of Ionic Liquids at Graphite Surface. J Phys Chem C 2010;114:990–5. doi:10.1021/jp902225n.

[191] Liu X, Wang Y, Li S, Yan T. Effects of anion on the electric double layer of imidazolium-based ionic liquids on graphite electrode by molecular dynamics simulation. Electrochim Acta 2015;184:164–70. doi:http://dx.doi.org/10.1016/j.electacta.2015.10.064.

[192] Mendonca ACF, Fomin YD, Malfreyt P, Padua AAH. Novel ionic lubricants for amorphous carbon surfaces: molecular modeling of the structure and friction. Soft Matter 2013;9:10606–16. doi:10.1039/C3SM51689J.

[193] Ramos-Alvarado B, Kumar S, Peterson GP. Solid-Liquid Thermal Transport and Its Relationship with Wettability and the Interfacial Liquid Structure. J Phys Chem Lett 2016;7:3497–501. doi:10.1021/acs.jpclett.6b01605.

[194] Savio D, Fillot N, Vergne P, Hetzler H, Seeman W, Morales Espejel GE. A Multiscale Study on the Wall Slip Effect in a Ceramic–Steel Contact With Nanometer-Thick Lubricant Film by a Nano-to-Elastohydrodynamic Lubrication Approach. J Tribol 2015;137(3):31502. doi:10.1115/1.4029937.

[195] Balandin AA, Shamsa M, Liu WL, Casiraghi C, Ferrari AC. Thermal conductivity of ultrathin tetrahedral amorphous carbon films. Appl Phys Lett 2008;93. doi:http://dx.doi.org/10.1063/1.2957041.

[196] Shamsa M, Liu WL, Balandin AA, Casiraghi C, Milne WI, Ferrari AC. Thermal conductivity of diamond-like carbon films. Appl Phys Lett 2006;89. doi:http://dx.doi.org/10.1063/1.2362601.

[197] Mendonca ACF. Molecular Simulations of New Ammonium-based Ionic Liquids as Environmentally Acceptable Lubricant Oils. phdthesis. UNIVERSITE BLAISE PASCAL, 2013.

[198] Morrow TI, Maginn EJ. Molecular Dynamics Study of the Ionic Liquid 1-n-Butyl-3-methylimidazolium Hexafluorophosphate. J Phys Chem B 2002;106:12807–13. doi:10.1021/jp0267003.

[199] Borodin O. Polarizable Force Field Development and Molecular Dynamics Simulations of Ionic Liquids. J Phys Chem B 2009;113:11463–78. doi:10.1021/jp905220k.

[200] Swope WC, Andersen HC, Berens PH, Wilson KR. A computer simulation method for the calculation of equilibrium constants for the formation of physical clusters of molecules: Application to small water clusters. J Chem Phys 1982;76:637–49. doi:http://dx.doi.org/10.1063/1.442716.

[201] Kollman PA. Advances and continuing challenges in achieving realistic and predictive simulations of the properties of organic and biological molecules. Acc Chem Res 1996;29:461–9. doi:10.1021/ar9500675.

Publication and conferences

Publications:

N. Voeltzel, A. Giuliani, N. Fillot, P. Vergne and L. Joly - Nanolubrication by ionic liquids: molecular dynamics simulations reveal an anomalous effective rheology - **Phys. Chem. Chem. Phys.**, 2015,**17**, 23226-23235

N. Voeltzel, P. Vergne, N. Fillot, N. Bouscharain and L. Joly - Rheology of an Ionic Liquid with Variable Carreau Exponent - A Full Picture by Molecular Simulation with Experimental Contribution – **Tribology Letters**, 2016, **64**, 25

Conferences:

Journée internationales Francophones de la Tribologie - May 26-28 2014 - Mulhouse, France - Simulation d'un fluide ionique nano-confiné pour la lubrification

Tribology Frontiers Conference - Oct. 26-28 2014 - Chicago, USA - Nano-confined ionic liquid simulations for lubrication

Lubricated Contact Cádiz - April 13-17 2015 - Cádiz, Spain - Rheology of nanoconfined ionic liquids between oxide surfaces

International Tribology Conference - Sept. 16-20 2015 - Tokyo, Japan - Ionic liquid nanoconfined between metal oxide and DLC surfaces

Multiscale Materials Modeling International Conference - 9-14 Oct. 2016 - Dijon, France - Ionic liquids as lubricants: a multi-parameter and multi-scale puzzle

FOLIO ADMINISTRATIF

THESE DE L’UNIVERSITE DE LYON OPEREE AU SEIN DE L’INSA LYON

NOM : Voeltzel DATE de SOUTENANCE : 18/11/2016

Prénoms : Nicolas, Gaëtan

TITRE : Molecular simulations of an ionic liquid as lubricant: from bulk rheology to nanoconfinements

NATURE : Doctorat Numéro d'ordre : 2016LYSEI119

Ecole doctorale : MEGA

Spécialité : Mécanique

RESUME :

Les contraintes économiques et environnementales toujours plus exigeantes tendent à réduire la quantité de lubrifiant utilisée dans les systèmes mécaniques. Il en résulte des épaisseurs de film de l’ordre du nanomètre dans les zones de contact, laissant seulement quelques couches de molécules de lubrifiant pour assurer la séparation des surfaces. Pour relever ce défi, de nouveaux fluides sont à l’étude tels que les liquides ioniques qui présentent un formidable potentiel en tant que lubrifiants.
Grâce à la Dynamique Moléculaire, la réponse rhéologique d’un liquide ionique à différentes sollicitations de température, pression et cisaillement est tout d’abord caractérisée en détail. Avec l’appui d’essais expérimentaux, l’aptitude du liquide ionique à lubrifier des films minces est confirmée. Cette étude a également permis de jeter un nouveau regard sur les modèles analytiques classiques utilisés en rhéologie.
Le liquide ionique en situation de nano-confinement entre deux surfaces représentatives d’un contact acier-acier est ensuite étudié. Les effets combinés du glissement à la paroi, de la rhéofluidification et de l’élévation de température apportent des éléments de réponse pour expliquer la saturation de la contrainte de cisaillement aux fortes sollicitations.
Enfin, l’influence de différents revêtements de surface limitant grandement le frottement est analysée. Selon le matériau utilisé, des régimes de lubrification très différents surviennent avec un glissement du fluide à la paroi parfois prédominant. L’utilisation de surfaces polaires impacte également fortement la réponse des contacts lubrifiés par un liquide ionique.

MOTS-CLÉS :
Lubrication, Molecular Dynamics, Ionic Liquids, Very Thin Film, Rheology, Interfacial Dynamics

Laboratoire (s) de recherche : Laboratoire de Mécanique des Contacts et des Structures

Directeur de thèse: Dr. Nicolas Fillot, Dr. Laurent Joly

Présidente de jury : Prof. Anne Neville

Composition du jury :

Prof. Anne Neville (Examinatrice)
Prof. Agilio Padua (Rapporteur)
Dr. Rosa M. Espinosa-Marzal (Rapportrice)
Dr. Nicolas Fillot (Directeur)
Dr. Laurent Joly (Directeur)
Dr. Philippe Vergne (Examinateur)

Molecular simulation of an ionic liquid as lubricant: from bulk rheology to nanoconfinement

Les contraintes économiques et environnementales toujours plus exigeantes tendent à réduire la quantité de lubrifiant utilisée dans les systèmes mécaniques. Il en résulte des épaisseurs de film de l'ordre du nanomètre dans les zones de contact, laissant seulement quelques couches de molécules de lubrifiant pour assurer la séparation des surfaces. Pour relever ce défi, de nouveaux fluides sont à l'étude tels que les liquides ioniques qui présentent un formidable potentiel en tant que lubrifiants.

Grâce à la Dynamique Moléculaire, la réponse rhéologique d'un liquide ionique à différentes sollicitations de température, pression et cisaillement est tout d'abord caractérisée en détail. Avec l'appui d'essais expérimentaux, l'aptitude du liquide ionique à lubrifier des films minces est confirmée. Cette étude a également permis de jeter un nouveau regard sur les modèles analytiques classiques utilisés en rhéologie.

Le liquide ionique en situation de nano-confinement entre deux surfaces représentatives d'un contact acier-acier est ensuite étudié. Les effets combinés du glissement à la paroi, de la rhéofluidification et de l'élévation de température apportent des éléments de réponse pour expliquer la saturation de la contrainte de cisaillement aux fortes sollicitations.

Enfin, l'influence de différents revêtements de surface limitant grandement le frottement est analysée. Selon le matériau utilisé, des régimes de lubrification très différents surviennent avec un glissement du fluide à la paroi parfois prédominant. L'utilisation de surfaces polaires impacte également fortement la réponse des contacts lubrifiés par un liquide ionique.

Molecular simulation of an ionic liquid as lubricant: from bulk rheology to nanoconfinement

Increasing economic and environmental constraints tend to reduce the amount of lubricant used in mechanical systems. This results in nanometric film thicknesses in the contact areas, leaving only a few layers of lubricant molecules to ensure the separation of the surfaces. To meet this challenge, new fluids are being considered such as ionic liquids which feature a great potential as lubricants.

Through Molecular Dynamics simulations, the rheological response of an ionic liquid to different conditions of temperature, shear and pressure is first characterized in detail. The ability of the ionic liquid to lubricate thin films is confirmed. Besides, this study goes back over the classic analytical models used in rheology.

The ionic liquid is then nanoconfined between two representative surfaces of a steel-steel contact. The combined effects of wall slip, shear-thinning and temperature rise provide answers to explain the saturation of the shear stress.

Finally, the influence of different low friction surface coatings is analyzed. According to the material used, very different dynamical behaviors occur. Moreover, it is shown that the use of polar surfaces significantly impacts the response of ionic liquid lubricated contacts.